# Determining NMR relaxation times for porous media: Theory, measurement and the inverse problem

by

Yijia Li

A thesis
presented to the University of Waterloo
in fulfillment of the
thesis requirement for the degree of
Master of Mathematics
in
Applied Mathematics

Waterloo, Ontario, Canada, 2007

## Declarations

I hereby declare that I am the sole author of this thesis. This is a true copy of the thesis, including any required final revisions, as accepted by my examiners.

I understand that my thesis may be made electronically available to the public.

**Abstract**

This thesis provides an introduction to and analysis of the problem of determining nuclear magnetic resonance (NMR) relaxation times of porous media by using the so-called Carr-Purcell-Meiboom-Gill (CPMG) technique. We introduce the principles of NMR, the CPMG technique and the signals produced, porous effects on the NMR relaxation times and discuss various numerical methods for the inverse problem of extracting the relaxation times from CPMG signals. The numerical methods for solving Fredholm integral equations of the first kind are sketched from a series expansion perspective. A method of using arbitrary constituent functions for improving the performance of non-negative least squares (NNLS) is developed and applied to several synthesized data sets and real experimental data sets of saturated porous glass gels. The data sets were obtained by the author of this thesis and the experimental procedure will be presented. We discuss the imperfections in the assumptions on the physical and numerical models, the numerical schemes, and the experimental results, which may lead to new research possibilities.

**Acknowledgements**

Here I would like to thank the people whose support and encouragement made this thesis possible:

First I would like to thank Professor Edward R. Vrscay for directing me to this topic and for the invaluable discussions and demonstrations which helped me to understand the problem and accomplish some research on this subject.

I am very grateful for Dr. Hartwig Peemoeller, Department of Physics, University of Waterloo, for giving me the opportunity to work in his NMR lab and for his advice on studying relaxometry of porous media.

I sincerely thank Dr. Rick Holly, Jianzhen Liang, Dr. Claude Lemaire, Dr. Firas Mansour and Dr. Wlad Weglarz of the NMR lab for their assistance. I also thank Greg Mayer and Mehran Ebrahimi for providing me with many resources and for many helpful discussions.

# Contents

# List of Tables

# List of Examples

# Chapter 1

# Introduction

## 1.1 Outline of thesis

This thesis is concerned with the inverse problem of structure determination using nuclear magnetic resonance (NMR). Specifically, we consider the so-called Carr-Purcell-Meiboom-Gill (CPMG) method as applied to the problem of determining the pore structure of porous media. The CPMG method measures the transverse relaxation time $T_2$ (defined in the next chapter) of the target of interest.

CPMG is one of the most often employed methods in NMR since it uses a simple configuration that evens out local fluctuations of magnetic fields. Having been invented in 1950s, there has been a long history of study of its applications in different areas of science and the analysis of its results, including the effects of molecular diffusion in the measurements. However, it has also been known for a long time that the associated inverse problem for determination of $T_2$ from its data, which is the so-called problem of "separation of exponentials", is ill-posed and involves nonlinear fitting. Different methods for solving this problem have been developed and tested over the years. However, each of these methods has its own problems which include one or more of the following: resolving fitted parameters, treating noisy data and

large computing time requirements. Also, the limitations of solving this problem implied by its ill-posedness and numerical instability are seldom discussed in the literature.

In this thesis, we shall discuss the validity of the separation of exponentials model for CPMG experimental data, summarize the existing computational methods for analyzing CPMG data, illustrate the ill-posedness and the source of numerical instability of the inverse problem, and improve one of the computational methods. In particular, we focus on a nonlinear iteration scheme and a linear least-squares method modified by our analysis to solve the problem. Examples of these methods applied to real experimental data will be given.

Section 1.2 provides a brief introduction to the study of porous media and applications of nuclear magnetic resonance used in this study.

Chapter 2 provides a detailed introduction of the physical problem. Section 2.1 presents the quantum mechanical derivation of the governing equations of nuclear magnetization in a magnetic field. Section 2.2 introduces the relaxation behaviors of the nuclear magnetization for a macroscopic body. In Section 2.3, by solving the governing equations of magnetic resonance, we show that the data provided by the CPMG method are in the form of an exponential decay. Section 2.4 summarizes the models discussing porous effects on the relaxation times, which are the parameters to be measured. In Section 2.5 we formulate the data analysis model based on Section 2.3 and 2.4. In Section 2.6 we discuss the possible systematic errors that could invalidate the sum-of-exponentials model. In Section 2.7 we describe the experimental procedure employed by the author that produced the experimental data used in this thesis. Most sections in this chapter are useful when discussing sources of systematic errors that do not belong to the machine, and when discussing the applications of the CPMG and similar techniques. Readers who are particularly interested in the inverse problem may consult Section 2.5 only.

Chapter 3 and 4 deals with numerical aspects of this study. All discussions will assume the validity of the separation of exponentials model. Section 3.1 lists

five categories of methods that solve the problem, and summarizes the advantages and disadvantages of each of these methods. Section 3.2 discusses the numerical instability of the inverse problem. Section 3.3 shows how solving the problem in one domain can be extended to another domain.

Chapter 4 introduces the use of continuous constituent functions for the inverse problem. This is based on an expansion of the solution, and can be used to reduce the number of unknowns (Section 4.1) and improve on one of the numerical schemes (Section 4.2). This approach is suitable for any Fredholm integral equation of the first kind. And in Section 4.3, we present some conclusions that are practical for experimental data analysis.

In Chapter 5, the numerical methods are applied to real experimental data sets obtained by the author.

Chapter 6 summarizes all the assumptions and conclusions in the previous chapters for a clear view of the problem, and gives suggestions on future research possibilities on this topic.

## 1.2 Porous media

Many constituents in the earth's lithosphere, i.e., the sphere of soils and rocks, contain pores, although the pores may be difficult to observe directly. Man-made materials also usually contain pores. Some pores are formed unintentionally, for example those in concretes and rubbers. And some are made intentionally, for example those in filtering materials and insulation materials, which can be designed to have pores with certain pore sizes. Almost all biological tissues (e.g. lungs, cell walls, blood vessels) and some food products (e.g. bread, cake) are also porous.

To qualify as a "porous medium", a material, in addition to containing pores or "voids", has to be permeable to fluids (e.g. liquid, gas, etc.) [11]. As such, studies of solid structures that do not involve fluids do not belong to this field. The study

of porous media first arose in soil science. The main topics of concern are how fluids permeate these materials and how the fluids affect the properties of the material. Fluids in a porous medium can affect all kinds of physical properties of the material, such as the durability, permeability, thermal properties and electrical conductivity. As a practical application in oil and gas mining, the desired products move through the earth, including rock and sand. The study of how the products are transported and how they affect the mine base may help in improving the mining technologies.

In studies of porous media, one normally needs to set up models in terms of basic parameters that characterize the porous media. According to [11], a classical text in the field, the macroscopic parameters include porosity, specific surface area, permeability, etc., and the microscopic parameters include pore topology, definition of pore sizes for irregularly shaped voids, pore size distribution, etc.. The flow in a porous medium is treated by a capillary model. Also, flows can be viewed in a macroscopic sense.

Nuclear magnetic resonance is a non-invasive method (i.e., the material is not physically dissected) used to detect the pore structures and hydration level (usually defined as the ratio of pore water volume to pore volume) of a material. As will be introduced in Section 2.3, the parameters measured by NMR are different in different geometric confinements. The effects of this geometric confinement will be discussed in detail in Section 2.4. If the material is fully saturated in normal conditions, the NMR signal solely depends on the pore structures, the type of material, and the type of fluid. The Carr-Purcell-Meiboom-Gill (CPMG) technique has been applied to the measurements of materials with complex microstructures [10]. If the material is not fully saturated, the signal is weakened and the measured parameters will be relevant to the hydration level, as the fluids tend to be attached to the surface and behave differently from those in the center of a pore (Figure 1.1). Sequential measurements can observe the hydration ([29] for cements and [43] for glass gels) or dehydration processes, or the evolution of solid structures due to hydration [4].

The target of study can also be the actual substances in the pores. For example,

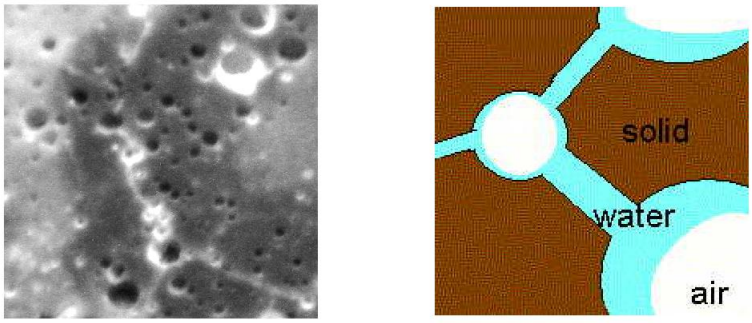


Figure 1.1: An image of a real concrete with pores (left), and a hypothetical picture of a partially saturated porous media (right).

we can study diffusion, random fast-exchange phenomena, and surface interactions of water molecules in pores [39].

As mentioned in the Section 1.1, the CPMG technique is very frequently used in NMR experiments. And it is also of paramount importance in the study of porous media using NMR. There are many papers regarding the data analysis procedure of CPMG data for porous samples, such as Glasel [13], Kroeker *et al.* [22], Stewart [40] and Williams *et al.* [47]. The data analysis procedure is what we will focus on starting in Chapter 3. Very basic NMR experiments such as CPMG yields single temporal signals for the entire sample. In contrast, 1D, 2D or 3D NMR imaging, or magnetic resonance imaging (MRI), can produce signals corresponding to particular regions in a medium. As such, the medium, in particular its pore structures can be imaged. These images can be compared with those obtained by other means, like CT and ultraviolet imaging. With NMR techniques for flow imaging, the flow of liquids in porous medium can be visualized [5].

# Chapter 2

# Some Basics of Nuclear Magnetic Resonance and the CPMG Method

## 2.1 Molecular spin under a magnetic field

Nuclear magnetic resonance (NMR) is a technique that detects the inner properties of an object while the object is intact. The principles of NMR were proposed in the 1940s by Bloch [7] following the discovery of nuclear spin. In 1950s the spin echo scheme was devised by Hahn, Carr and Purcell [17]. The basics of NMR imaging was developed in the 1970s by Lauterbur [26] and Mansfield [30], who received Nobel Prizes for their respective work in this area.

The basic exerimental setup for NMR is illustrated schematically in Figure 2.1. A large coil is responsible for the production of a strong stationary field, most often homogeneous and directed vertically ($z$-axis). This field produces the longitudinal alignment of molecular spins. An rf (radio frequency) coil generates a magnetic field that rotates about the $z$-axis. This field produces transverse (i.e., towards the $x$-$y$ plane) excitation of the molecular spins. 1D, 2D and 3D measurements (imaging) are accomplished by imposing 1D, 2D or 3D gradient fields and selective pulses other

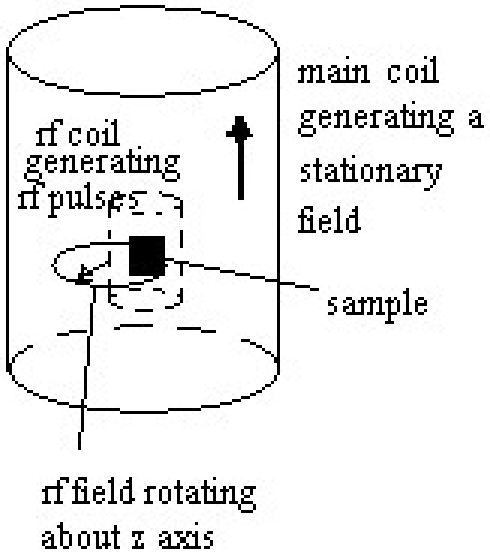


Figure 2.1: The basic step of an NMR experiment.

than the basic setup. NMR imaging is of great importance in modern medicine. Also the experiments can be configured to measure proton density, the degree of diffusion in magnetic field gradients, or flow of particles. Hinshaw *et al.* [18] provides an excellent introduction for beginners on these different measurements. In medicine and engineering, hydrogen, specifically, its nucleus, the proton, is usually the target of measurement. The hydrogen nucleus is the easiest to measure because of its small excitation energy and small strength of chemical bonds. It is easy to rotate in the magnetic field and so require less power in the experiments. In chemistry and biology, larger particles like nitrogen or phosphorus are measured.

The physical basis of NMR is the interaction of a nuclear spin with magnetic fields. The discussion below is brief. For more details, the reader may consult [15].

Many quantum mechanical particles (e.g. electrons, protons, neutrons, nuclei) possess an intrinsic angular momentum or spin. Let $\vec{S}$ denote the spin angular

momentum of such a particle. A particle having non-zero spin $\vec{S}$ also has a magnetic moment $\vec{\mu}$ proportional to its spin, i.e., $\vec{\mu} = \gamma\vec{S}$, where $\gamma$ is the so-called gyromagnetic ratio. (For protons, it is $\gamma = \frac{2.79e}{M_p c}$ where $e$ is the electrostatic unit, $M_p$ is the mass of proton, and $c$ is the speed of light.)

The interaction of a magnetic moment $\vec{\mu}$ with an applied magnetic field $\vec{B}$ is defined by the quantum mechanical Hamiltonian operator

$$\hat{H} = -\vec{\mu} \cdot \vec{B} = -\gamma \vec{B} \cdot \vec{S}. \tag{2.1}$$

The simplest case, a particle of spin-$\frac{1}{2}$, will actually be most relevant since it includes the case of a proton, the nucleus of a hydrogen atom. The quantum mechanical operator of a spin-$\frac{1}{2}$ particle can be written in terms of the so-called $2 \times 2$ Pauli matrix operators as follows

$$\vec{S} = \frac{1}{2}\hbar\vec{\sigma} \quad or \quad (S_x, S_y, S_z) = \frac{1}{2}\hbar(\sigma_x, \sigma_y, \sigma_z), \tag{2.2}$$

where $\hbar = \frac{h}{2\pi}$ and $h$ is Planck's constant ($6.63 \times 10^{-34} m^2 kg/s$). The Pauli matrices are given by

$$\sigma_x = \begin{pmatrix} 0 & 1 \\ 1 & 0 \end{pmatrix}, \quad \sigma_y = \begin{pmatrix} 0 & -i \\ i & 0 \end{pmatrix}, \quad \sigma_z = \begin{pmatrix} 1 & 0 \\ 0 & -1 \end{pmatrix}. \tag{2.3}$$

In order to solve for the spin angular momentum in only a static field pointing to the "z" direction, we consider $\sigma_z$. Note that $\sigma_z$ has eigenvalues $S_z = +1$ and $-1$ with corresponding "spin up" ($S_z = +1$) and "spin down" ($S_z = -1$) eigenstates, respectively,

$$\vec{u}_1 = \begin{pmatrix} 1 \\ 0 \end{pmatrix}, \quad \vec{u}_2 = \begin{pmatrix} 0 \\ 1 \end{pmatrix}. \tag{2.4}$$

Also note that these eigenstates may be represented by two-component vectors. Such vectors are also known as "spinors".

Now let us assume that the spin-$\frac{1}{2}$ particle is in the presence of a constant mag-

netic field $\vec{B}$, pointing in the $z$ direction with magnitude $B_0$, i.e., $\vec{B} = \vec{B}_0 = (0, 0, B_0)$. Then from (2.1) the interaction Hamiltonian is given by

$$\hat{H} = -\frac{1}{2}\gamma\hbar B_0\sigma_z. \tag{2.5}$$

The eigenstates of $\sigma_z$ are thus seen to be eigenstates of the Hamiltonian $\hat{H}$, i.e.,

$$\hat{H}\vec{u}_1 = -\frac{1}{2}\gamma\hbar B_0\vec{u}_1 = E_1\vec{u}_1, \tag{2.6}$$

$$\hat{H}\vec{u}_2 = \frac{1}{2}\gamma\hbar B_0\vec{u}_2 = E_2\vec{u}_2. \tag{2.7}$$

Note that $E_1 < E_2$, i.e., the "spin up" eigenstate $\vec{u}_1$, which is the state for which the spin $\vec{S}$ or magnetic moment $\vec{\mu}$ is parallel to $\vec{B}_0$, has lower energy than the "spin down" eigenstate $\vec{u}_2$. The negative sign for $E_1$ means that the nuclear magnetization is antiparrelell to the external field.

The difference in energies of the "spin up" and "spin down" eigenstates induced by the presence of the magnetic field $\vec{B}_0$ is known as the Zeeman effect in a field that is not too high. The frequency $\omega_0$ of electromagnetic radiation that corresponds to this difference in energy is determined by the relation

$$\hbar\omega_0 = E_2 - E_1 = \gamma\hbar B_0. \tag{2.8}$$

Therefore,

$$\omega_0 = \gamma B_0 \tag{2.9}$$

is the "resonant frequency" of excitation. We shall return to this result below.

According to quantum mechanics, the time evolution of a two-component state vector $\psi(t)$ or wavefunction of a spin-$\frac{1}{2}$ particle in the magnetic field $\vec{B}_0$ will be given by the time-dependent Schrödinger equation

$$i\hbar\frac{d\psi}{dt} = \hat{H}\psi = -\frac{1}{2}\gamma\hbar B_0\sigma_z\psi. \tag{2.10}$$

It is convenient to express $\psi(t)$ in terms of the basis set $\vec{u}_1$ and $\vec{u}_2$, i.e.,

$$\psi(t) = c_1(t)\vec{u}_1 + c_2(t)\vec{u}_2, \tag{2.11}$$

where $c_1(t)$ and $c_2(t)$ are complex-valued coefficients that must satisfy the normalization condition

$$|c_1(t)|^2 + |c_2(t)|^2 = 1. \tag{2.12}$$

The solution to Eq. (2.10) is

$$\psi(t) = c_{10}e^{-iE_1t/\hbar}\vec{u}_1 + c_{20}e^{-iE_2t/\hbar}\vec{u}_2, \tag{2.13}$$

where $c_{10} = c_1(0), c_{20} = c_2(0)$ such that $|c_{10}|^2 + |c_{20}|^2 = 1$.

In particular, we are interested in the expectation values of the components $\mu_i$ of the magnetic moment vector $\vec{\mu}$, which may be computed as follows,

$$\langle \mu_i \rangle = \gamma \langle S_i \rangle = \langle \psi(t) | \frac{1}{2} \gamma \hbar \sigma_i | \psi(t) \rangle, \;\; i = x, y, z, \tag{2.14}$$

where

$$\langle S_i \rangle = \langle \psi(t) | S_i | \psi(t) \rangle.$$

Here, we have employed the so-called Dirac "bra-ket" notation ("bra" yields complex-conjugate transpose).

For example, in the calculation of $\langle \mu_x \rangle$,

$$\sigma_x|\psi(t)\rangle = \begin{pmatrix} 0 & 1 \\ 1 & 0 \end{pmatrix} \left[ c_{10}e^{-iE_1t/\hbar} \begin{pmatrix} 1 \\ 0 \end{pmatrix} + c_{20}e^{-E_2t/\hbar} \begin{pmatrix} 0 \\ -1 \end{pmatrix} \right] \tag{2.15}$$

$$= c_{10}e^{-iE_1t/\hbar} \begin{pmatrix} 0 \\ 1 \end{pmatrix} + c_{20}e^{-iE_2t/\hbar} \begin{pmatrix} -1 \\ 0 \end{pmatrix}, \tag{2.16}$$

so that

$$\langle \mu_x \rangle = \frac{1}{2}\gamma\hbar \left[ c_{10}^* e^{iE_1 t/\hbar} \begin{pmatrix} 1 \\ 0 \end{pmatrix}^T + c_{20}^* e^{iE_2 t/\hbar} \begin{pmatrix} 0 \\ -1 \end{pmatrix}^T \right]$$
$$\cdot \left[ c_{10} e^{-iE_1 t/\hbar} \begin{pmatrix} 0 \\ 1 \end{pmatrix} + c_{20} e^{-iE_2 t/\hbar} \begin{pmatrix} -1 \\ 0 \end{pmatrix} \right] \tag{2.17}$$

$$= -\frac{1}{2}\gamma\hbar \left[ c_{10}^* c_{20} e^{i(E_1 - E_2)t/\hbar} + c_{10} c_{20}^* e^{-i(E_1 - E_2)t/\hbar} \right] \tag{2.18}$$

$$= -\gamma\hbar Re \left[ c_{10} c_{20}^* e^{i\omega_0 t} \right]. \tag{2.19}$$

Similarly, we find that

$$\langle \mu_y \rangle = -\frac{1}{2}\gamma\hbar \left[ i c_{10}^* c_{20} e^{i(E_1 - E_2)t/\hbar} - i c_{10} c_{20}^* e^{-i(E_1 - E_2)t/\hbar} \right] \tag{2.20}$$

$$= -\gamma\hbar Re \left[ -i c_{10} c_{20}^* e^{i\omega_0 t} \right], \tag{2.21}$$

and

$$\langle \mu_z \rangle = \frac{1}{2}\gamma\hbar \left[ |c_{10}|^2 - |c_{20}|^2 \right]. \tag{2.22}$$

In all cases, the expectation value $\langle \mu_z \rangle$ is constant, depending only on the initial values $c_1(0)$ and $c_2(0)$. Moreover, $\langle \mu_x \rangle$ and $\langle \mu_y \rangle$ are real-valued since they involve the multiplication of complex quantities to their conjugates.

Here are three special cases:

1. $c_1(0) = 1,\ \ c_2(0) = 0$. Then $\psi(0) = \vec{u}_1$ so that $\psi(t) = e^{-iE_1 t/\hbar}\vec{u}_1$. In this case $\langle \mu_x \rangle = \langle \mu_y \rangle = 0$ and $\langle \mu_z \rangle = \frac{1}{2}\gamma\hbar$.

2. $c_1(0) = 0,\ \ c_2(0) = 1$. Then $\psi(0) = \vec{u}_2$ so that $\psi(t) = e^{-iE_2 t/\hbar}\vec{u}_2$. Thus $\langle \mu_x \rangle = \langle \mu_y \rangle = 0$ and $\langle \mu_z \rangle = -\frac{1}{2}\gamma\hbar$.

3. $c_1(0) = c_2(0) = \frac{1}{\sqrt{2}}$. After some calculations,

$$\langle \mu_x \rangle = -\frac{1}{2}\gamma\hbar \cos \omega_0 t$$

$$\langle \mu_y \rangle = -\frac{1}{2}\gamma\hbar \sin \omega_0 t$$

$$\langle \mu_z \rangle = 0.$$

In general, we may view the expectation values $\langle \mu_x \rangle$, $\langle \mu_y \rangle$ and $\langle \mu_z \rangle$ as components of a vector $\vec{\mu}_{av} \in \mathbb{R}^3$. A straightforward calculation shows that

$$||\vec{\mu}_{av}|| = [\langle \mu_x \rangle^2 + \langle \mu_y \rangle^2 + \langle \mu_z \rangle^2]^{1/2} \tag{2.23}$$

$$= \frac{1}{2}\gamma\hbar. \tag{2.24}$$

Furthermore, this "average magnetic moment vector" $\vec{\mu}_{av}$ precesses about the $z$-axis, the axis of the static magnetic field $\vec{B}_0$. The angular frequency of the precession is $\omega_0$, the resonant frequency defined in Eq. (2.9). Note that $\omega_0$ is determined by the energy level spacing $\Delta E = E_2 - E_1$ which, in turn, is proportional to the magnitude $B_0$ of the applied magnetic field $\vec{B}_0$.

The reader will note the similarity of the above results, derived from quantum mechanics, to those obtained from classical electromagnetic theory. Here, the motion of a magnetic moment $\vec{\mu}$ in an external field $\vec{B}_0$ is described by the equation

$$\frac{d\vec{\mu}}{dt} = \gamma\vec{\mu} \times \vec{B}_0. \tag{2.25}$$

In the case that $\vec{B}_0 = (0, 0, B_0)$ and $\vec{\mu}(0) = (\mu_x(0), \mu_y(0), \mu_z(0))$, it is easily shown [24] that the solution to this equation is given by

$$\mu_x(t) = \mu_x(0) \cos \omega_0 t + \mu_y(0) \sin \omega_0 t,$$

$$\mu_y(t) = \mu_y(0) \cos \omega_0 t - \mu_x(0) \sin \omega_0 t,$$

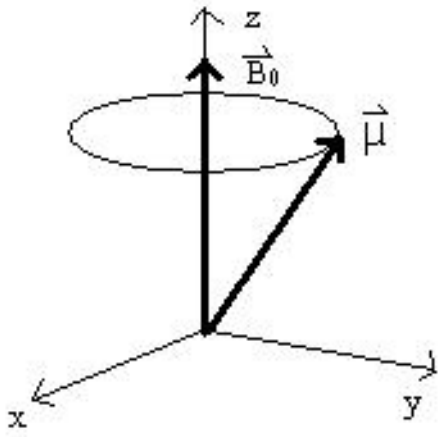


Figure 2.2: Precession of the nuclear magnetic moment $\vec{\mu}$ about the static field $\vec{B}_0$.

$$\mu_z(t) = \mu_z(0),$$

where $\omega_0 = \gamma B_0$. The classical magnetic moment vector $\vec{\mu}(t)$, therefore, precesses about $\vec{B}_0$ with angular frequency $\omega_0$. This precession of a magnetic moment about a static magnetic field is known as *Larmor precession*. The frequency $\omega_0$ is known as the *Larmor frequency*.

We shall now exploit the similarity of quantum and classical descriptions and use the latter to explain another fundamental feature of NMR, namely, the use of an applied radio frequency magnetic field $\vec{B}_1(t)$, directed perpendicularly to $\vec{B}_0$, to induce transitions from one Zeeman energy level to another. This phenomenon was originally studied by Purcell, Torrey and Pound [36] in paraffin containing hydrogen nuclei.

We now suppose that in addition to the static magnetic field $\vec{B}_0 = (0, 0, B_0)$ there now exists a radio frequency magnetic field $\vec{B}_1(t)$ with the frequency of rotation $\omega$. The motion of the magnetic moment $\vec{\mu}(t)$ in the laboratory coordinate system is then

given by the equation

$$\frac{d\vec{\mu}}{dt} = \vec{\mu} \times \gamma(\vec{B}_0 + \vec{B}_1(t)). \tag{2.26}$$

One procedure in the literature (e.g. see [24]) is to consider the following form for $\vec{B}_1$,

$$\vec{B}_1(t) = (B_1 \cos \omega t, 0, 0). \tag{2.27}$$

$\vec{B}_1(t)$ is said to be "linearly polarized" along the $x$-axis. Obviously, it is perpendicular to the static field $\vec{B}_0$. Substitution of $\vec{B}_1(t)$ into Eq. (2.26) leads to a first order linear time-dependent system of DEs in the components $\mu_i$ which is not exactly solvable. We shall follow the literature (see again [24]) and provide a very good approximation to the exact solution $\vec{\mu}(t)$ in terms of some geometrical arguments.

Firstly, the linearly polarized field $\vec{B}(t)$ may be considered as a sum of two vectors, $\vec{B}_+(t)$ and $\vec{B}_-(t)$, that rotate about the $z$-axis with frequency $\omega$ but in opposite directions, i.e.,

$$\vec{B}(t) = \vec{B}_+(t) + \vec{B}_-(t),$$

where

$$\vec{B}_\pm(t) = \frac{1}{2}(B_1 \cos \omega t, \pm B_1 \sin \omega t, 0).$$

We shall consider only the component $\vec{B}_-(t)$ which rotates in the same direction as the classical Larmor precessing magnetic moment $\vec{\mu}(t)$ in the laboratory system discussed earlier (clockwise in $x$-$y$ plane). The argument is that the counter-rotating component $\vec{B}_+(t)$ perturbs the motion of $\vec{\mu}(t)$ only very slightly and therefore may be neglected [18].

We now consider a coordinate system $(x', y', z')$ that rotates about the laboratory $z$-axis in the direction of the Larmor precession but with angular frequency $\omega$. Note that in the rotating system, the vector $\vec{B}_-(t)$ is stationary.

Let $\vec{\mu}'$ denote the magnetic moment vector expressed in terms of the rotating set of basis vectors $\{\hat{i}', \hat{j}', \hat{k}'\}$. The equation of motion of $\vec{\mu}'$ in this system will then be

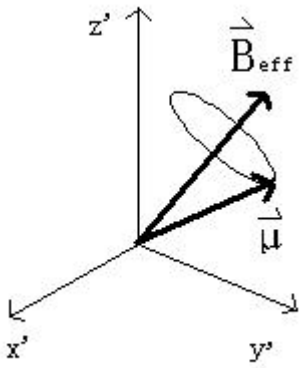


Figure 2.3: Precession of $\vec{\mu}$ about $\vec{B}_{eff}$ in rotating coordinate system.

given by

$$\frac{d\vec{\mu}'}{dt} = \vec{\mu}' \times \gamma(B_0\hat{k}' + \frac{1}{2}\hat{B}_1\hat{i}') - \vec{\mu}' \times \omega\hat{k}' \tag{2.28}$$

$$= \vec{\mu}' \times \gamma[(B_0 - \frac{\omega}{\gamma})\hat{k}' + B_{rf}\hat{i}'], \tag{2.29}$$

where $B_{rf} = \frac{1}{2}B_1$. The term $-\vec{\mu}' \times \omega\hat{k}'$ accounts for the rotating coordinate system.

From Eq. (2.29), we see that in the rotating reference frame, the vector $\vec{\mu}'$ precesses about an effective static magnetic field

$$\vec{B}_{eff} = B_{rf}\hat{i}' + (B_0 - \frac{\omega}{\gamma})\hat{k}'. \tag{2.30}$$

The angular frequency of precession of $\vec{\mu}'$ about $\vec{B}_{eff}$ in this rotating frame is given by

$$\omega' = \gamma||\vec{B}_{eff}|| = \gamma[(B_0 - \frac{\omega}{\gamma})^2 + B_{rf}^2]^{1/2}. \tag{2.31}$$

(Note: In many books, the radio frequency field $\vec{B}_1$ is simply assumed to be "circu-

larly polarized", i.e., rotating clockwise with frequency $\omega$, i.e.,

$$\vec{B}(t) = (B_1 \cos \omega t, -B_1 \sin \omega t, 0).$$

In this case, $B_{rf} = B_1$.)

The condition of "resonance" for this system is $\omega = \gamma B_0$, that is, $\omega = \omega_0$, the Larmor frequency, In this case, from Eq. (2.29), the effective magnetic field in the rorating frame is $\vec{B}_{eff} = B_{rf}\hat{i}'$. From Eq. (2.9), the frequency of precession of $\vec{\mu}$ about $\vec{B}_{eff}$ is $\omega_1 = \gamma B_{rf}$.

Let us now examine the effects of the rf field $\vec{B}(t)$ on the magnetic moment vector $\vec{\mu}$ at resonance. First, we assume that $\vec{\mu}$ is parallel to the static field $\vec{B}_0 = B_0\hat{k}$. (In the quantum case, this would correspond to the "spin up" state $\psi = \vec{u}_1$.) During the application of $\vec{B}(t)$, the magnetic moment vector $\vec{\mu}$ will precess about $\vec{B}_{eff} = B_{rf}\hat{i}'$ in the rotating frame, specifically, in the $y'$-$z'$ plane with angular frequency $\omega_1 = \gamma B_{rf}$. If the field $\vec{B}(t)$ is applied over a quarter of the period of the precession, i.e., over the time $t = \pi/(2\omega_1) = \pi/(2\gamma B_{rf})$, then the vector $\vec{\mu}$ will have rotated by an angle $\pi/2$ (a "90° rotation"), so that it will lie on the $y'$-axis. If the field $\vec{B}(t)$ is then turned off, the magnetic moment vector $\vec{\mu}$ will remain in the $y'$-axis, therefore precessing about $\vec{B}_0$ in the $xy$ laboratory frame. This is known as a "$\pi/2$ pulse" or "90 degree pulse".

On the other hand, if the field $\vec{B}(t)$ is applied over one-half of the period of precession, i.e., over the time $t = \pi/(\gamma B_{rf})$, then $\vec{\mu}$ will have presessed about $\vec{B}_{rf}$ from the direction of $\vec{B}_0$ to that of $-\vec{B}_0$. This "$\pi$-pulse" or "180 degree pulse" has essentially "flipped" the direction of the magnetic moment vector $\vec{\mu}$. In the quantum case, this would correspond to the "excitation" of the magnetic moment from the lower $E_1$, "spin-up", energy state to the higher $E_2$, "spin-down", energy state. Of course, if the magnetic moment vector $\vec{\mu}$ were originally pointing in the $-\vec{B}_0$ direction, it would be "flipped" to the $\vec{B}_0$ direction by a "$\pi/2$ pulse".

In summary, we have just shown how a radio frequency magnetic field $\vec{B}(t)$ applied

in the $xy$-plane can rotate the magnetic moment vector $\vec{\mu}$ about the x'-axis in the case of resonance. Similarly, the magnetic moment vector can be rotated about other directions in the xy-plane if $B_1$ is pointing to other directions in the xy-plane in the rotating frame.

NMR experiments are normally performed in macroscopic systems of spins/magnetic moments, for example, the spin-$\frac{1}{2}$ hydrogen nuclei in a container of water at room temperature or the hydrogen nuclei of water contained in a biological tissue specimen. Moreover, the atoms or molecules containing these nuclei are constantly colliding, hence interacting, due to thermal motion. As a result, it is not the case that all nuclei in the presence of a static magnetic field $\vec{B}_0$ will be in the lowest energy state. The behaviors of such macroscopic collections of quantum systems is the subject of statistical mechanics. We state here, only very briefly, that at "thermal equilibrium" the fraction of nuclei in a sample that are in a particular state with energy $E_m$ is given by

$$P_m = \frac{e^{-E_m/kT}}{Z}, \tag{2.32}$$

where $T$ is the temperature, $k$ is the Boltzman constant, and

$$Z = \sum_m e^{-E_m/kT}, \tag{2.33}$$

is the so-called "partition function".

For spin-$\frac{1}{2}$ particles, in the presence of a static $\vec{B}_0$ field, recall that $E_1 < E_2$ so that the equilibrium population of the spin-up (parallel alignment) nuclei will be greater than that of the spin-down (antiparallel alignment). In the "$\pi/2$-pulse or $\pi$-pulse" experiments described earlier, there are more transitions induced from the lower energy state to the higher energy state than the reverse.

## 2.2 Macroscopic magnetization, relaxation and the Bloch equations

The following section is based primarily upon the discussion in [15]. Consider, for simplicity, a macroscopic body that is composed of protons, i.e., hydrogen nuclei, the spin/magnetic moments of which will contribute to an NMR signal. The magnetization, $\vec{M}(\vec{r},t)$, is defined as the local magnetic moment per unit volume at a point $\vec{r}$ in the body and at time $t$, as follows. We consider a volume $V(\vec{t})$ centered at $\vec{r}$ that is sufficiently small so that external fields are, to a good approximation, homogeneous over $V(\vec{r})$ yet sufficiently large to contain a large number of protons. The magnetization is then

$$\vec{M}(\vec{r},t) = \frac{1}{V(\vec{r})}\sum_i \vec{\mu}_i, \tag{2.34}$$

where the sum is over all protons in $V(\vec{r})$. The interaction of each magnetic moment in $V(\vec{r})$ with an external magnetic field $\vec{B}_{ext}$ is given by

$$\frac{d\vec{\mu}_i}{dt} = \gamma\vec{\mu}_i \times \vec{B}_{ext}(\vec{r}). \tag{2.35}$$

If we sum over all protons in $V(\vec{r})$ and divide by $V(\vec{r})$, we arrive at the following equation for the magnetization at $\vec{r}$:

$$\frac{d\vec{M}}{dt} = \gamma\vec{M} \times \vec{B}_{ext}. \tag{2.36}$$

Here we emphasize that no other interactions involving the magnetic moments $\vec{\mu}_i$ are being considered at this time. In other words, we are ignoring any interactions between the protons.

The reader will note the similarity in structure between Eq. (2.36) for the magnetization $\vec{M}$ and Eq. (2.35) for the magnetic moment of a single spin particle. This

essentially implies that we may consider the net magnetization of a macroscopic assembly of spin magnetic moments as a single magnetic moment obtained from the vector sum of magnetic moments in the assembly, if no inter-molecular interactions are considered.

In the case of a main static field $\vec{B}_{ext} = \vec{B}_0 = B_0\hat{k}$ it is convenient to consider two components of the magnetization,

1) $\vec{M}_{||} = M_z\hat{k}$, the parallel or "longitudinal" component,

2) $\vec{M}_{\perp} = M_x\hat{i} + M_y\hat{j}$, the "transverse" components.

From Eq. (2.36), it follows that

$$\frac{dM_z}{dt} = 0, \tag{2.37}$$

and

$$\frac{d\vec{M}_{\perp}}{dt} = \gamma\vec{M}_{\perp} \times \vec{B}_0. \tag{2.38}$$

The $3\times3$ system in (2.36) has decomposed into parallel and transverse ($2\times2$) systems.

Given the similarity between Eq. (2.36) for $\vec{M}$ and Eq. (2.35) for the magnetic moment of a single spin, the solutions for $M_x(t)$, $M_y(t)$ and $M_z(t)$ will have the same form as $\mu_x(t)$, $\mu_y(t)$ and $\mu_z(t)$ in Eq. (2.35).

Eqs. (2.36) and (2.35), however, are inadequate for the modelling of real assemblages of protons in macroscopic materials, since the protons interact with each other in their neighbourhoods. A more realistic description of real systems will require additional terms in these equations which depend upon relaxation parameters that are different for the two equations. The components $M_z$ and $\vec{M}_{\perp}$ relax in different ways toward their final values.

## $M_z$ and $T_1$ relaxation

In a macroscopic system of interacting protons immersed in a static external magnetic field $\vec{B}_{ext} = B_0\hat{k}$, the magnetic moments of these protons try to align with the external field through the exchange of energy with the surroundings. This exchange is accomplished through thermal motion of the atoms that contain these protons and their subsequent collisions with other atoms in the system. An argument considering the potential energy of the nuclear magnetization ([15], p. 53) shows that there is an equilibrium value $M_0$ for the parallel magnetization $M_z$ of the system, with

$$M_0 = \frac{1}{4}\rho_0 \frac{\gamma^2\hbar^2}{kT} B_0, \tag{2.39}$$

where $\rho_0$ is the proton density, $k$ is Boltzman's constant and $T$ is the absolute temperature. The rate of change of $M_z$ is proportional to the difference $M_0 - M_z$. The proportionality constant, determined experimentally, is inversely related to the time scale of the growth/decay rate. As such, Eq. (2.37) is replaced by the equation

$$\frac{dM_z}{dt} = \frac{1}{T_1}(M_0 - M_z), \tag{2.40}$$

where $T_1$ is the "spin-lattice relaxaion time". The value of $T_1$ for pure water is 3.6 s at a termperature of 25 °C. Some typical values for various human tissues are given in Table 2.1 ([15], p. 54) below.

The solution of Eq. (2.40) is

$$M_z(t) = M_z(0)e^{-t/T_1} + M_0(1 - e^{-t/T_1}). \tag{2.41}$$

After an r.f. pulse $\vec{B}_1(t)$, discussed earlier, the parallel magnetization displays an exponential grow from the initial value $M_z(0)$ to the equilibrium value $M_0$.

## $\vec{M}_\perp$ and $T_2$ relaxation

In our macroscopic system of interacting protons, the transverse magnetization $\vec{M}_\perp(t)$ decays to zero, but due to a different process, in which spins experience not only the external applied field but also static local fields of their due to spins in their neighbourhood. The variations in the local fields cause different local precessional frequencies. As a result, individual spins that may have been aligned initially in the $xy$ plane will "fan out" in time, thus reducing the net transverse magnetization – the sum of all individual transverse components – in the $xy$ plane. Thus fanning out is also known as "dephasing".

This decay of the transverse magnetization leads to the introduction of another experimental parameter, the "spin-spin" relaxation time $T_2$. If we assume that the decay is exponentially, Eq. (2.38) is then modified by the addition of a decay term, i.e.,

$$\frac{d\vec{M}_\perp}{dt} = \gamma\vec{M}_\perp \times \vec{B}_0 - \frac{1}{T_2}\vec{M}_\perp. \tag{2.42}$$

The solution to this system will be given below.

The relaxation rates for spin-spin interactions, where no energy is lost, are higher than those for spin-lattice couplings. As a result $T_2 < T_1$. The value of $T_2$ for pure water is 3.6 s at a temperature of 25 °C. The $T_2$ values for some human tissues are given in Table 2.1 ([15] p. 54). The values of $T_2$ are very short for solids (generally in the order of microseconds) and much longer for liquids (on the order of seconds).

## $T_2^*$ and $T_2'$ relaxation rates

In practical situations, external field homogeneities can result in additional dephasing of the transverse magnetization. Sometimes, the resulting change in the relaxation times can be characterized by a separate decay time $T_2'$. The total relaxation rate,

| Tissue | $T_1$(ms) | $T_2$(ms) |
|---|---|---|
| gray matter (GM) | 950 | 100 |
| white matter (WM) | 600 | 80 |
| muscle | 900 | 50 |
| cerebrospinal fluid (CSF) | 4500 | 2200 |
| fat | 250 | 60 |
| blood | 1200 | 100-200 |

Table 2.1: Representative values of relaxation parameters $T_1$ and $T_2$ in milliseconds, for hydrogen components of different human body tissues at $B_0 = 1.5$ T and 37 °C (from [15])

.

defined as $R_2^*$, is the sum of internal and external relaxation rates, i.e.,

$$R_2^* = R_2 + R_2'. \tag{2.43}$$

Since relaxation rates are defined as the inverses of their respective relaxation times, we can define an overall relaxation time $T_2^* = 1/R_2^*$ as follows,

$$\frac{1}{T_2^*} = \frac{1}{T_2} + \frac{1}{T_2'}. \tag{2.44}$$

The loss of transverse magnetization due to $T_2'$ is recoverable by "spin echo" methods, including the CPMG method to be discussed below. On the other hand, the intrinsic $T_2$ decay is not recoverable, being due to static randome variations of local fields in a solid and local, random, time-dependent field fluctuations in a liquid.

Eqs. (2.40) and (2.42) comprise the so-called Bloch system of differential equations for the magnetization of a sample in the presence of an external magnetic field $\vec{B}_{ext}$. These equations were first postulated by F. Bloch in 1946 [7]. This system may be written compactly as follows:

$$\frac{d\vec{M}}{dt} = \gamma \vec{M} \times \vec{B}_{ext} + \frac{1}{T_1}(M_0 - M_z)\hat{k} - \frac{1}{T_2}\vec{M}_\perp. \tag{2.45}$$

In the special case of a static homogeneous field aligned along the $z$-axis, i.e., $\vec{B}_{ext} = B_0\hat{k}$, this system may be written in matrix form as

$$\frac{d}{dt}\begin{pmatrix} M_x \\ M_y \\ M_z \end{pmatrix} = \begin{pmatrix} -\frac{1}{T_2} & \gamma B_0 & 0 \\ -\gamma B_0 & -\frac{1}{T_2} & 0 \\ 0 & 0 & -\frac{1}{T_1} \end{pmatrix}\begin{pmatrix} M_x \\ M_y \\ M_z \end{pmatrix} + \begin{pmatrix} 0 \\ 0 \\ \frac{M_0}{T_1} \end{pmatrix}. \tag{2.46}$$

The solution for this system may be easily found:

$$M_x(t) = e^{-t/T_2}[M_x(0)\cos\omega_0 t + M_y(0)\sin\omega_0 t],$$

$$M_y(t) = e^{-t/T_2}[M_y(0)\sin\omega_0 t - M_x(0)\sin\omega_0 t],$$

$$M_z(t) = M_z(0)e^{-t/T_1} + M_0[1 - e^{-t/T_1}].$$

In the limit $t \to +\infty$, these three components approach the following equilibrium values:

$$M_x(t) \to 0, \;\; M_y(t) \to 0, \;\; M_z(t) \to M_0.$$

In what follows, it will be useful to consider the Bloch equations for more general magnetic fields $\vec{B}_{ext} = (B_x, B_y, B_z)$. The matrix form of these equations is

$$\frac{d\vec{M}}{dt} = P\vec{M} + \vec{v}, \tag{2.47}$$

where

$$P = \begin{pmatrix} -\frac{1}{T_2} & \gamma B_z & -\gamma B_x \\ -\gamma B_z & -\frac{1}{T_2} & \gamma B_x \\ \gamma B_y & -\gamma B_x & -\frac{1}{T_1} \end{pmatrix}, \tag{2.48}$$

$$\vec{v} = \begin{pmatrix} 0 \\ 0 \\ \frac{M_0}{T_1} \end{pmatrix}.$$

This is again a first order (in time) linear system of differential equations in the components $M_i$. If we assume that $\vec{M}$ is spatially homogeneous in the unit volume, then the solution is

$$\vec{M} = e^{Pt}\vec{C} + P^{-1}\vec{v}, \tag{2.49}$$

where $C$ is a constant given by the initial condition:

$$\vec{C} = \vec{M}(0) - P^{-1}\vec{v}.$$

In the above discussion, $\vec{B}$ was assumed to be constant in time, yielding the solution in (2.49). In NMR experiments, however, $\vec{B}$ is usually configured to change with time, and in our experiment it will be piecewise constant in time. Therefore, the signal, which is proportional to $\vec{M}(t)$, will depend on the particular configuration of $\vec{B}$ used. An NMR "sequence" is specified by how $\vec{B}$ changes with time.

## 2.3 Configuring the magnetization field

In our experiments we use the so-called "CPMG" sequence [15] which has three components: (i) a "$\pi$ pulse", (ii) a "$\pi/2$ pulse" and (iii) "a dephasing period", described below, each of which spans a short period of time and over each of which $\vec{B}$ is constant. The particular order in which these components are applied in the sequence will be introduced in a later section. The parameters for the three components are:

1. The "$\pi/2$ pulse"

$$\gamma\vec{B} = (a, 0, 0), \quad for \ t_s \leq t \leq t_s + t_{\frac{\pi}{2}},$$

where $t_s$ is the time when the pulse starts, and

$$t_{\frac{\pi}{2}} = \frac{\pi}{2a}. \tag{2.50}$$

Because of the typical values of $a$ (see below), this time length is short, which explains why it is called a "pulse". Then $P$ in (2.48) becomes

$$P_1 = \begin{pmatrix} -\frac{1}{T_2} & 0 & 0 \\ 0 & -\frac{1}{T_2} & a \\ 0 & -a & -\frac{1}{T_1} \end{pmatrix}. \tag{2.51}$$

Let

$$X_1 = e^{P_1 t_{\frac{\pi}{2}}} = \begin{pmatrix} e^{-\frac{t_{\frac{\pi}{2}}}{T_2}} & 0 & 0 \\ 0 & 0 & e^{-\frac{t_{\frac{\pi}{2}}}{T_2}} \\ 0 & -e^{-\frac{t_{\frac{\pi}{2}}}{T_1}} & 0 \end{pmatrix}, \tag{2.52}$$

$$\vec{l_1} = (I - X_1)P_1^{-1}\vec{v}.$$

Then the behavior of $\vec{M}$ given by (2.49) is

$$\vec{M}_{end} = X_1\vec{M}_{start} + \vec{l_1}. \tag{2.53}$$

With Eq. (2.50) met, all terms containing $a$ in $X_1$ have either $\cos(at_{\frac{\pi}{2}})$=0 or $\sin(at_{\frac{\pi}{2}}) = 1$.

The parameter $a$ is typically greater than 1000 Hz in value. The relaxation time $T_1$ is typically greater than 50 ms [19]. With these assumptions the absolute value of every element in $\vec{l_1}$ is less than $0.00005M_0$. So one usually neglects $\vec{l_1}$ to give

$$\vec{M}_{end} = X_1\vec{M}_{start}. \tag{2.54}$$

This component of the sequence is called a "$\pi/2$ pulse" because $\vec{M}$ is rotated about the $x$-axis by $\pi/2$ radians (90 degrees) disregarding the exponential decays (see Figure 2.4).

2. The "$\pi$ pulse"

$$\gamma\vec{B} = (0, a, 0), \ \ for \ \ t_s \leq t \leq t_s + t_\pi,$$

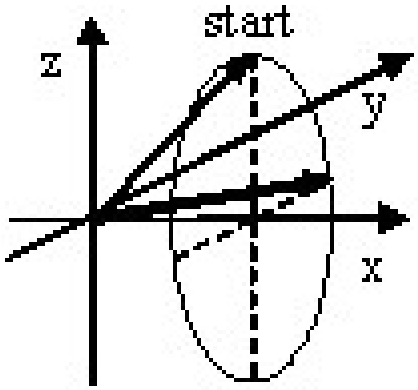


Figure 2.4: Rotation about $x$-axis for $\pi/2$.

where

$$t_\pi = \frac{\pi}{a}. \tag{2.55}$$

Then $P$ in (2.48) becomes

$$P_2 = \begin{pmatrix} -\frac{1}{T_2} & 0 & -a \\ 0 & -\frac{1}{T_2} & 0 \\ a & 0 & -\frac{1}{T_1} \end{pmatrix}. \tag{2.56}$$

Let

$$X_2 = e^{P_2 t_\pi} = \begin{pmatrix} -e^{-\frac{t_\pi}{T_2}} & 0 & 0 \\ 0 & e^{-\frac{t_\pi}{T_2}} & 0 \\ 0 & 0 & -e^{-\frac{t_\pi}{T_1}} \end{pmatrix}, \tag{2.57}$$

$$\vec{l_2} = (I - X_2)P_2^{-1}\vec{v},$$

then

$$\vec{M}_{end} = X_2\vec{M}_{start} + \vec{l_2} \tag{2.58}$$

Once again $a$ has to meet the duration requirement so that the cosine and sine

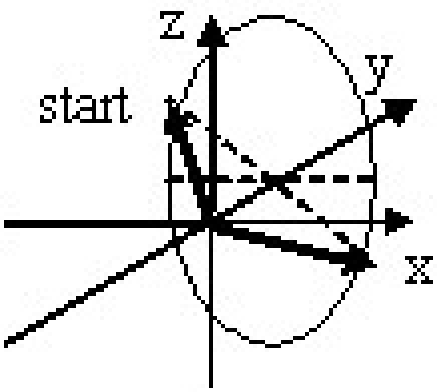


Figure 2.5: Rotation about $y$-axis for $\pi$.

terms in $X_2$ are 0 or 1. The same argument as for the $\pi/2$ pulse will show that $\vec{l_2}$ is very small. This component is called a $\pi$ pulse because $\vec{M}$ is rotated about $y$-axis for $\pi$ radians (180 degrees) disregarding the exponential decays (see Figure 2.5).

3. "Dephasing"

$$\gamma\vec{B} = (0,0,0),\ for\ t_s \leq t \leq t_s + t_E,$$

where $t_E$ is arbitrary but usually much greater than $t_\pi$.
$P$ in (2.48) becomes

$$P_3 = \begin{pmatrix} -\frac{1}{T_2} & 0 & 0 \\ 0 & -\frac{1}{T_2} & 0 \\ 0 & 0 & -\frac{1}{T_1} \end{pmatrix}. \tag{2.59}$$

Let

$$X_3 = e^{P_3 t_E} = \begin{pmatrix} e^{-\frac{t_E}{T_2}} & 0 & 0 \\ 0 & e^{-\frac{t_E}{T_2}} & 0 \\ 0 & 0 & e^{-\frac{t_E}{T_1}} \end{pmatrix}, \tag{2.60}$$

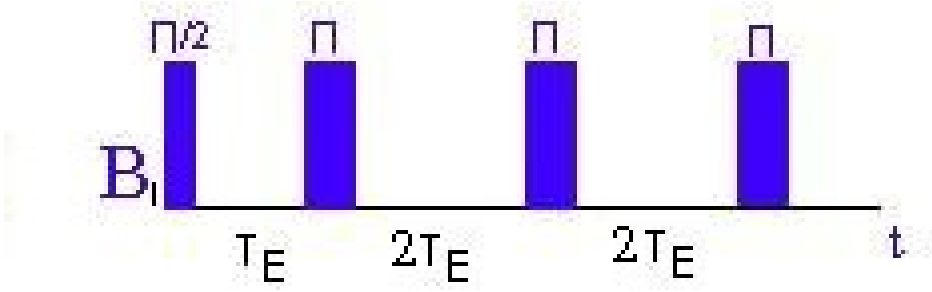


Figure 2.6: A CPMG sequence.

$$\vec{l_3} = (I - X_3)P_3^{-1}\vec{v}$$
$$\vec{M}_{end} = X_3\vec{M}_{start} + \vec{l_3} \tag{2.61}$$

Here the magnetization field terms $(a)$ does not appear in the $P_3$. As a result $\vec{l_3}$ is not negligible.

This portion of the sequence is called dephasing because the $x$ and $y$ components of the nuclear magnetization simply decay exponentially. Over this period $z$ component evolves towards $M_0$:

$$M_{z,end} = M_{z,start} + M_0(1 - e^{-t_E/T_1}). \tag{2.62}$$

The CPMG sequence is composed of the $\pi/2$ pulse, $\pi$ pulses, and dephasing periods that were described in the previous section. The order of these components is as follows: we begin with a "$\pi/2$ pulse" followed by $n$ applications of the sequence "dephasing-$\pi$-dephasing".

The initial condition is $\vec{M}(-t_{\frac{\pi}{2}}) = M_0(0, 0, 1)$ so that after the application of the first $\pi/2$ pulse, $\vec{M}(0) = M_0(0, 1, 0)$, by Eq. (2.54). Then after $n$ (dephasing - $\pi$ pulse

- dephasing) subsequences,

$$\vec{M} = X^n(\vec{M}(0) - \vec{r}) + \vec{r}, \tag{2.63}$$

where

$$X = X_3 X_2 X_3, \tag{2.64}$$

$$\vec{r} = (I - X)^{-1}(X_2 X_3 \vec{l_2} + X_2 \vec{l_3} + \vec{l_2}). \tag{2.65}$$

In our experiments, we shall be measuring the $y$ component of $\vec{M}$. From the definition of $X_2$ and $X_3$ we see that $\vec{r}_y$=0, so

$$M_y(n(2t_\pi + t_E)) = M_0 e^{(-n(2t_\pi + t_E)/T_2)}, \tag{2.66}$$

By setting $t_n = n(2t_\pi + t_E)$, Eq. (2.66) may be written as

$$M_y(t_n) = M_0 e^{-t_n/T_2}. \tag{2.67}$$

Note that the signal decays exponentially with time constant $T_2$. The goal will be to extract the value of $T_2$ from the experimental data.

## 2.4 Porous media relaxation time model

The relaxation times of water in pores varies because of a variety of factors, including the geometric confinement and water-surface interactions. Surface interactions describe the interactions between water and the solid surface. In most cases we are only concerned about the hydrogen bonds. With significant surface interactions, the CPMG signal may undergo the stretched relaxation [39]:

$$M_y(t_n) = M_y(0) e^{-(t_n/T_2)^\beta} \tag{2.68}$$

In this thesis we re not concerned about the strethed exponentials. The Zimmerman-Brittin two-site model [51] models the proton relaxation of water molecules in the pores by assuming there are a number of phases that are characterized by the relaxation times ($T_{1,2i}$ for the $i$th phase) and the molecules in these phases undergo stochastic exchanges. Some details of the physics of "fast-exchanges" of water molecules can be found in [6]. In case of very fast exchange, which is usually assumed in porous models, the observed relaxation behavior is equivalent to a single relaxation time system, with relaxation time $T_{1,2effect}$ as given by

$$\frac{1}{T_{1,2effect}} = \sum_i \frac{P_{1,2i}}{T_{1,2i}}, \tag{2.69}$$

where the $P_{1,2i}$ are constants specific to the system. This was obtained by using a matrix system that characterizes the fast-exchanges. As was the case for Eqs. (2.43) and (2.44), Eq. (2.69) is obtained by a consideration of various relaxation rates $R_i$. Generally the water in pores can be modeled approximately by a surface water layer and a bulk water, which results in a two-site model. Therefore, one may consider

$$\frac{1}{T_{1,2}} = \frac{a}{T_{1,2bulk}} + \frac{b}{T_{1,2surface}}, \tag{2.70}$$

where $a$ and $b$ represent the populations of the bulk and surface phases, respectively, and are functions of pore volume, pore surface area and surface layer thickness. This expression is also obtained by Brownstein and Tarr [8] by a model using equations in continuum mechanics. Because that the water molecules adjacent to the surface do not undergo as much as inter-molecular interactions as those in the center, the molecules in the surface layer would decay slower than those in the bulk water layer. So one expects

$$T_{1,2surf} < T_{1,2bulk}$$

Some discussions on this model and other models can be found in Holly [19]. In fact we are only interested in whether or not the pore water in a porous medium


Figure 2.7: The two-site model.

sample yields signals that have a single relaxation time. Judging from the research literature, there is, to date, no way to determine whether (2.70) is valid. This model is only served as an attempt to show what is happening in the pores. And hopefully if we can fit the parameters in the two side model from measurements of porous media with known structures, as done in [19], we may find a relation between these parameters to some variables describing the pore structure. We may then be able to predict the relaxation time value by the pore structure.

Another important fact people have learned from experiments is that $T_2$ depends linearly on the volume-to-surface ratio [10], that is, linearly on the pore diameter for spherical or cylindrical pores.

## 2.5 Statement of our problem

It was shown in Eq. (2.67), Section 2.1, that the solution to a CPMG sequence for one (spatially homogeneous) unit volume is

$$M_y(n(2t_E + t_\pi)) = M_0 e^{-n(2t_E+t_\pi)/T_2} = M_0 e^{-t_n/T_2}, \;\; n \in \mathbb{N},$$

for each unit volume. By definition, $M_0$ is proportional to the proton density of the unit volume, and so both $M_0$ and $T_2$ are functions of the location $(x, y, z)$ of the unit volume.

The magnitude of the NMR signal is proportional to the sum of the magnitudes

of $y$-component magnetizations of all protons. From Section 2.4, the $T_2$ relaxation may vary with the pore size. And the pore sizes in a sample may not be all the same. We may formulate the relaxation time distribution in either a discrete or a continuous way. In either case, the signal $f(t)$ produced by a sample will be given by

$$M_y(t) = \int_{\mathcal{D}} M_0(x, y, z) e^{-t/T_2(x,y,z)} dV,$$

where the integration is performed over the sample volume, $\mathcal{D} \subset \mathbb{R}^3$.

The discrete case applies to samples that have homogeneous pore sizes. Let us now mix $M$ different species of these samples so that the $T_2 = T_2^{(1)}$ in volume $V_1$, $T_2 = T_2^{(2)}$ in volume $V_2$, etc.. Then, for this mixed sample, the $y$-component magnetization will be given by

$$M_y(n(2t_E + t_\pi)) = \sum_{i=1}^{M} \int_{V_i} M_0(x, y, z) e^{-n(2t_E+t_\pi)/T_2^{(i)}} dV \tag{2.71}$$

$$= \sum_{i=1}^{M} A_i e^{-n(2t_E+t_\pi)/T_2^{(i)}}, \tag{2.72}$$

where $A_i = \int_{V_i} M_0(x, y, z) dV$. Since we are not concerned about the $T_1$ relaxation time, we shall simply rewrite Eq. (2.72) as

$$M_y(t) = \sum_{i}^{M} A_i e^{-t/T_i}, \tag{2.73}$$

where $t$ assumes the discrete values of $t_n = n(2t_E + t_\pi)$, $n = 0, 1, ...$

In the continuous formulation, we assume the existence of a continuous distribution of $T_2$ values with associated volume elements $\Delta V(T_2)$. This formulation can be produced by a calculus-type construction. We suppose that $T_a$ and $T_b$ are respectively the lower and upper bounds on the $T_2$ relaxation time. Now form a partition

of the interval $[T_a, T_b]$ into $M$ subintervals $T_a = T_2^{(0)} < T_2^{(1)} < ... < T_2^{(M)} = T_b$. (The partition need not be an equipartition.) Let $\Delta T_2^{(i)} = T_2^{(i+1)} - T_2^{(i)}$, $i = 0, 1, ...M-1$. Now let $\Delta V_i$ denote the set of $(x, y, z)$ values in one sample for which the $T_2$ value $T_2(x, y, z)$ lies within the interval $[T_2^{(i)}, T_2^{(i+1)})$, $i = 0, 1, 2, ...M-1$. Then the total signal may be approximated by the finite sum

$$M_y(n(2t_E + t_\pi)) = M_y(t_n) \approx \sum_{i=1}^{M} \int_{V_i} M_0(x, y, z) e^{-t_n/T_2^{(i)}} dV. \tag{2.74}$$

Note that we are approximating $T_2(x, y, z)$ as a piecewise constant function over the sets $V_i$. In other words, the expression on the right hand side of (2.74) may be considered as a kind of Riemann sum approximation. We now consider the limit $M \to \infty$ such that $\max_{0 \le i \le M-1} \Delta T^{(i)} \to 0$. With suitable assumptions on $T_2(x, y, z)$, e.g. piecewise continuous over $\mathcal{D} \subset \mathbb{R}^3$, the domain of the sample, we expect that the $M \to \infty$ limit of the Riemann sum exists and may be written as

$$M_y(t_n) = \int_{T_a}^{T_b} g(T_2) e^{-n(2t_E + t_\pi)/T_2} dT_2. \tag{2.75}$$

for some non-negative $g(T_2)$, where

$$g(T_2) = \lim_{\Delta T_2^{(i)} \to 0, T_2 \in [T_2^{(i)}, T_2^{(i+1)})} \int_{V_i} M_0(x, y, z) dV$$

exists. Once again, for simplicity, we shall write this as

$$M_y(t) = \int_{T_a}^{T_b} g(T) e^{-t/T} dT. \tag{2.76}$$

The signal $f(t)$ is proportional to the $y$-component magnetization of the sample, i.e. $f(t) = kM_y(t)$. So by letting $A_i$ and $g(T)$ absorb the constant $k$, $f(t)$ has the expression in Eq. (2.73) or Eq. (2.75).

In experiments, however, one always encounters noise coming from the electronics

system. A standard approach is to assume that the noise as a function of time, $n(t)$, is Gaussian white noise. And sometimes there is a vertical shift, or "baseline offset", which means that the numerical values of the data acquired has the property $f(t) \to C \neq 0$ as $t \to \infty$. Then the signal will be expressed by

$$f(t) = \sum_{i}^{M} A_i e^{-t/T_i} + n(t) + C. \tag{2.77}$$

or

$$f(t) = \int_{T_a}^{T_b} g(T) e^{-t/T} dT + n(t) + C, \tag{2.78}$$

Our goal is to extract $g(T)$ or $A_i$ and $T_i$ from $f(t)$. To find these, we will also need to find the $C$. In the discrete form, $M$ is sometimes unknown, in which case we have to determine a suitable value of $M$ from data. And regarding the presence of the noise term $n(t)$ in Eqs. (2.77) and (2.78), we adopt an additional condition in our approximation procedure: A solution to this inverse problem will make the residual noise term $n(t)$ as "white" as possible. We shall explain the motivation for this condition, which is borrowed from signal processing studies, below.

In other words, we shall separate the signal into two components, one of which is a sum or integral of exponentials, and the other, $n(t)$, is as close to a Gaussian white noise as possible. Furthermore, we will try to minimize the "energy" or $L_2$ norm of $n(t)$, which is the principle of least squares [41]. If there are multiple "good" solutions, we shall choose the simplest one, or the one that is closest to what we desire, based on previous knowledge. A "good" solution means that the residual $n(t)$ given by this solution demonstrates the characteristics of Gaussian white noise. Thus we will need a way to justify whether a discrete signal is a "good" Gaussian white noise. A white noise means that its Fourier spectrum is constant and the signal values are independent. A Gaussian noise means that the distribution density function of the signal is Gaussian. Such a condition is often used in signal processing [21]. To be strict in justifying these properties, statistical variables should be computed and

we should determine the ranges for these variables that are admitted by a "good" Gaussian white noise. But in our experiment, we shall only use our visual inspection for a crucial judgement.

Then the inverse problem for $T_2$ relaxation times can be stated in one of the following ways:

1. Problem P1

   Find $A_i$, $T_i$, $i = 1..N$ and $C$ so that

   $$||f(t) - \sum_{i=1} i^N A_i e^{-t/T_i} - C||_2 = [\sum_{n=0}^{N_t} (f(t_n) - \sum_{i=1}^{N} A_i e^{-t_n/T_i} - C)^2]^{1/2} \quad (2.79)$$

   is minimized, where $M$ is given.

2. Problem P2

   Find $N$, $A_i$, $T_i$, $i = 1..N$ and $C$ so that $N$ is the minimum positive integer such that when

   $$||f(t) - \sum_{i=1}^{N} A_i e^{-t/T_i} - C||_2 = [\sum_{n=0}^{N_t} (f(t_n) - \sum_{i=1}^{N} A_i e^{-t_n/T_i} - C)^2]^{1/2} \quad (2.80)$$

   is minimized, $f(t) - \sum_{i=1}^{N} A_i e^{-t/T_i} - C$ is a "good" Gaussian white noise.

3. Problem -

   Find $g(T)$ on $[T_a, T_b]$ and $C$ so that

   $$||f(t) - \int_{T_a}^{T_b} g(T) e^{t/T} dT + C||_2 = [\sum_{n=0}^{N_t} (f(t_n) - \int_{T_a}^{T_b} g(T) e^{-t_n/T} dT - C)^2]^{1/2} \quad (2.81)$$

   is minimized.

When $g(T)$ is comprised of a finite number of distinct Dirac delta functions, P3 becomes P1.

In this case, the continuous problem is most often solved in a discrete way, i.e., $g(T)$ is a discrete function on a sequence of equi-partitioned $T$ values, and the integral is approximated by a numerical integration. By a linear approximation of the integration, the third case may be stated alternatively as

4. Problem P4

   Find $g_i$ and $C$ so that

$$||f(t) - \sum_{i}^{N} g_i e^{-t/T_i} - C||_2 = [\sum_{n=0}^{N_t} (f(t_n) - \sum_{i}^{N} g_i e^{-t_n/T_i} - C)^2]^{1/2} \qquad (2.82)$$

   is minimized, for given $T_i$, $i..N$. $\Delta T = T_{i+1} - T_i$ is usually constant and $N$ is usually large. We would still call this the continuous problem, which is equivalent to P3, as opposed to the truely discrete problems.

We also demand $g(T)$ to be non-negative in order to be physically meaningful as a density function. Also in the case of measuring $T_2$ values that are distributed about some central values, we would like to know the peak locations in $g(T)$ and the total amplitude belonging to each peak. If this information cannot be obtained, then the solution is meaningless.

The extraction of discrete relaxation times $T_i$ and associated coefficients $A_i$ from Eq. (2.77) or continuous distribution $g(T)$ from Eq. (2.78) are examples of the classical "separation of exponentials" problem that is encountered in a number of scientific areas. The inverse problem and various numerical methods devised to solve it are discussed in more detail in Chapter 3.

In our experiments, we have $2t_E + t_\pi \approx 0.2$ms, $t_{max} < 1000$ ms. The noise level is about 400<var$[n(t)]$ <900 for experiments on a 30 MHz machine, and the signal amplitude is about $8000 < f(0) < 20000$. The unit of these amplitudes depends

on the machine giving the signal, and is proportional to the total magnetization of the sample. We will use the millisecond as the unit of time for both $t$ and $T$, unless otherwise noted. The $T_2$ times of the samples used in this study lie in the interval $[10, 100]$. The above values of parameters are assumed specifically for our experiments. However the analyses in this thesis are valid for all $t \geq 0$, and the results for $T \in [10, 100]$ can be extended to other intervals of $T$. In fact $T_2$ in any measurement has an upper limit of 3600 ms which is the $T_2$ of pure water at a temperature of 25 °C. And a $T_2$ less than 10 ms is not expected in the present system under study.

In this thesis we will present and analyze the experimental data sets obtained from the following six experiments:

1. Water. Paramagnetic copper sulphate ($CuSO_4$) has been added in order to decrease the $T_2$ time from that of pure water. The solution is assumed to be homogeneous in the tube, so that there should be a single relaxation time. The 30 MHz frequency identifying the machine refers to $\frac{\omega_0}{2\pi}$, which depends on the magnetic field strength $B_0$ of this machine. The signal for this experiment is plotted in Figure 2.8.

2. The above sample measured in a 500 MHz machine. (This signal is plotted in Figure 2.9 as another example.)

3. Porous glass beads with pores of a fixed cylindrical diameter – 237 Å. The pores are saturated with clean water (the procedure is described in a later section). This measurement was made with the 30 MHz machine. Based on the two-site model in Section 2.4, there should be a single relaxation time. In fact, the pore diameter may not be homogeneous and should have a distribution around the mean value. If the distribution is wide, the the curve will not be well-fitted by a single-component exponential decay and should be fitted to a continuous distribution.

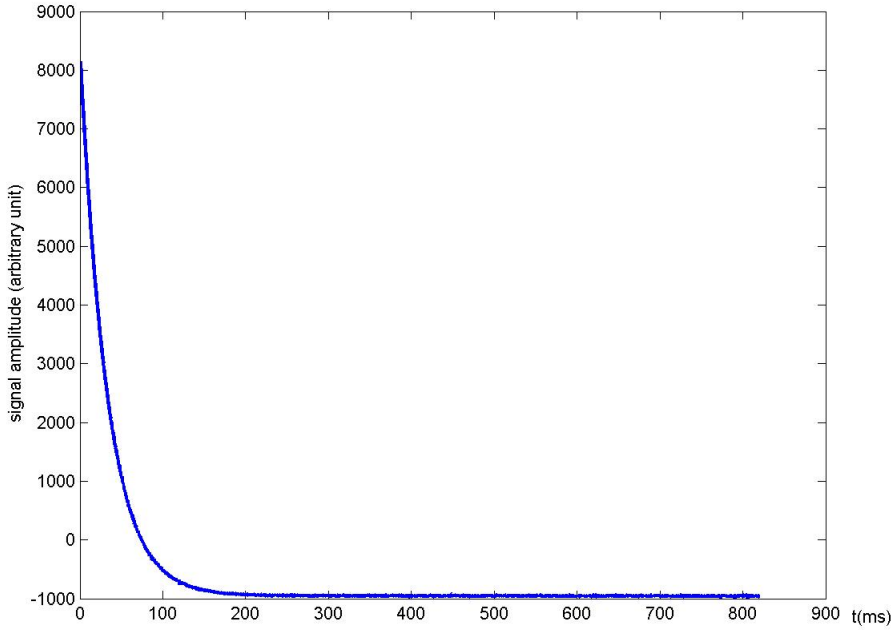


Figure 2.8: The first data set.

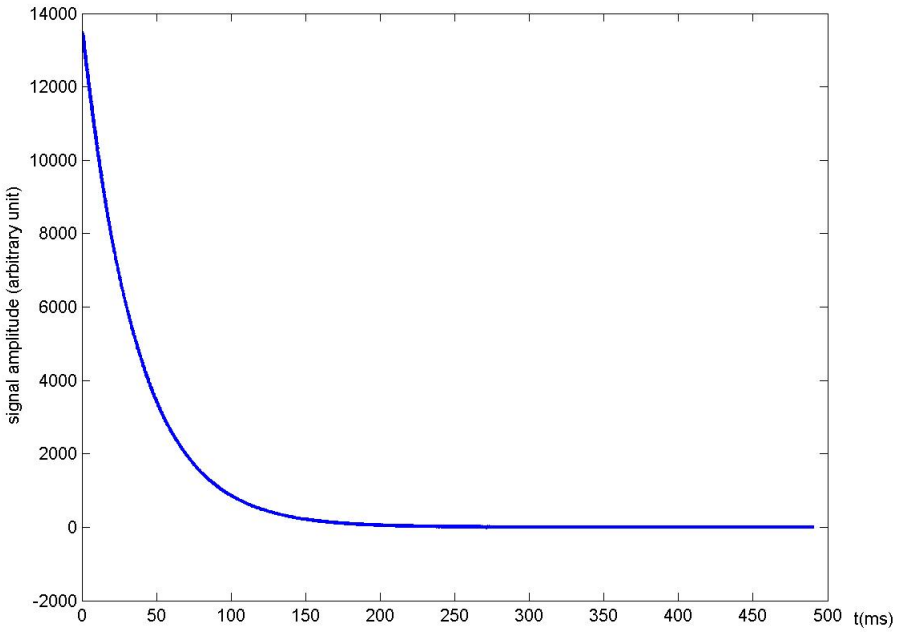


Figure 2.9: The second data set.

4. Saturated porous glass beads with controlled pore diameter being 491 Å, measured by the 30 MHz machine.

5. Saturated mixture of the 237 Å sample and the 491 Å sample with the proportion of their total pore volumes in the mixture being about 6:5, measured by the 30 MHz machine. Based on the formulation of the problem in the beginning of this section, this curve should be fitted to a two-component exponential decay. If the pore diameters have distributions, the data should be fitted to a continuous distribution.

6. Another saturated mixture of the above two species with the proportion in the pore volumes being about 1:3, measured by the 30 MHz machine.

The experimental procedure employed to obtain these data sets will be explained in Section 2.7.

## 2.6 Possible sources of systematic errors

In our statement of the problems in the previous section, we assumed the existence of only Gaussian white noise. In fact there is a large possibility that systematic errors can also be present. The systematic errors can be due to diffusion, stretched exponentials (Eq. (2.68)), off-resonance, pulse length error, or problems that are accidental or specific to the machine. Strictly speaking, if the factor is from the physical system, or the problem is detectable and possible to be corrected, it is not a systematic error. In this way only the problems specific to the machine can be called a factor of systematic errors. However here by systematic errors we mean the factors that could invalidate the sum-of-exponentials model.

Problems specific to the machine are generally non-predictable, but may possibly be identified when different machines give different data for the same sample, and quantified through caliberation procedures. We had some mearurements from the 30

MHz machine, with no sample in it, hoping to have a look at the systematic errors due to the coils only. We found that the systematic errors due to the coils only is not the same all the time. But by adding these errors to clean phony signals and fitting this data curve, the results do not differ from those by fitting the clean signals by a significant amount. So we assume that the systematic errors coming from the electronic system is negligible. The shape of these systematic errors is sometimes like a straight line with a small slope, sometimes a small tilt at the beginning of the signal, and sometimes both.

The possibility of stretched exponentials is ignored in this thesis.

Diffusion effects can be modeled by the Bloch-Torrey equations [15]. The solution with diffusion for the CPMG case is discussed by several authors, specifically,

$$M_y(t_n) = Ae^{-t_n/T_2 - kt_n^3}, \tag{2.83}$$

by Carr and Purcell [9] and Kaiser[20], and

$$M(t_n) = Ae^{-t_n/T_2 - kt_n}, \tag{2.84}$$

by Kaiser for very fast diffusion, by Torrey [42] assuming the $x$ and $z$ component magnetization at $t = 0$ is very small and by Haacke [15]. In the above expressions, $k$ is linear in the molecular self diffusion constant $D$ for water, and quadratic in all of the field gradient $G$, the gyromagnetic ratio $\gamma$ for proton in water, and the dephasing length $T_E$.

CPMG is designed for circumventing the effects of diffusion, through magnetic field gradients caused by local fluctuations [15]. Other than this, the only possibility that causes diffusion is the density gradient of protons. But the diffusion caused by the density gradients is so fast, that the system must finally go to an equilibrium in which either no density gradient exists or the density gradient does not cause diffusion because of strong chemical forces [10]. In such an equilibrium, $G$ is zero

and so is $k$. As a result, we are not concerned about diffusions.

Off-resonance and pulse length error can easily occur. It has been mentioned that the Bloch equations are written in a frame rotating about $z$-axis in a required frequency. For resonance, there is a required relation among the stationary field strength, the rotating frequency and the nuclear gyromagnetic ratio, given in Eq. (2.9). If this relation is not met, then the values of $\vec{B}$ in Section 2.3 will be nonzero in the $z$-direction. This is called off-resonance. If the time length requirements for the pulses in Section 2.3 are not met, then the $\cos(at_{\pi/2,\pi})$ and $\sin(at_{\pi/2,\pi})$ terms in the matrices $X_{1,2}$ will not become 0 or 1. This produces the pulse length error. In either cases, the solution to the CPMG sequence can be simulated by solving the Bloch equations with these "off-resonance" and "pulse length error" parameters.

Vold *et al.*. [44] have shown that the CPMG measurement due to off-resonance and pulse length error will be

$$M_y(t_n) = Ae^{-t_n/R_a} + B\cos(mt_n)e^{-t_n/R_b} + C. \tag{2.85}$$

The parameters in this expression have very complicated dependence on the experiment configuration parameters and the relaxation times. Here is a simulation of the signals by directly computing the $X_i$ matrices in Section 2.3. The parameter $a$ is assume to be 30 MHz and $T_2$ is assumed to be 36 ms. The values of other parameters are listed in Table 2.2.

By Section 2.3 the solution to CPMG is

$$\vec{M}(t_n) = X^n(\vec{M}(0) - \vec{r}) + \vec{r}, \tag{2.86}$$

where

$$\vec{r} = (I - X)^{-1}(X_2X_3\vec{l_2} + X_2\vec{l_3} + \vec{l_2}),$$

$$X = X_3X_2X_3.$$

| % error in $t_\pi$ | $T_1$=0.1s,b=1k | $T_1$=0.1s,b=10k | $T_1$=1s,b=10k |
|---|---|---|---|
| 0 | 36.0001ms | | |
| +2 | 36.0003ms | | |
| +4 | 36.0094ms | 36.0671ms | 36.1018ms |

Table 2.2: Fitted $T_2$ for different combinations of errors.

For $M_y$, only the second row of $X^n$ is relevant. For each combination of parameters, we calculate $M_y(t_n)$, fit the curve with one component using LSQCURVEFIT in MATLAB (Table 2.2) and plot the residuals (Figure 2.10). We assumed that the $x$ and $z$ components of $\vec{M}(0)$ are zeros. In fact, a calculation would show that the contribution of an error $\epsilon$ at $t = 0$, which is $X^n\vec{\epsilon}$, is negligible if the amplitudes in the error vector are less than $0.0001M_0$.

The results show that with only off-resonance condition, the data has negligible oscillations (beats). The presence of pulse length error dilates the amplitudes of the oscillation. The amplitudes of the oscillation also increase with the level of off-resonance. The difference in $T_1$ does not affect the results very much. In all of the experiments, the fitted relaxation times do not have significant differences, and the maximum amplitude of the oscillation is about $0.002M_0$. This amount of oscillation is not even observable in the presence of Gaussian white noise $n$ with $\sigma[n] = 0.0025M_0$ (Figure 3.4 in Section 3.1), which can represent the noise level encountered in our physical experiments. However, it can be detected by doing a Fourier transform on the residual. If off-resonance or pulse length error is larger than the simulated values, the errors in the data would become larger and may cause errors in fitted parameters or produce weird residual shapes. For example when the error in the $\pi$ pulse is +25%, the magnitude of oscillation in the residual can be as large as $0.1f(0)$. We will assume that the off-resonance and pulse length errors in our physical experiments are much smaller than our simulated values.

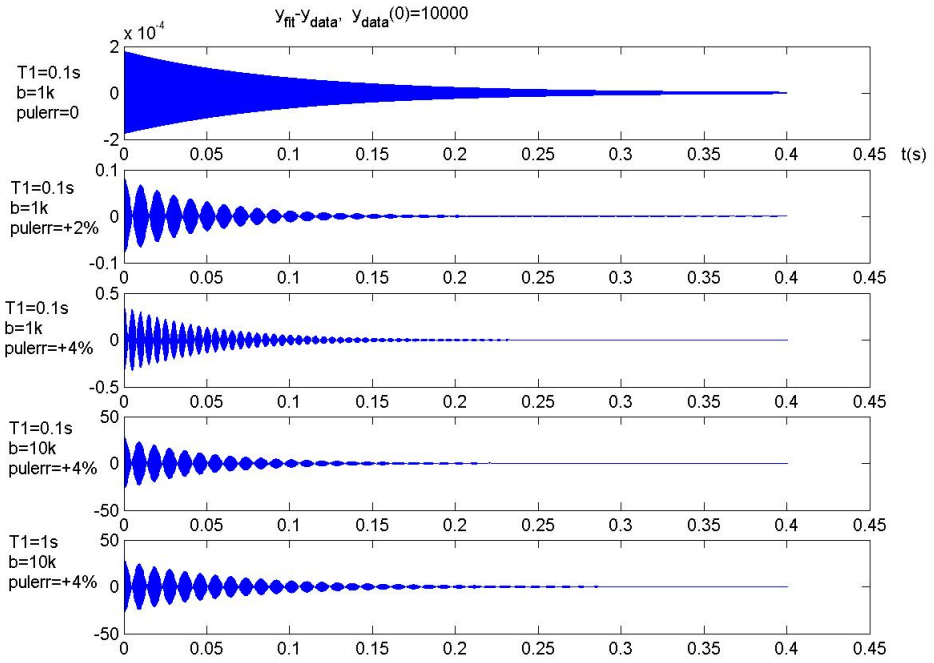


Figure 2.10: Residuals in fitting the curves with different combinations of errors in the experiment configurations.

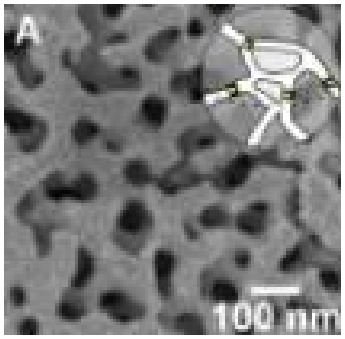


Figure 2.11: Scanning electron micrographs of controlled porous glass (CPG) with a pore diameter about 55 nm. (From J. M. Ha, J. H. Wolf, M. A. Hillmyer and M. D. Ward, J. Am. Chem. Soc., 126, 3382 (2004).)

## 2.7 Experimental

In this section we introduce the experimental procedure through which the data sets are obtained. The procedure includes sample preparation, measurement and sampling of the signal. For the data sets 1 and 2 listed in Section 2.5, the samples were just prepared by simply adding chemicals into water. The procedure described below was applied for porous glass gel samples.

### Sample preparation

In our experiments we used two species of porous silica glass gel with controlled pore diameters of 237 Å and 491 Å (Figure 2.12). These materials are glass grains that have many cylindrical pores (which may be interconnected) inside. The pore diameter refers to the diameter of the cylinder. The diameters of pores for each species may have a distribution within 10% of its mean diameter. Figure 2.11 is a picture of such a porous glass with pore diameter of 55 nm.

In our experiments we saturate the samples with water in an effort to ensure that all pores in the sample are filled with water. To make sure that the sample is saturated, we put the samples in a beaker of water and placed the beaker into


Figure 2.12: Glass gel sample.

a container that is connected to vacuum pump (Figure 2.13) via a valve. We then opened and closed the two valves for three times. When the valve is open, air is being removed from the container. As a result, the air in the pores, originally at atmospheric pressure, expands and we see air bubbles rising to the surface of the water. After the valve is closed, a connection to the container is opened, allowing air to enter the system. As a result, water enters the pores. The procedure is repeated.

After the sample is saturated with water, it is taken out of the beaker and put on filter paper to be dried. At this time the glass beads stick together because of surface water on the beads. The sample is sufficiently dried once the glass beads are fully separated as dry sand. They should then be immediately transported to a tube and the tube is sealed with parafilm (a kind of plastic material) so that the pore water does not evaporate (Figure 2.14). A schematic illustration is showed in Figure 2.15 for the prepared sample.

When mixing the two species, the saturation procedure is the same. But before saturation the samples must be weighed according to the proportion of pore volume we desire. The pore-volume-to-mass ratios for each sample are different. The information of this ratio is provided by the manufacturer of the glass gels. This ratio


Figure 2.13: The pump system that saturates the sample. The beaker containing the sample is placed in the glass container on the picture.

Figure 2.14: The completed sample which is contained in a small tube.

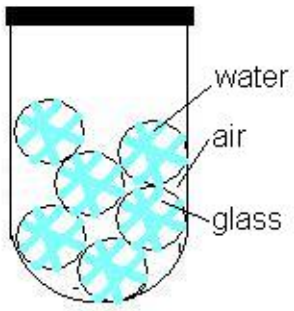


Figure 2.15: A schematic illustration of the completed sample.

is 0.95 ($cm^3/g$) for the 237 Å sample and 0.85 for the 491 Å sample. Assuming saturation of the sample, the proportion of water volume can be calculated by these ratios and the weights of the samples (Figure 2.16). After they are weighed, the two species are put together into the beaker for saturation.

## Measurements

Most of the measurements were done in a 30 MHz machine, which means that the machine has a magnetic field for which the parameter $\omega_0$ in Section 2.1 is $2\pi 30$ MHz. The tube containing the sample is inserted into the central coil (Figure 2.17). The frequency can be adjusted to the accuracy of 1 Hz (Figure 2.18). The values of $T_\pi$, $T_{\pi/2}$, $T_E$, number of measurements, repeating time between measurements and the length of the signal are set up on the computer by an in-house program. In our experiments, $T_\pi$ is 3.4 $\mu$s, $T_{\pi/2}$ is 1.7 $\mu$s, and $T_E$ is 100 $\mu$s. From signal processing, we know that the signal-to-noise ratio of noisy signals (assuming additional Gaussian white noise) may be increased by averaging over repeated measurements. In fact, we know that for measurements with random Gaussian white noise, with such averaging of repeated measurements the expectation value of the signal to noise ratio is proportional to the number of measurements. In our experiment the signals are

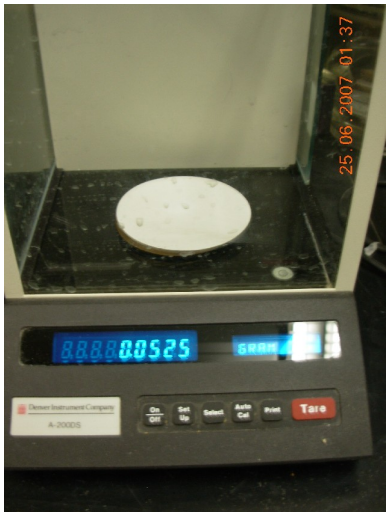


Figure 2.16: The two species are weighed to make a desired proportion in their pore volumes for the mixture.

obtained by averaging 410 measurements, and the repeating time between measurements is 15 s. The time interval of the signals are typically 1 s. But there are always large systematic errors in the second half of the signal (which is a problem of our machine), so in our data analysis we use only the portion of the signal for $t \in [0, 500]$ (ms). The signals are acquired by a GAGE CompuScope 1012 board.

## Sampling of signals

The raw signals (Figure 2.19) obtained from the signal acquisition board are sampled with a spacing of 50 $\mu$s. The time spacing between spin-echoes, i.e., $(T_E + 2T_\pi)$ is about 200 $\mu$s. So we need to pick the spin-echo points from the raw signal. This is done also by an in-house program, in which we set the spacing of the time points for our signal (Figure 2.20 and 2.21), and then the program outputs suitable points picked out from the raw signal. If the input spacing is not set up properly, the output signal will have a beat pattern.


Figure 2.17: The 30 MHz NMR machine, housed in the UW Department of Physics building.

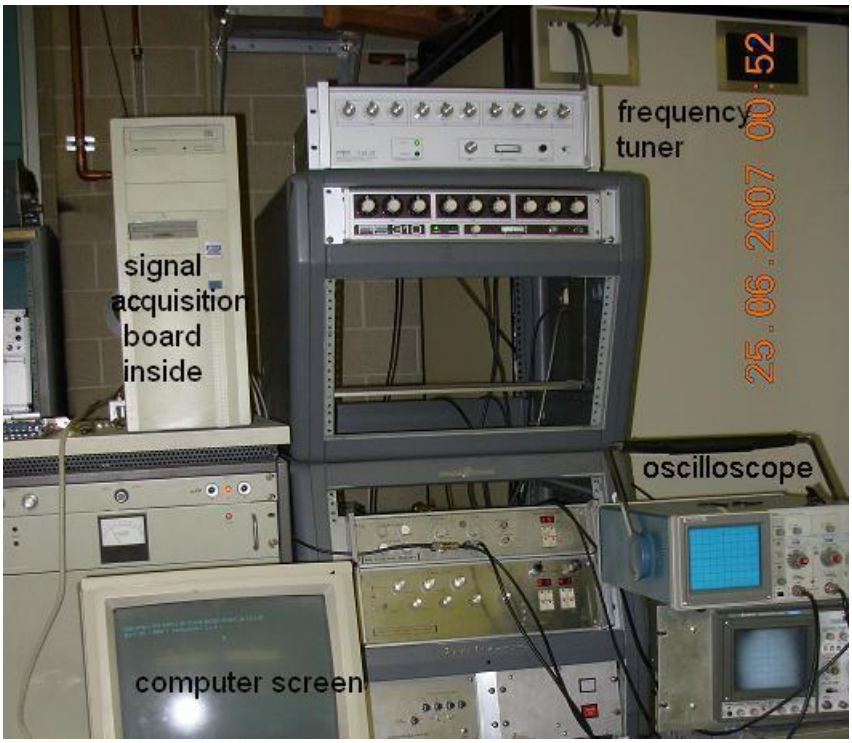


Figure 2.18: The equipment for configuration and signal acquisition.

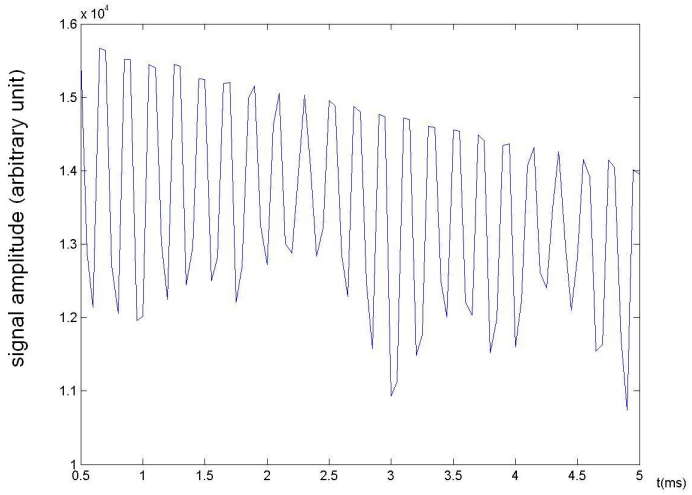


Figure 2.19: A small portion of the raw signal given by the signal acquisition system. This signal is for data set 5 in Section 2.5.

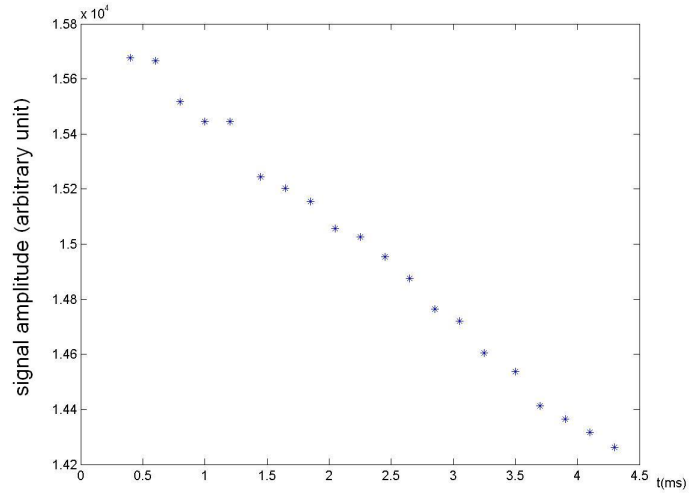


Figure 2.20: A small portion of the signal to be analyzed after selecting suitable time points from the raw signal.

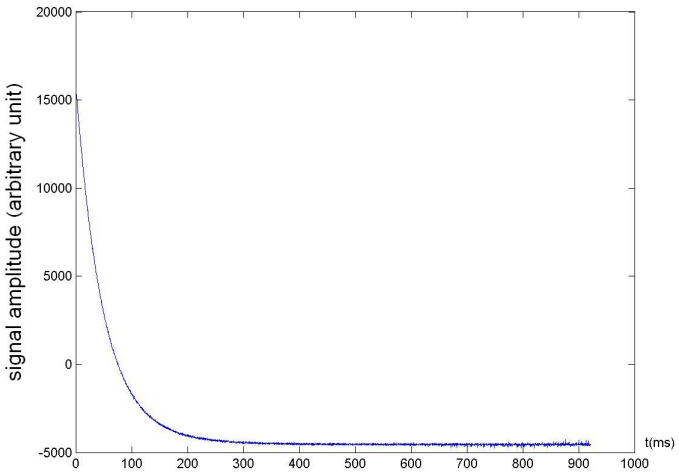


Figure 2.21: The full signal to be analyzed.

# Chapter 3

# A Review of the Problem of "Separation of Exponentials"

## 3.1 Numerical methods

The classical problem of "separation of exponentials" [25] can be stated as follows: Given a function $f(t)$ (or data points), and an $N > 0$, find the best approximant of $f(t)$ as a linear combination of the exponentially decaying terms, i.e.,

$$f(t) \approx \sum_{i=1}^{N} A_i e^{-\lambda_i t}. \tag{3.1}$$

By setting one of the $\lambda_i$'s to be zero, say $\lambda_1 = 0$, the sum in (3.1) may accomodate a constant term, $A_1$, which is also known as the "baseline offset". In this case, the sum in (3.1) approaches $A_1$ as $t \to +\infty$. The problem of extracting the parameters $A_i$ and $\lambda_i$ is encountered not only in NMR data analysis, but also encountered in many other problems, for example, radioactive decay, fitting statistical data to a Poisson distribution, blood tracer activity, transient signal from sensors [14], and fluorescence decay.

The problem of inverting a Laplace transform from real and discrete data is a more general form of this problem. A discrete distribution may be viewed as a continuous distribution that consists only of $\delta$-functions. Recall that the basic inverse Laplace transform requires the analytical form of the function so that the inversion integral can be performed in the complex plane. The inversion of the Laplace transform from real discrete data is normally done to find a solution on an array of disretized $\lambda$. By the change of variable $\lambda = 1/T$, the separation of relaxation times problem

$$f(t) = \int_0^\infty g(T)e^{-t/T}dT, \;\; g(T) = 0 \;\; for \;\; T \in [0, T_a] \cup [T_b, \infty) \tag{3.2}$$

becomes the Laplace transform of a localized function $p(\lambda) = g(1/\lambda)/\lambda^2$. We denote the integral equation (3.2) to be

$$f(t) = S[g], \tag{3.3}$$

as opposed to the Laplace transform $f(t) = \mathscr{L}[p]$.

Below is a review of five methods that have been devised to solve this problem: Prony's method, Padé-Laplace, iteration on the unknown parameters, direct matrix inversion, and integral transforms. The first three consider the discrete form of the problem, and the latter two consider the continuous problem. However, if the true distribution is discrete, the latter two are able to give approximate solutions. There is no method that is designed particularly for determining the number $N$ of components in (3.1). It is claimed that some methods have the ability to tell whether an assumed value for $N$ is sufficiently good, and guarantee some level of accuracy for the solved components. Considering the nature of the problem, it is, in some cases, meaningless to discuss the accuracy and how many components there actually are. Direct matrix inversion can be accompanied by regularization to find certain types of solutions.

### 3.1.1 Prony's method

To introduce Prony's method and, later, the direct matrix inversion method, we denote $\xi_i = e^{-\Delta t/T_i}$, supposing that $t_n = n\Delta t$, for $n = 0...N_t$.

Then the sum of exponentials in (3.1) will become

$$\tilde{f}(t_n) = \sum_{i=0}^{M} A_i \xi_i^n. \tag{3.4}$$

Prony's method was invented in 1795 [12], and was discussed by Lanczos in his textbook [25]. The method is based on the fact that a function in the form (3.4) is the solution of a recursion equation $\tilde{f}_{n+M+1} = \sum_{i=0}^{M} c_i \tilde{f}_{n+i}$ for some $c_i$'s. If we could determine the $c_i$'s from data, then the $\xi_i$'s are the roots of the equation

$$1 + c_M x + c_{M-1} x^2 + ... + c_1 x^{M-1} + c_0 x^M = 0. \tag{3.5}$$

One method of finding $c_i$'s is to minimize the norm of the vector

$$\vec{\epsilon} = \begin{pmatrix} f_0 & ... & f_M \\ f_1 & ... & f_{M+1} \\ & \vdots & \\ f_{k-M} & ... & f_k \end{pmatrix} \vec{c} - \vec{f}, \tag{3.6}$$

where $\vec{f} = (f(t_0), f(t_1), f(t_2)...f(t_{N_t}))$ is the signal. Similar with a $\lambda_i$ being 0 in (3.1), the baseline in (3.4) is equivalent to a $\xi_i = 1$. In Prony's method, this means that one of the $\xi_i$ should have the value 1 in the final solution. System (3.6) can be solved by singular value decomposition [23].

Alternatively, we could assume $\tilde{f}_n = \sum_{i=0}^{M} c_i \tilde{f}_{n+i+1}$, and the expressions for (3.5) and (3.6) should change accordingly. Fitting (3.4) with the two directions of recursion are called forward prediction and backward prediction, respectively, in the linear

prediction problem considered in signal processing [31]. In the forward case, the roots to (3.5) will fall inside the unit circle on the complex plane [31], and so can be found by searching. In the backward case, the roots can be solved with better accuracy though solving for them is harder. Because of the difficulty in finding the roots when the order is higher, this method is used only for small $M$.

The disadvantages with the iteration method are that: (1) It is sensitive to noise. (2) A small change in $c_i$ can produce large changes in the roots to (3.5). (3) It is difficult to find good $c_i$'s that make (3.6) a small vector as well as the roots to (3.5) real.

For a detailed introduction to the iteration method, as well as linear prediction in speech, see [31].

### 3.1.2 Padé-Laplace method

The Padé-Laplace method is designed for the discrete problem (P1 in Section 2.5), and involves the identification of poles of a function. Taking the Laplace transform of a sum of exponentials gives

$$h(p) = \mathscr{L}[\sum_{j=1}^{N} A_j e^{-t/T_j}](p) = \sum_{j=1}^{N} \frac{A_j}{p - 1/T_j}. \tag{3.7}$$

Thus we are done if we can fit $h(p)$ instead of $f(t)$. To fit $h(p)$, we notice that the last expression in Eq. (3.7) is a rational function in $p$, i.e.,

$$h(p) = \frac{\sum_{s=0}^{N-1} a_s p^s}{\sum_{v=0}^{N} b_v p^v}. \tag{3.8}$$

Choosing a $p_0$ and performing a Taylor expansion of $h(p)$ to order $L + N$ by taking numerical derivatives of $h(p)$, we can produce a polynomial approximation of $h(p)$ around $p_0$. And then $a_s$ and $b_s$ can be computed by the recursive algorithm

of Longman [28]. The baseline of the signal corresponds to one of the $T_i$ being at infinity, i.e., a pole of $h(p)$ at 0.

This method is found to be very robust with respect to noise [50], and able to determine $N$ in the sense that when $N$ is larger than necessary, the extra $a_s$'s and $b_v$'s will be zeros [50]. In [50], the method was tested with noise but only for sums whose exponential terms were very different. As a result, the author of this thesis does not know how it works with a sum of similar exponentials. The difficulty is the choice of a suitable $p_0$, which can be done at least by search, and a number of people have derived better ways for determining $p_0$ [14]. The main algorithm for Padé-Laplace is provided in [3].

### 3.1.3 Iteration of parameters

In this method, the iterated parameters include the relaxation times as well as the amplitudes, and so it solves a nonlinear fitting problem. MATLAB has a built-in function LSQCURVEFIT that solves any least square fitting for a small number of parameters. By default, it uses an interior-reflexive Newton method and a subspace trust region method. The gradient computed for iteration is the preconditioned conjugate gradient. In some other software such as *Origin* [52], the least squares fitting algorithm uses a Marquart-Levenberg scheme.

The advantages of this method are that it works well with noise, and that it is accurate in solving for a small number of components. The disadvantage is that it is not accurate for solving a large number of components, for example, more than four components in MATLAB.

There is another advantage of this method in the presence of systematic errors. This method converges to different results by using different initial values. Without systematic errors, of course, we would like to determine the optimal solution. With systematic errors, however, a non-optimal solution may be closer to the true solution than an optimal one. In such cases, we may find more possibilities for the true

solution by examining non-optimal solutions, as the true solution may not be the optimal solution.

### 3.1.4 Direct matrix inversion

Using Eq. (3.4), we could minimize the norm of $\tilde{f}(t_n) - f(t_n)$ assuming a large number of $T_i$'s, i.e., solve the system

$$\begin{pmatrix} 1 & 1 & ... & 1 \\ \xi_1 & \xi_2 & ... & \xi_M \\ & : & : & \\ \xi_1^k & \xi_2^k & ... & \xi_M^k \end{pmatrix} \vec{g} \approx \vec{f}. \tag{3.9}$$

This is mostly suitable for determining $g(T)$ in the continuous problem. Solving the system in Eq. (3.9) requires a large amount of work. In this process, a singular value decomposition or iteration may be used. The non-negative least squares (NNLS) or linear programming (LP) [48] schemes mentioned in the literature falls into this category, both of which can be regularized, that is constrain on the first/or second derivatives, to find certain type of solutions. In this way the solution can be made as smooth as desired [48].

The non-negative least squares method solves for $\vec{g}$ vectors with non-negative elements in (3.9). Therefore it is particularly suitable for our physical problem, as other methods solving the continuous problem may fail to constrain the solutions to be non-negative. The algorithms of NNLS usually follow the work of Lawson and Hanson [27]. This algorithm tends to give separated delta functions even for smooth distributions if no regularization is used. MATLAB now has a built-in NNLS function called LSQNONNEG. This author performed a few experiments in MATLAB and found that the function does not treat the baseline term well when it is included in the matrix, and so a baseline has to be determined beforehand.

Some disadvantages of this method are: (1) It is not as accurate in solving the

discrete problem as a search or iteration procedure over all the unknowns, because it usually gives more components than there actually are, with some components split and some components merged, especially when the fixed $T$ points skip over the true locations (Example 1 below). (2) For the same reason, it is not able to determine the minimum number of components, since the number of delta functions in the solutions given by this method cannot be constrained. In comparison, other methods allow us to prescribe the number of components and increase it until the solution is good enough. (3) For the continuous problem, if the distributions are not as simple as a couple of thin peaks, the algorithm may require a long time when a suitable level of regularization (that avoids the solution to be separated delta functions) is used (say one minute for 100 relaxation time points, and more than six minutes for 200 relaxation time points), and sometimes the algorithm would fail.

**Example 1.** ***NNLS solving a discrete distribution when the discretized $T$'s jump over the locations of the true relaxation times***
*Let the data curve be given by*

$$f(t) = 2000e^{-t/40.5} + 2000e^{-t/50.5} + 2000e^{-t/70.5}.$$

*We sample from this curve to produce data points, where $t$ is equi-partitioned with $\Delta t$ being 0.2 ms and the number of time points is 2500. Then we solve the continuous problem P3 by assuming $T = (10, 11, 12...100)$ (ms). Let $B$ be the matrix of $\xi$'s in 3.9. Thus $B$ is a 2500 by 91 matrix.*

*The MATLAB command is*

$$[A, p1, p2, p3, p4] = lsqnonneg(B, f);$$

*where $A$ is the solution vector, p2 is the residual, and p4.iterations is the number of iteration steps (p4 is a structured variable and p4.iterations is a member of p4). The result is a residual to be of order $10^{-3}$ and the number of iteration steps is 17.*

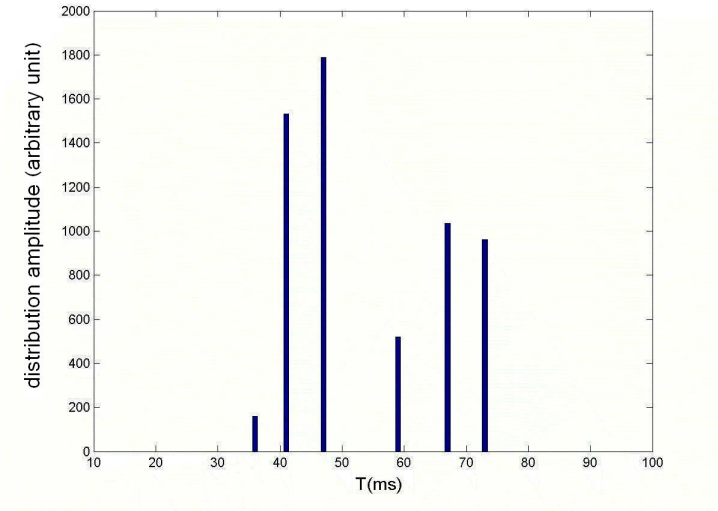


Figure 3.1: The solution solved by NNLS for the three component distribution of Example 1.

*Figure 3.1 shows that the result solved by NNLS gives six components. Given such a solution, we cannot tell whether any of the adjacent components should be combined, or whether there should be a component around T =60.*

**Example 2.** ***A failure of the NNLS algorithm in MATLAB***

*Consider the following distribution of* $T$*,*

$$g(T) = A(\sin((T - 40)/40 \times 2\pi) + 1) \tag{3.10}$$

*for* $T \in [10, 100]$*, and a signal* $f(t) = S[g]$*. This distribution is plotted in Figure 3.2.* $A$ *is a scaling factor so that* $f(0) = 10000$*. The result obtained by LSQNONNEG from* $f(t)$ *in MATLAB is plotted in Figure 3.3. The algorithm fails to give a nonnegative solution.*

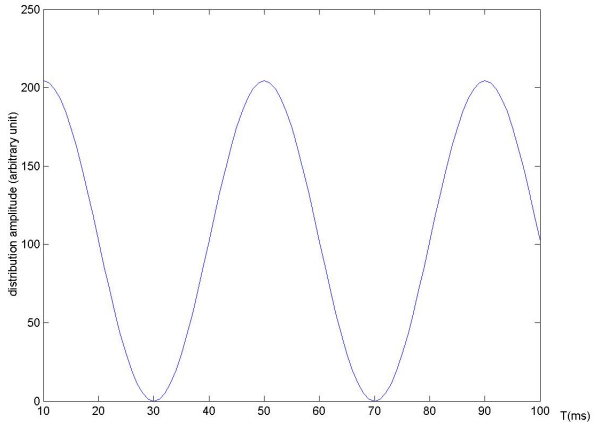


Figure 3.2: An example that NNLS fails. This the true distribution.

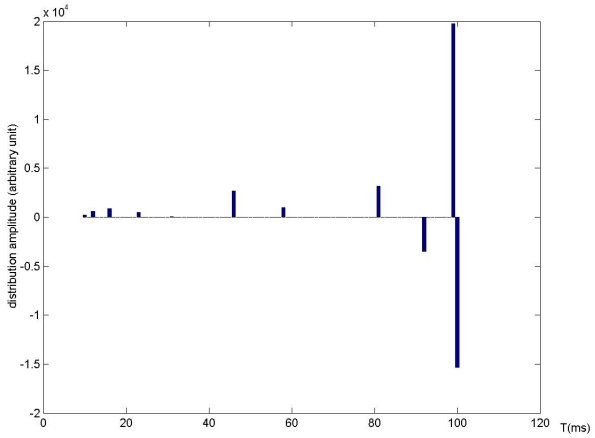


Figure 3.3: The solution solved by NNLS for the distribution plotted in Figure 3.2.

### 3.1.5 Integral transforms

As the name suggests, these methods are based upon the computation of integral transforms of the data. Being different from the Padé-Laplace method, the solutions for these methods result directly from some global transformation. Without matrix inversions, they allow more data points for the $T$ values than the matrix inversion method. However, they still lack accuracy for the discrete problem in which case the solution will be composed of continuous peaks centered at discrete relaxation rates.

All of the integral transform methods are ways of performing the inverse Laplace transform from the real axis as adapted to the relaxation time problem. The inversion may use the Mellin transform [2] or the Gardner transform [38], both of which make use of Fourier transforms. Inversion may also be performed by other suitable techniques, for example Ramm [37] gave a closed expression for inverting the Laplace transform from the real axis.

For the relaxation time problem, the integral methods are generally not suitable, because they usually use nonlinear changes of variables. As a result, the accuracy of the solutions will be biased to only a part of the domain of $g$, and sometimes the data sets need to be interpolated to generate non-equipartitioned time axis. The other disadvantages include: (1) They are not as robust as Padé-Laplace in dealing with noise [14], and (2) the solutions cannot be regularized.

### 3.1.6 Our choice of methods to be applied to the experiemntal data

For the *discrete problem*, the best method this author has found so far is the iteration of all parameters. When dealing with a small number of components it does not exhibit any obvious disadvantages. Moreover, various software packages, e.g. MATLAB, Origin and SAS, have this functionality implemented. Finally, in real experiments we shall encounter systematic errors and therefore have need of the

non-optimal solutions.

For the *continuous problem*, NNLS has obvious advantages for our physical problem, since it yields non-negative solutions and allows regularization. As a result, it guarantees that the solutions are meaningful to some extent. We shall introduce some general theorems on the numerical instability on inverting the Laplace transform due to its eigenvalue spectrum.

From the expansion in this eigensystem, an exponential sampling method for inverting the Laplace transform was developed by McWhirter and Pike [33] in 1980, but was seldom mentioned in NMR literatures. Since it comes from the Sampling Theorem, it can be seen as an interpolation using sinc functions. We shall introduce it in Chapter 4. And we shall show a similar method in Chapter 4 that comes from an expansion in the eigenfunctions of the Laplace transform but solves the problem using arbitrary constituent functions. Although these two methods are for inverting the Laplace transform, they are different from the integral transform methods in Section 3.1.5, but are more similar to NNLS, in that all of them minimize an expression in the form

$$||f(t) - \sum_{n=1}^{N} c_n z_n(t)||_2, \tag{3.11}$$

where $z_n(t)$'s are known. Without any constraint on $c_n$'s, this problem can be solved by differentiating this minimizer with respect to $c_n$'s, and setting the derivatives to zero. Then $c_n$'s can be solved in the following way. Let $A$ be an $N$ by $N$ matrix, $\vec{b}$ be an $N$-vector, $N_t$ denote the number of time points, and the elements of $A$ and $b$ are defined to be

$$A_{mn} = \sum_{i=1}^{N_t} z_m(t_i) z_n(t_i) - \frac{1}{N_t} \sum_{i=1}^{N_t} z_m(t_i) \sum_{n=0}^{N_t-1} z_n(t_i), \tag{3.12}$$

$$b_m = \sum_{i=1}^{N_t} f(t_i) z_m(t_i) - \frac{1}{N_t} \sum_{i=0}^{N_t} f(t_i) \sum_{i=1}^{N_t} z_m(t_i). \tag{3.13}$$

The solution is

$$\vec{c} = A^{-1}\vec{b}, \tag{3.14}$$

$$C = \frac{1}{N_t}\sum_{i=1}^{N_t} f(t_i) - \sum_{i=1}^{N_t}\sum_{n=1}^{N} c_n z_n(t_i), \tag{3.15}$$

provided that $A^{-1}$ exists. Since $N$ is small, (3.14) can be done without any special algorithm.

## MATLAB algorithm 1

```
function [co,C,res]=lsqsum(B,f);
% Finding the solution minimizing 3.11
% B is matrix containing z(t)'s.
% The size of B is the number of time points by N.
% f is the signal. co is the array of coefficients.
% C is the baseline offset. res is the residual.
BB=B';
[M,N]=size(BB);
A=zeros(M,M);
k=length(f);
for i=1:M;
    for j=1:M;
        A(i,j)=sum(BB(i,:).*BB(j,:))-1/k*sum(BB(i,:))*sum(BB(j,:));
    end;
end;
b=zeros(M,1);
for i=1:M;
    b(i)=sum(f.*BB(i,:))-1/k*sum(f)*sum(BB(i,:));
end;
co=A\b;
f1=BB*co;
C=1/k*(sum(f)-sum(f1));
res=y-f1';
```

With NNLS, let $B$ be an $N_t$ by $N$ matrix, and

$$B_{ij} = z_j(t_i), \tag{3.16}$$

then the problem is inverting the system

$$\vec{f} \approx B\vec{c}. \tag{3.17}$$

NNLS will give nonnegative $\vec{c}$ to this problem. And as the number of unknowns is decreased, the problems of computing time and the possibility of failure can be resolved.

## 3.2 Numerical instability

### 3.2.1 The meaning of numerical instability in NMR data analysis

Consider the Fredholm integral equation of the first kind

$$f(t) = \int_{T_a}^{T_b} g(T)e^{-t/T}dT. \tag{3.18}$$

Solving such an inverse problem, i.e., finding $g(T)$ given $f(t)$, suffers from numerical instability. To be consistent with our physical problem, we will call $f(t)$ the signal, or the data, that is given by the solution, or the distribution $g(T)$.

Numerical instability means that a small change in the signal may cause a large change in the solution. The instability may come from the ill-posedness (Section 3.2.2) of the inverse problem. It may also come from the ill-conditioning in the subsets (of the set of all possible data) in which the solution is well-posed. The former source, i.e., the ill-posedness, makes larger differences in the solutions whose

signals are similar, and makes it generally impossible to charaterize the solutions that give similar signals. However, since the instability is what we can observe directly from data analysis, and it does not necessarily imply ill-posedness, we will only be concerned about numerical instability in general in this thesis. It is shown in Lanczos [25] that a sum of two exponentials may very well approximate a sum of three exponentials. Whittal and MacKay [48] also gave some examples of getting different solutions for a same data curve.

What is worse is that in NMR experiments for porous media, there is always noise, which one normally assumes, for simplicity, to be Gaussian white noise. This will be the assumption made in this thesis. As such, we also adopt the approach that "good" solutions to our inverse problem are those for which the residual, i.e., errors with respect to the signal data, exhibit the characteristics of Gaussian white noise. With a certain noise level, for example the noise level we encountered in our experiments, good solutions for a same data set can be very different from each other as a result of the numerical instability.

For example, in our experiments with the 30 MHz machine, the signal strength is about $f(0) \approx 10000$ (this is the magnitude shown by our computer, which has an arbitrary unit and is proportional to the total nuclear magnetization of the sample), and the noise level is about $\sigma[n(t)] \approx 25$ (Figure 3.4) in the same unit. Then if a distribution gives a signal that differs from the noiseless signal (the signal could have been given by the real distribution of the relaxation time if there is no noise) by less than 1 at every point, an intuitive judgment would tell us that it is a good solution, because this small difference plus the Gaussian white noise component still looks like a Gaussian white noise.

We now give an example in order to be strict in this argument. During data analysis, we will minimize the $L_2$ norm of the signal residual. In fact, because of the random nature of white noise, a deviation from the Gaussian white noise can have a smaller $L_2$ norm than the $L_2$ norm of the original noise. This means the true solution may not be the optimal solution.

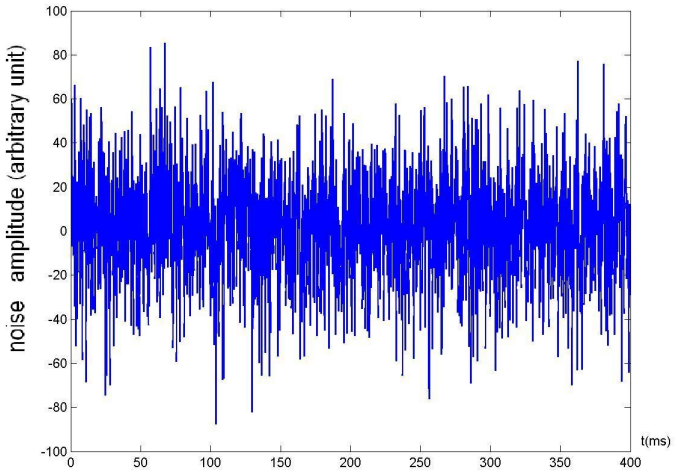


Figure 3.4: A Gaussian white noise with $\sigma[n(t)] = 25$ generated in MATLAB.

**Example 3.** ***The optimal solution not being the true distribution with presence of Gaussian white noise***

*In MATLAB we generated a phony data set with t=0,0.2,0.4...400, using the formula*

$$y = 5000e^{-t/30} + 5000e^{-t/50} + 5000e^{-t/90}.$$

*A Gaussian white noise was made by the command*

$$>> n = randn([1\ 2001]) * 25;$$

*and n(t) is shown in Figure 3.4. We then construct the noisy data set* $f(t) = y(t) + n(t)$. *The clean signal* $y(t)$ *and the noisy signal* $f(t)$ *are plotted in Figure 3.5. The* $L_2$ *norm of n(t), which is the residual between the data* $f(t)$ *and the noiseless signal, is 1126.8.*

*However, for this data, the parameter set in y(t) is not the optimal solution.*

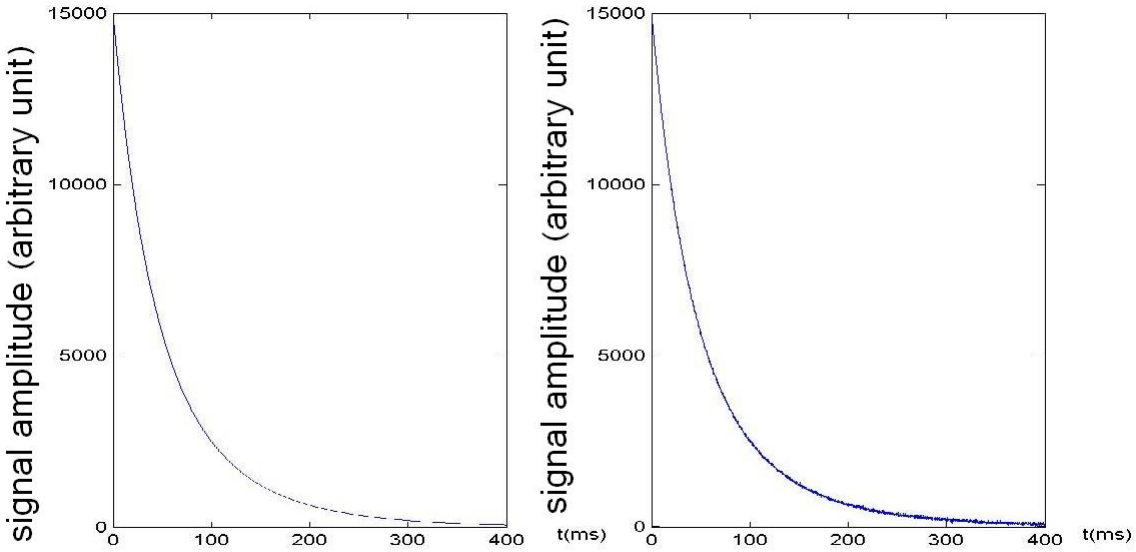


Figure 3.5: The clean signal $y = 5000e^{-t/30} + 5000e^{-t/50} + 5000e^{-t/90}$ (left) and the noisy signal $y + n$ (right) where $\sigma[n] = 25$.

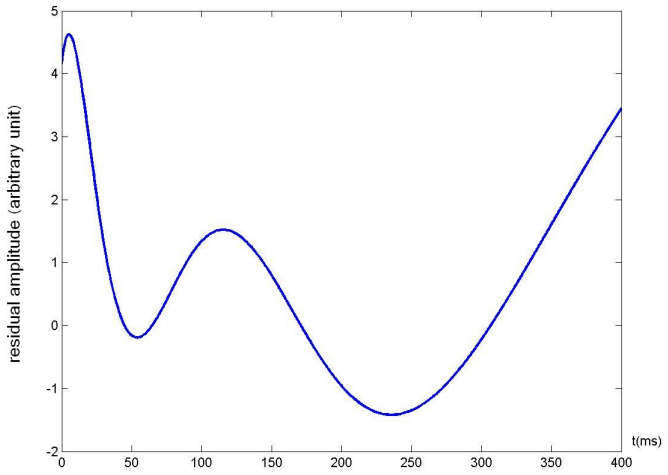


Figure 3.6: $\tilde{y}(t) - y(t)$

*Another solution*

$$\tilde{y}(t) = 4183.7e^{-t/89.98} + 4120.2e^{-t/62.11} + 6692.1e^{-t/31.99} + 8.1645; \tag{3.19}$$

*results in a residual, that is, $f(t) - \tilde{y}(t)$, with $L_2$ norm 1126.7. $\tilde{y}(t)$ is a "better" solution in terms of the $L_2$ norm of the residual, but its error in the second relaxation time is large.*

*Figure 3.6 plots the difference between $y(t)$ and $\tilde{y}(t)$. The maximal difference of these two functions is about 7. This gives us an example of how different signals are allowed to be when they are not distinguishable in the presence of noise.*

The above example shows that the optimal solution may not be the true parameters in term of $L_2$ norm of residual. Thus it is not so meaningful to demand the solution to be optimal, and getting "good" or "possible" solutions may be the best thing that we can do.

### 3.2.2 Ill-posedness of separation of exponentials

The problem of separation of exponentials is ill-posed, which means that it violates at least one of the following properties:

(1) A solution exists,

(2) The solution is unique,

(3) The solution depends continuously on the data, in some reasonable topology.

This follows the classic definition of "well-posedness" by the mathematician Hadamard [16]. For our problem, the violation of (2) and (3) occur at the same time. If the solution is unique for any possible data, then the solution will depend continuously on the data. But in fact, there can be several combinations of parameters that achieve the same level of approximation for one data set. And as the data changes, the optimal solution may jump from one region to another region in the solution space.

**Example 4.** ***Solution not depending continuously on the data***

*Consider a data set f(t) changing continuously from*

$$f_1(t) = 2e^{-t} + e^{-5t}$$

*to*

$$f_2(t) = 2e^{-4t} + e^{-t}$$

*by setting*

$$f(t) = \beta f_1(t) + (1 - \beta) f_2(t),$$

*where $\beta$ is varied from 1 to 0 continuously.*

*We fit $f(t)$ to a two-component exponential decay by fixing $A_1 = 2$ and $A_2$=1:*

$$f(t) \approx 2e^{-\lambda_1 t} + e^{-\lambda_2 t}.$$

*In the figures, we have plotted the the $L_2$ norm of the residual $f(t) - (2e^{-\lambda_1 t} + e^{-\lambda_2 t})$*

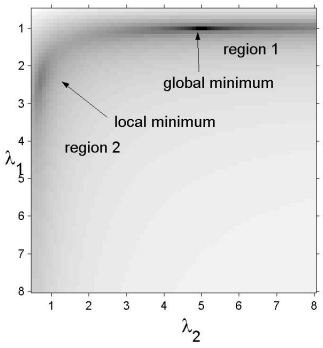


Figure 3.7: Gray level plots of the $L_2$ norm of the residual versus the two relaxation times. $\beta$=1.

*over the parameter region* $(\lambda_1, \lambda_2) \in [0.5, 8]^2$. *(This approach follows that of Greg Mayer in the Department of Applied Mathematics of the University of Waterloo, who used such figures to show the existence of multiple minima when minimizing the* $L_2$ *norm for an exponential decay fitting.)*

*We divide the domain of parameters* $(\lambda_1, \lambda_2)$ *into two regions, where Region 1 is defined by* $\lambda_1 < \lambda_2$ *and Region 2 is by* $\lambda_2 < \lambda_1$. *When* $\beta = 1$, *the global minimum of the norm of the residual is at (1,5), which is the true parameter set for the data. But there is another local minimum at about (2.2,0.8) (Figure 3.7). As* $\beta$ *decreases, the local minimum value of Region 1 increases while that of Region 2 decreases. When* $\beta = 0.4$, *the norms of the residuals at the two disconnected minima have about the same local minimum value (Figure 3.8). For* $\beta > 0.4$, *the local minimum in Region 2 becomes the global minimum (Figure 3.9). As a result, there is a discontinuous "jump" in the location of the global minimum from Region 1 to Region 2. A schematic illustration is shown in Figure 3.10.*

The ill-posedness is actually due to the fact that the data is allowed to be not in the form that is assumed for the solution. In the above example, we wanted

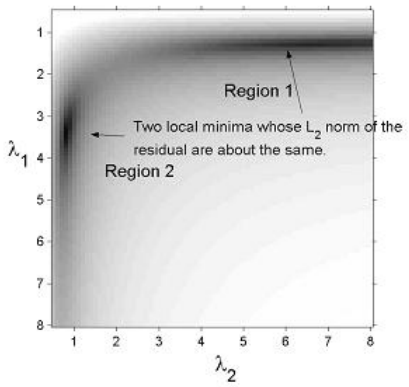


Figure 3.8: Gray level plots of the $L_2$ norm of the residual versus the two relaxation times. $\beta$=0.4.

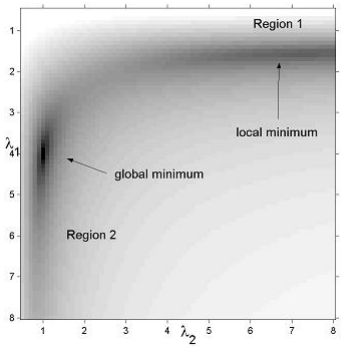


Figure 3.9: Gray level plots of the $L_2$ norm of the residual versus the two relaxation times. $\beta$=0.

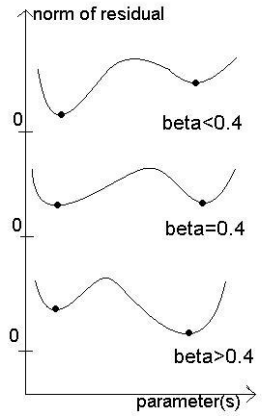


Figure 3.10: Schematic illustration for the ill-posedness shown in Example 4.

a solution being a sum of two exponentials. But as $f(t)$ changes from $f_1(t)$ to $f_2(t)$, $f(t)$ is never a sum of two exponentials except at the two ends. Figure 3.11 illustrates this procedure. On the figure, $D$ is the data set, $Y$ is the set of sums of two exponentials, and $X$ is the set of parameter sets. $f_\beta$ on the figure represents the data corresponding to $\beta = 0.4$ in the example. At this point, there are two different sums of two exponentials that best approximate the data, and each of them corresponds to a unique solution of the parameters. The continuous problem P4 suffers from the ill-posedness in the same way.

When there is noise, the data is never in $Y$. Every noisy data may be best approximated by many clean signals in $Y$, and each of them corresponds to a unique solution in $X$. Thus ill-posedness happens in the similar way as that in Figure 3.11.

### 3.2.3 Ill-conditioning and the eigensystem of the Laplace transform

In exactly solving $f(t) = S[g]$, i.e., when $f$ is only allowed to be in $Y$, the inverse problem on the positive axis, but still ill-conditioned. That is, a small change in $f$ (in some norm) can still cause a big change in $g$, although the change in $g$ can be

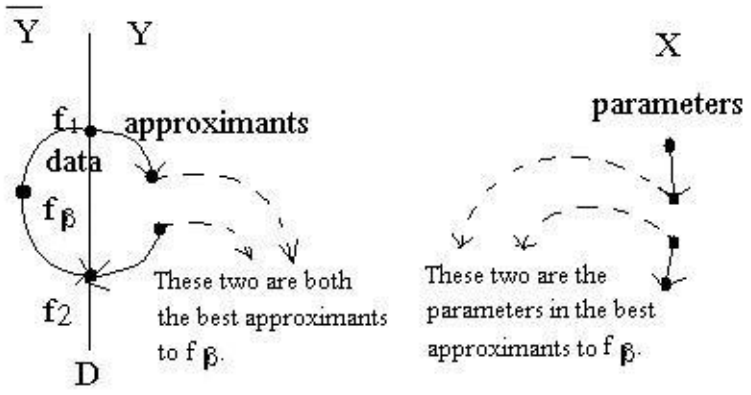


Figure 3.11: Another illustration for Example 4. $f_\beta$ represents the data when $\beta = 0.4$, and $f_1$ and $f_2$ are as defined in Example 4.

.

made arbitrarily small by restricting the change in $f$. This can be best illustrated by the eigensystem of Laplace transform.

By a change of variable $\lambda = \frac{1}{T}$, the integral equation (3.18) can be stated as a Laplace transform:

$$f(t) = \int_{\frac{1}{T_b}}^{\frac{1}{T_a}} \frac{g(\frac{1}{\lambda})}{\lambda^2} e^{-\lambda t} d\lambda. \tag{3.20}$$

It is shown in McWhirter and Pike [33] that the eigenfunctions of the Laplace transform are given by

$$\psi_\omega^+(v) = \frac{\Re(\sqrt{\Gamma(\frac{1}{2}+i\omega)}v^{-1/2-i\omega})}{\sqrt{\pi|\Gamma(\frac{1}{2}+i\omega)|}}, \tag{3.21}$$

$$\psi_\omega^-(v) = \frac{\Im(\sqrt{\Gamma(\frac{1}{2}+i\omega)}v^{-1/2-i\omega})}{\sqrt{\pi|\Gamma(\frac{1}{2}+i\omega)|}}, \tag{3.22}$$

where $v \in (0, +\infty)$ and $\omega \in \mathbb{R}$. Some of the eigenfunctions are plotted in Figure

3.12. These functions have the symmetry relationship

$$\psi_\omega^\pm = \pm\psi_{-\omega}^\pm. \tag{3.23}$$

In terms of real quantities, the eigenfunctions have the expressions

$$\psi_\omega^+(v) = \frac{1}{\sqrt{\pi}}[\cos(\theta/2)v^{-1/2}\cos(\omega\ln(v)) + \sin(\theta/2)v^{-1/2}\sin(\omega\ln(v))], \tag{3.24}$$

$$\psi_\omega^-(v) = \frac{1}{\sqrt{\pi}}[\sin(\theta/2)v^{-1/2}\cos(\omega\ln(v)) - \cos(\theta/2)v^{-1/2}\sin(\omega\ln(v))], \tag{3.25}$$

where

$$\theta = \arctan\left(\frac{\Re(\Gamma(\frac{1}{2}+i\omega)}{\Im(\Gamma(\frac{1}{2}+i\omega)}\right). \tag{3.26}$$

Note that $\psi_\omega^-(v) = 0$.

The corresponding eigenvalues are given by

$$\lambda_\omega^\pm = \pm\sqrt{|\Gamma(\frac{1}{2}+i\omega)|} = \pm\sqrt{\pi/\cosh(\pi\omega)}, \tag{3.27}$$

which are plotted in Figure 3.13, so that

$$\mathscr{L}[\psi_\omega^\pm(v)](t) = \lambda_\omega^\pm\psi_\omega^\pm(t). \tag{3.28}$$

The eigenfunctions are singular at $v = 0$ but are integrable. They are orthogonal so that

$$\int_0^{+\infty}\psi_\omega^+(v)\psi_{\omega'}^+(v)dv = \begin{cases}\delta(\omega-\omega') & \omega\neq 0,\\ 2\delta(\omega) & \omega = 0,\end{cases} \tag{3.29}$$

$$\int_0^{+\infty}\psi_\omega^-(v)\psi_{\omega'}^-(v)dv = \begin{cases}\delta(\omega-\omega') & \omega\neq 0,\\ 0 & \omega = 0,\end{cases} \tag{3.30}$$

$$\int_0^{+\infty}\psi_\omega^+(v)\psi_{\omega'}^-(v)dv = 0, \tag{3.31}$$

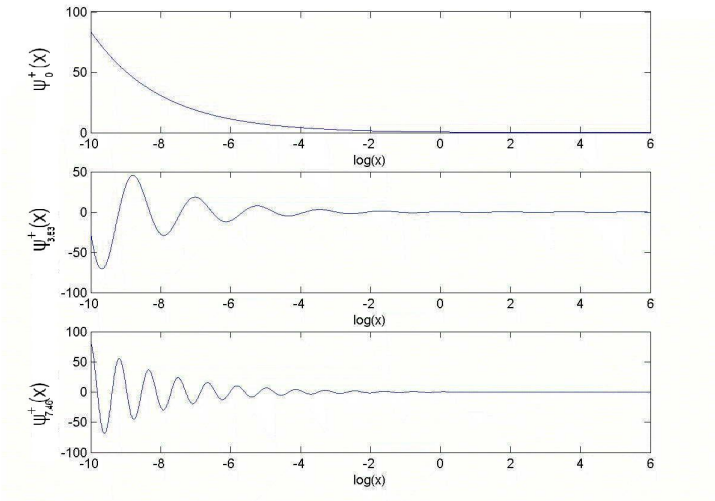


Figure 3.12: Some eigenfunctions of the Laplace transform for different values of $\omega$.

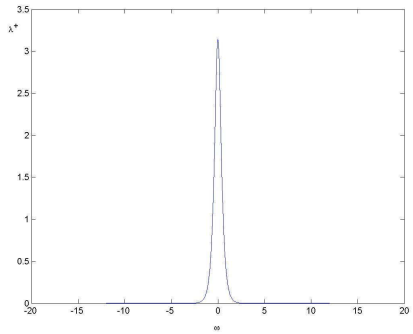


Figure 3.13: Eigenvalues decaying with $|\omega|$ increasing.

where $\delta$ is the Dirac delta function.

The set of eigenfunctions is also complete so such that for any $p(v) \in L^1(0, +\infty)$,

$$p(v) = \int_{-\infty}^{+\infty} c_\omega^+ \psi_\omega^+(v) d\omega + \int_{-\infty}^{+\infty} c_\omega^- \psi_\omega^-(v) d\omega. \tag{3.32}$$

Given $p(v)$, the coefficients $c_\omega$ can be found by

$$c_\omega^+ = \int_0^{+\infty} p(v)\psi_\omega^+(v)dv, \quad for\ \omega \neq 0, \tag{3.33}$$

$$c_0^+ = \frac{1}{2}\int_0^{+\infty} p(v)\psi_0(v)dv. \tag{3.34}$$

$$c_\omega^- = \int_0^{+\infty} p(v)\psi_\omega^-(v)dv, \quad for\ \omega \neq 0, \tag{3.35}$$

$$c_0^- = 0. \tag{3.36}$$

And so inverting the Laplace transform has a unique solution, provided that the integrals in calculating the coefficients converge.

Define

$$\Psi_\omega(v) = \psi_\omega^+(v) + i\psi_\omega^-(v) \tag{3.37}$$

$$= \frac{\sqrt{\Gamma(\frac{1}{2} + i\omega)}v^{-1/2-i\omega}}{\sqrt{\pi|\Gamma(\frac{1}{2} + i\omega)|}} \tag{3.38}$$

$$= \frac{v^{-1/2}e^{i\theta/2 - i\omega \ln v}}{\sqrt{\pi}} \tag{3.39}$$

$$= \frac{v^{-1/2}e^{i\theta/2}e^{-i\omega \ln v}}{\sqrt{\pi}}, \tag{3.40}$$

where $\theta$ is as defined in (3.26).

By a change of variable $x = \ln v$, $v^{1/2}p(v)$ can be expanded in terms of $e^{-i\omega \ln v}$,

that is,

$$v^{1/2}p(v) = \int_{-\infty}^{+\infty} \alpha_\omega e^{-i\omega \ln v} d\omega \tag{3.41}$$

$$= \int_{-\infty}^{+\infty} \beta_\omega \frac{e^{-i\omega \ln v} e^{i\theta/2}}{\sqrt{\pi}} d\omega \tag{3.42}$$

$$p(v) = \int_{-\infty}^{+\infty} \beta_\omega \Psi_\omega(v) d\omega, \tag{3.43}$$

where $\beta_\omega = e^{-i\theta/2}\alpha_\omega\sqrt{\pi}$ and $\theta$ is defined in (3.26).

Comparing (3.43) to the expression

$$p(v) = \int_{-\infty}^{+\infty} c_\omega^+ \Re(\Psi_\omega) d\omega + \int_{-\infty}^{+\infty} c_\omega^- \Im(\Psi_\omega) d\omega, \tag{3.44}$$

which is equivalent to (3.32), we have

$$\beta_\omega = c_\omega^+ - i c_\omega^- \tag{3.45}$$

and then $c_\omega^\pm$ can be obtained from $a_\omega$:

$$c_\omega^+ = \sqrt{\pi}\Re(e^{-i\theta/2}\alpha_\omega), \tag{3.46}$$

$$c_\omega^- = -\sqrt{\pi}\Im(e^{-i\theta/2}\alpha_\omega). \tag{3.47}$$

If $p(v)$ is defined on $[v_{min}, v_{max}]$, then $p(v)v^{1/2}$ can be expanded in the Fourier series (**??**) with discretized $\omega$

$$\Delta\omega = \omega_{n+1} - \omega_n = \frac{2\pi}{\ln v_{max} - \ln v_{min}}. \tag{3.48}$$

And so $\psi_\omega^\pm$ with the same discretization form a complete basis for $C[v_{min}, v_{max}]$. The

coefficients for the eigenfunctions after this discretization are

$$\tilde{c}_n^{\pm} = c_{\omega_n}^{\pm}/\Delta\omega. \tag{3.49}$$

Now let us see how this eigensystem accounts for the ill-conditioning of inverting the Laplace transform. The eigenvalues $\lambda_\omega$ are almost zero when $\omega$ is greater than 2. If a function cannot be approximately represented by its small-$\omega$ components only, its large-$\omega$ components cannot be ignored. However, in this case, the amplitudes of the large-$\omega$ components cannot be accurately solved if these components of the true distribution are not extremely large, because these components are too much diminished by the integral operator. This also means that the correct small-$\omega$ components plus an incorrect combination of the large-$\omega$ components may make a very good solution. This is the cause of the ill-conditioning in inverting the Laplace transform. Note that the ill-conditioning is intrinsic to the transform and thus not only encountered in the eigenfunction decomposition.

Functions that can be approximated by using only the small-$\omega$ components can be recovered by the eigenfunction method. In both [33] and our own numerical experiments, the function $\lambda e^{-\lambda}$ is recovered with a small error (compared to the recovered portion) from its Laplace transform. Unfortunately, in our problem the distributions are often thinner peaks. By "thin" we mean that the distribution has a small variance. For example it can be a peak on $T \in [50, 100]$, and then the domain of the preimage function in the corresponding Laplace transform is in $[0.01, 0.02]$. The large-$\omega$ components for such a preimage function are nonnegligible.

In the extreme case of a delta function, the Fourier spectrum has constant magnitude for all $\omega$. From (3.45), the magnitudes of the coefficients in the expansion using the eigenfunctions are also constant. The contribution of each component in the Laplace transform decays as the coefficients in the expansion of $p(v)$ times $\lambda$, which is, after all, $\lambda_\omega$. By numerically integrating $|\lambda_\omega|$ over $\omega$, we can see that the finite integral for $|\omega| \leq 4.5$ contributes to more than 99.9% of the whole infinite

integral. If we employ the cutoff

$$|\omega| \leq \omega_{max} = 4.5, \tag{3.50}$$

the time domain signal would have little difference but the distribution would certainly be very different from a delta function.

## 3.3 Time-scaling property

The integral equation (3.18) has a nice time-scaling property. By a change of variable $\tilde{T} = kT$ and $\tilde{t} = kt$, and let $\tilde{f}(\tilde{t}) = f(\tilde{t}/k)$, (3.18) becomes

$$f(t) = \tilde{f}(\tilde{t}) = \int_{kT_a}^{kT_b} \frac{g(\tilde{T}/k)}{k} e^{-\tilde{t}/\tilde{T}} d\tilde{T}, \tag{3.51}$$

$$\int_{kT_a}^{kT_b} \frac{g(\tilde{T}/k)}{k} d\tilde{T} = \int_{T_a}^{T_b} g(T) dT.$$

Suppose we are looking for a solution for the data $\tilde{f}(\tilde{t})$ and $\tilde{T} \in [kT_a, kT_b]$, solving the equivalent problem for this data with the scaled time $t = \tilde{t}/k$ and $T \in [T_a, T_b]$ will give the solution for $\tilde{T} \in [kT_a, kT_b]$ with the original $t$ axis. Then any property of the problem for $[T_a, T_b]$ can be adopted to the interval $[kT_a, kT_b]$.

This implies that the resolution of the problem worsens logarithmically with $T$, which in fact can be seen from the eigenfunctions of the Laplace transform. In many papers (for example [48]), the distribution is represented on a $\log(T)$ scale instead of $T$ scale.

# Chapter 4

# Using Continuous Constituent Functions for the Approximate Inversion of Laplace Transforms and Solving Similar Integral Equations

In Section 3.1.4, we introduced the method that solves the integral equation (3.18) by solving a linear system. The number of columns of the matrix is the number of unknowns, i.e., the number of discrete $T_k$ points. If we can reduce the number of unknowns, then the solution should require less time. In addition, failures of the algorithm would not easy to happen. Such a reduction may be achieved by assuming a set of continuous constituent functions, and solving for their associated expansion coefficients instead of the coefficients at all $T_k$ points.

The reduction of the number of unknowns essentially relies on the ill-conditioning of the integral transform. Introducing constituent functions is like grouping preimage

functions of the integral transform that yield similar images.

The constituent functions can be sinc functions as a result of a series expansion of the solution and the Sampling Theorem. This way of solving a Fredholm integral equation of the first kind was shown in [34] for one specific kernel and the expansion in the eigenfunctions of this kernel. In the next section, following their procedure, we will formulate the general procedure of solving an arbitrary Fredholm integral equation of the first kind by an Fourier-like expansion and by means of the Sampling Theorem. And then we will develop a new method of using arbitrary constituent functions which also results from the series expansion of the solution.

## 4.1 Reducing the number of unknowns by expansion

### 4.1.1 General formulation of expanding the preimage function

Consider the Fredholm integral equation of the first kind

$$f(t) = \int_0^{+\infty} p(v)K(v,t)dv, \tag{4.1}$$

which we solve for $p(v)$ from $f(t)$.

We suppose that $p(v)$ can be expanded in terms of a continuously-indexed family of functions $\phi_\omega$ as follows,

$$p(v) = \int_{-\infty}^{+\infty} c_\omega \phi_\omega d\omega, \tag{4.2}$$

so that

$$f(t) = \int_{-\infty}^{+\infty} c_\omega \int_0^{+\infty} \phi_\omega(v)K(v,t)dvd\omega. \tag{4.3}$$

For example this expansion can be the Fourier transform.

If for this set of $\phi_\omega$, there exists an $\omega_{max}$ such that the quantity

$$\int_{-\infty}^{-\omega_{max}} c_\omega \int_0^{+\infty} \phi_\omega(v)K(v,t)dvd\omega + \int_{\omega_{max}}^{+\infty} c_\omega \int_0^{+\infty} \phi_\omega(v)K(v,t)dvd\omega \tag{4.4}$$

is negligible, then

$$\tilde{p}(v) = \int_{-\omega_{max}}^{+\omega_{max}} c_\omega \phi_\omega(v)d\omega \tag{4.5}$$

is an approximate solution to (4.1).

**Use of the Sampling Theorem assuming continuous spectrum**

With the assumption of the cutoff in $\omega$, let us assume that the $\phi_\omega$ are of the form

$$\phi_\omega(v) = q(v)r_\omega e^{ih(v)\omega}, \tag{4.6}$$

where $r_\omega$ is any function of $\omega$, and $h(v)$ is absolutely monotone, as is the case for the set of eigenfunctions of the Laplace transform. Then, make the change of variable $x = h(v)$ and define

$$P(x) = \frac{\tilde{p}(v)}{h'(v)} \tag{4.7}$$

(this latter change of variable is to make the integration of a sinc function easier later), so that

$$P(x)dx = \tilde{p}(v)dv. \tag{4.8}$$

From Eq. (4.5) it follows that

$$\frac{\tilde{p}(v)}{q(v)} = \frac{h'(h^{-1}(x))P(x)}{q(h^{-1}(x))} = \int_{-\omega_{max}}^{+\omega_{max}} c_\omega r_\omega e^{ix\omega}d\omega. \tag{4.9}$$

The integral on the right hand side may be viewed as the inverse Fourier transform over a finite frequency interval, implying that the function $\tilde{p}(v)/q(v)$ is "band limited". By the Sampling Theorem [32], $\tilde{p}(v)/q(v)$ can be recovered from its sampled

points at $v_n$ where $x_{n+1} - x_n = h(v_{n+1}) - h(v_n) = \pi/\omega_{max}$ on the positive half axis. This, in turn, implies that $P(x)$ can be reconstructed from these sampled values by

$$P(x) = \frac{q(h^{-1}(x))}{h'(h^{-1}(x))} \sum_{n=1}^{\infty} \frac{P(x_n)}{q(v_n)} \text{sinc}(\omega_{max}(x - x_n)). \tag{4.10}$$

We may now use (4.10) and (4.3) to produce the following approximation $\tilde{f}(t)$ to $f(t)$ in Eq. (4.1):

$$\begin{aligned}
\tilde{f}(t) &= \int_0^{\infty} \tilde{p}(v) K(v,t) dv && (4.11)\\
&= \int_{h^{-1}(0)}^{h^{-1}(\infty)} K(v(x),t) P(x) dx \quad (by\ (4.8)) && (4.12)\\
&= \sum_{n=1}^{\infty} \frac{\tilde{p}(v_n)}{q(v_n)} h'(v_n) \int_{-\infty}^{\infty} K(v(x),t) \frac{q(v(x))}{h'(v(x))} \text{sinc}(\omega_{max}(x - x_n)) dx && (4.13)\\
&= \sum_{n=1}^{\infty} P(x_n) \int_{-\infty}^{\infty} K(v,t) \frac{q(v(x))h'(v(x_n))}{q(v(x_n))h'(v(x))} \text{sinc}(\omega_{max}(x - x_n)) dx. && (4.14)
\end{aligned}$$

Now define

$$W_n(t) = \int_0^{\infty} K(v,t) \frac{q(v(x))h'(v(x_n))}{q(v(x_n))h'(v(x))} \text{sinc}(\omega_{max}(x - x_n)) dx. \tag{4.15}$$

Since

$$\lim_{\omega_{max} \to \infty} \text{sinc}(\omega_{max}(x - x_n)) = \frac{\pi}{\omega_{max}} \delta(x_n), \tag{4.16}$$

it follows that

$$\lim_{\omega_{max} \to \infty} W_n(t) = \frac{\pi}{\omega_{max}} K(x_n, t). \tag{4.17}$$

Therefore, we can solve the integral equation (3.1) by minimizing

$$||f(t) - \tilde{f}(t)||_2 = ||f(t) - \sum_{n=1}^{N} P(x_n) W_n(t)||_2. \tag{4.18}$$

With noise $n(t)$ and baseline offset $C$, the minimizer is

$$||f(t) - \tilde{f}(t)||_2 = ||f(t) - \sum_{n=1}^{N} P(x_n)W_n(t) - C||_2. \tag{4.19}$$

$N$ is chosen so that the function is sampled on a suitably large interval. Minimizing (4.19) is accomplished by solving an $N$ by $N$ linear system after differentiating the minimizer with respect to $P(x_n)$ and setting the derivatives equal to zero, as done in (3.12)-(3.15). And then $P(x)$ is found using (4.10) and $\tilde{p}(v)$ is found using (4.7).

### Discrete spectrum

If the $\omega$ index is discretized, and a suitable cutoff value still exists, then a solution can be found by minimizing the residual

$$||f(t) - \sum_{n=-n_{max}}^{n_{max}} c_{\omega_n} \int_0^{+\infty} \phi_{\omega_n}(v)K(v,t)dv - C||_2. \tag{4.20}$$

Recall that a finite interval can be spanned by Fourier series with discrete $\omega$ values. If $\phi_\omega$ is of form (4.6), then discrete $\omega$ implies that the solutions are defined on finite intervals. The smaller the interval of $v$, the larger is the minimum $\Delta\omega$ required. However for the inverse problem, if we know that the solution is supported on a small interval, we cannot just discretize $\omega$ over this interval for the following reason. Although the expansion with continuous spectrum sums to the solution exactly, which is zero outside a small interval, the expansion with the discrete spectrum may not sum to zero outside the assumed interval. Therefore, the transformed expansion with discrete spectrum by infinite integral is not the same as the transformed solution, who is zero outside a small interval.

If, however, the integral in Eq. (3.1) is over a finite interval, and the cutoff

frequency is found according to the error

$$\int_{-\infty}^{-\omega_{max}} c_\omega \int_{v_{min}}^{v_{max}} \phi_\omega(v)K(v,t)dvd\omega + \int_{\omega_{max}}^{+\infty} c_\omega \int_{v_{min}}^{v_{max}} \phi_\omega(v)K(v,t)dvd\omega, \quad (4.21)$$

which assumes the small interval, then we could discretize $\omega$ according to the small interval as well.

But to find a suitable cutoff using a finite integral in (3.1) may not be as easy as to find this cutoff value using the infinite integral. So we do not find the frequency cutoff value according to the finite integral. If (4.21) is almost the same as (4.4) (which does the infinite integrals), then the discretization of $\omega$ according to $[v_{min}, v_{max}]$ the $\omega_{max}$ assuming the infinite integral are both valid. For example, for the eigenfunctions of the Laplace transform, following the approach in [**?**], if $v_{min} = 10^{-6}$ and $v_{max} = 100$,

$$\int_0^{v_{min}} e^{-vt}\psi_\omega^{\pm}(v)dv \leq \frac{1}{\sqrt{\pi}} \int_0^{v_{min}} v^{-1/2}dv \sim {v_{min}}^{1/2} = 10^{-3}, \quad (4.22)$$

In our experimental data, the spacing of $t$ points is about 0.2, and the first point ($t = 0$) can be ignored when the fitting error at the first point is much greater than the rest. With the inequality $e^{-0.2v} < v^{-3}$ for $v > 100$, we have

$$\int_{v_{max}}^{\infty} e^{-vt}\psi_\omega^{\pm}(v)dv \leq \frac{1}{\sqrt{\pi}} \int_{v_{max}}^{\infty} v^{-7/2}dv \sim {v_{max}}^{-5/2} = 10^{-5}. \quad (4.23)$$

Then we can say that when $p(v)$ is expanded in the eigenfunctions which are set to be zero outside $[v_{min}, v_{max}]$, the contributions from each component still decay as before, and the cutoff error (4.21) is almost the same with (4.4). Therefore, $\omega$ can be discretized as follows

$$\Delta\omega = \frac{2\pi}{\ln 100 - \ln 10^{-6}} \approx 0.34, \quad (4.24)$$

and the $\omega_{max}$ that we found before discretizing the spectrum is still valid.

Theoretically, the solution can then be found by solving the coefficients in (4.20)

directly. But when we really want a solution localized on a small solution for the separation of relaxation times problem, this method will not work, because the $p(v)$ is assumed to be on $[10^{-6}, 100]$, and the solution can be much wider than the physically allowed interval of $v$. We would like to find solutions on intervals smaller than $[10^{-6}, 100]$ if possible.

**Finding solutions using arbitrary constituent functions**

Now assume a Fourier-like series $\phi_n$ in the form (4.6). Also assume that a true distribution $p(v)$ and a set of arbitrary nonzero integrable functions $\{\eta_i(v)\}_{i=1}^N$ are all feasible for the frequency cutoff at $\omega_{max}$. Finally, let $[v_{min}, v_{max}]$ be a sufficiently large interval $[v_{min}, v_{max}]$, so that the $\omega_{max}$ is still valid after discretization of $\omega$. Then

$$\Delta\omega = \frac{2\pi}{h(v_{max}) - h(v_{min})}, \tag{4.25}$$

and the number of functions that we need for the expansions, denoted by $N$, can be found accordingly. By the frequency property of $p(v)$ and $\eta_i$,

$$\tilde{p}(v) = \sum_{n=1}^{N} c_n \phi_n(v) \tag{4.26}$$

and

$$\tilde{\eta}_i(v) = \sum_{n=1}^{N} b_{in} \phi_n(v). \tag{4.27}$$

Let

$$q(v) = \sum_{i=1}^{N} a_i \eta_i(v) \tag{4.28}$$

$$= \sum_{n=1}^{N} \sum_{i=1}^{N} a_i b_{in} \phi_n(v), \tag{4.29}$$

then $\int_{v_{min}}^{v_{max}} p(v)K(v,t)dv \approx \int_{v_{min}}^{v_{max}} q(v)K(v,t)dv$ if

$$\sum_{n,i=1}^{N} a_i b_{in} \phi_n(v) = \sum_{n=1}^{N} c_n \phi_n(v), \tag{4.30}$$

which is obviously true when

$$\sum_{i=1}^{N} a_i b_{in} = c_n \tag{4.31}$$

for every $n$. Let $Q$ be an $N$ by $N$ matrix such that

$$Q_{ni} = b_{in}, \tag{4.32}$$

then $\vec{a}$ is uniquely determined from $\vec{c}$ by

$$\vec{a} = Q^{-1}\vec{c}, \tag{4.33}$$

provided that $Q^{-1}$ exists.

The existence of $Q^{-1}$ generally requires that the $\vec{b}_i$ vectors are linearly independent. With the $\phi_n(v)$ linearly independent, it means that $\tilde{\eta}_i(v)$ are linearly independent, or the integral transforms of $\tilde{\eta}_i(v)$ are linearly independent, which is likely to be satisfied when $\eta_i(v)$ are linearly independent.

Then we can conclude that when we have a suitable $N$ for the frequency cutoff and discretization, we can assume $N$ arbitrary linearly independent constituent functions that are feasible to this frequency cutoff and discretization on our assumed interval, and there is very likely to exist a linearly combination of these functions that is an approximate solution to the integral equation.

The solution is found by minimizing

$$||f(t) - \sum_{n=1}^{N} c_n \int_{v_{min}}^{v_{max}} \eta_n(v)K(v,t)dv - C||_2, \tag{4.34}$$

where $C$ is a baseline offset, and will result in solving an $N$ by $N$ linear system as done in (3.12)-(3.15).

The use of arbitrary constituent functions can also be formulated by expanding the kernel. For the same integral equation (4.1), if the kernel can be expanded as

$$K(v,t) = \sum_{n=1}^{+\infty} r_n(v)\phi_n(t), \tag{4.35}$$

then

$$f(t) = \sum_{n=1}^{+\infty} \phi_n(t) \int_0^{+\infty} g(v)c_n(v)dv. \tag{4.36}$$

If there exists an $N$ such that for any $p(v)$, the error in the cutoff in $n$, which is

$$\sum_{n=N+1}^{+\infty} \phi_n(t) \int_0^{+\infty} p(v)r_n(v)dv, \tag{4.37}$$

is negligible, then $q(v)$ is an approximate solution to (4.1), if

$$\sum_{n=1}^{N} \phi_n(t) \int_0^{+\infty} r_n(v)p(v)dv = \sum_{n=1}^{N} \phi_n(t) \int_0^{+\infty} r_n(v)q(v)dv. \tag{4.38}$$

This is obviously true if

$$\int_0^{+\infty} r_n(v)p(v)dv = \int_0^{+\infty} r_n(v)q(v)dv \tag{4.39}$$

for all $n = 1, 2..N$. Let

$$\tilde{p}(v) = \sum_{n=1}^{N} c_n\eta_n(v), \tag{4.40}$$

$$a_n = \int_0^{+\infty} r_n(v)p(v)dv, \tag{4.41}$$

and $Q$ be an $N$ by $N$ matrix with

$$Q_{ij} = \int_0^{+\infty} r_i(v)\eta_j(v)dv. \tag{4.42}$$

Then $c_n$ in (4.40) is uniquely determined from $a_n$ in (4.41) by

$$\vec{c} = Q^{-1}\vec{a} \tag{4.43}$$

provided that $Q^{-1}$ exists. The existence of $Q^{-1}$ generally requires that $\eta_n(v)$'s are linearly independent and that none of them are orthogonal to any one of the $r_n(v)$.

As an example, the kernel can be expanded in its Taylor series about some $v_0$, and then $\phi_n(t)$ are $e^{-v_0 t}$ multiplied by polynomials of $t$. Compared to the formulation of expanding the preimage function, expanding the kernel does not require that $p(v)$ satisfies the frequency cutoff. But to find $N$ from (4.37) without expanding $p(v)$ will need to take $\phi_n(v)$ out of the integral in (4.37) by relaxing it to its maximum absolute value on $[v_{min}, v_{amx}]$. This will result in a much larger $N$ than required for an expansion of $p(v)$.

### 4.1.2 Inverting the Laplace transform by exponential sampling

We now invert the Laplace transform from discrete data by expanding the preimage function and using sampling theorem based on the formulations in Section 4.2.1.

The minimizer will be

$$||f(t) - \sum_{n=1}^{N} P(x_n)W_n(t)||_2, \tag{4.44}$$

where

$$P(x) = e^x\tilde{p}(e^x) = v\tilde{p}(v) \tag{4.45}$$

and

$$W_n(t) = \int_0^\infty e^{-e^x t} e^{(x-x_n)/2} \text{sinc}(\omega_{max}(x - x_n))dx, \tag{4.46}$$

which approaches $\pi/\omega_{max} e^{-e^{x_n} t}$ as $\omega_{max} \to \infty$. So if $\omega_{max}$ is large, we can instead solve for the optimal $v_n \tilde{p}$ in

$$||f(t) - \sum_{n=1}^{N} \pi/\omega_{max} v_n \tilde{p}(v_n) e^{-v_n t}||_2, \tag{4.47}$$

and $\tilde{p}(v)$ will be a sum of $N$ delta functions. With use of $W_n$, $\tilde{p}(v)$ is recovered by

$$\tilde{p}(v) = v^{-1/2} \sum_{n=1}^{N} v_n^{1/2} \tilde{p}(v_n) \text{sinc}(\omega_{max}(\ln v - \ln v_n)). \tag{4.48}$$

The solution is the optimal solution assuming the cutoff of frequency and interval for $v$.

In our practical problem of separation of relaxation times, the interval of $v$ is extremely small, i.e., $[0.01, 0.1]$. If $\omega_{max} = 2\pi$, we assume that the re-constructed solution will still be zero outside this interval, so that $N = 6 \approx 2(\ln 0.1 - \ln 0.01) + 1$.

For the relaxation times problem, $g(T) = p(1/T)/T^2$, and so $g$ can be reconstructed directly by

$$g(T) = T^{-5/2} \sum_{n=1}^{N} v_n^{-1/2} P(x_n) \text{sinc}(\omega_{max}(-\ln T - \ln v_n)). \tag{4.49}$$

Although the change of variable is not linear, $g$ can still be recovered on equipartitioned $T$ values.

## MATLAB algorithm 2

```
function [g,C,res]=gsampling(x,xx,t,T,f);
% the sampling method
```

```
% x is as defined in Section 4.1.2 and xx is the sampling points of x
% t is the time axis
% T is the array of relaxation time points
% f is the signal
% g is the reconstructed solution on T
% C is the baseline offset
% res is the residal.
% omega cutoff is 2pi.
n=length(x);
W=zeros(length(t),n);
v=exp(x);
for i=1:n;
    W(:,i)=transpose(laptr((xx),sinc(2*(xx-x(i))).*exp(1/2*(xx-x(i))),t));
end;
[co,C,res]=lsqsum(W,f);
% lsqsum is the function in Algorithm 1 in Section 3.1.6
g=T*0;
for i=1:n;
    g=g+co(i)/power(v(i),0.5).*sinc(2*(-log(T)-log(v(i))));
end;
g=g.*power(T,-2.5);


function y=laptr(x,p,t);
% finding the laplace transform of p by simpson's rule
% x is the axis as defined in Section 4.1.2
% t is the time axis
y=t*0;
dx=x(2)-x(1);
odd=(3:2:length(x)-1);
even=(2:2:length(x)-1);
for i=1:length(t);
    es=p.*exp(-exp(x)*t(i)).*exp(x);
    y(i)=(sum(es(even))*4+sum(es(odd))*2+es(1)+es(length(x)))*dx/3;
end;
```

**Example 5.** ***Using the sampling method to find an arbitrary distribution of relaxation times***

*Consider the following distribution of $T$ used in Example 1 of Section 3.1.4,*

$$g(T) = A(e^{-(T-30)^2/100} + e^{-(T-50)^2/100} + e^{-(T-80)^2/100})(45^2 - (T-55)^2), \qquad (4.50)$$

*for $T \in [10, 100]$ (ms) and $A$ is a scaling factor so that $S[g](0) = 10000$. In addition, we add a white Gaussian noise $n(t)$ generated by Matlab with standard deviation 25 and a baseline offset $C = -2000$. We then construct the data according to the formula $f(t) = S[g] + n(t) + C$ for $t = 0, 0.2, 0.4...400$ (ms).*

*We use $\omega_{max} = 2\pi,\ 4\pi$ and $x \in [-4.6254, -2.1254]$ where $x$ is equipartitioned with spacing 0.0005. And then $v \in [-0.0098, 0.1069]$ and $T \in [8.38, 102.04]$. When $\omega_{max} = 2\pi$, there are 6 sampled points and $x_{n+1} - x_n = 0.5$. When $\omega_{max} = 4\pi$, there are 11 sampled points. We find $P(x_n)$ from (4.44) and reconstruct $g$ from (4.49). Figure 4.1 shows the true $g$ and the two solutions using the two $\omega_{max}$. Figure 4.2 plots the residuals between the fitted data and the clean data $S[g] + C$.*

*The data points are very well fitted despite the large noise component, however the solutions oscillate and assume negative values which is physically inadmissable. When $\omega_{max}$ is large, the oscillation is too severe.*

**Example 6.** ***Use of sampling method when the true solution is composed of a few delta functions***

*Consider the distribution*

$$g(T) = 3000\delta(T-20) + 3000\delta(T-50) + 3000\delta(T-90), \qquad (4.51)$$

*for $T \in [10, 100]$ (ms). Here, $n(t)$ is a Gaussian white noise with standard deviation 25 and $C = -2000$. The data is then assumed to be given by $f(t) = S[g] + n(t) + C$. The solution with $\omega_{max} = 2\pi$ and the true distribution are plotted in Figure 4.3. For this example, we use the interval $x \in [-4.6254, -2.6254]$ instead of $x \in$*

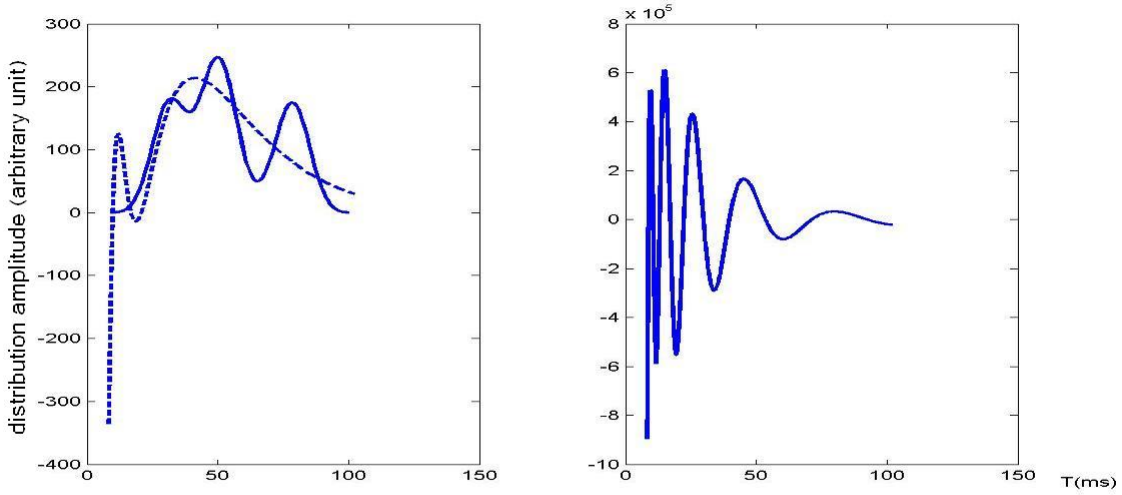


Figure 4.1: Solution by the sampling method. The left figure plots the true $g$ (solid line) and the solution with $\omega_{max} = 2\pi$ (dashed line). The right figure plots the solution with $\omega_{max} = 4\pi$.

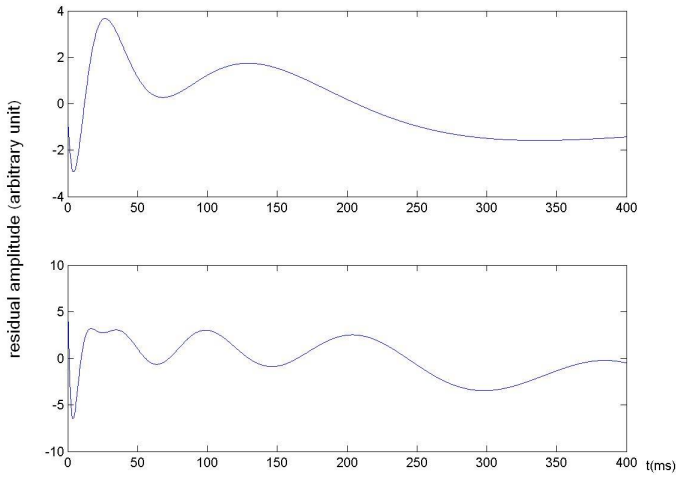


Figure 4.2: The fitting residuals with $\omega_{max} = 2\pi$ and $\omega_{max} = 4\pi$.

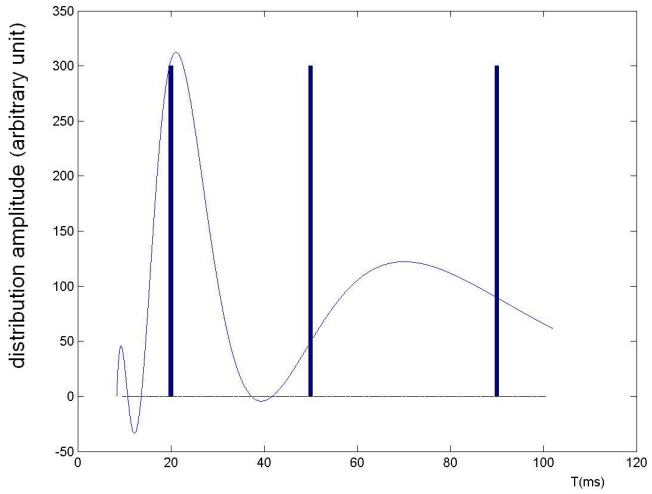


Figure 4.3: Solution found by the sampling method (line) when the true distribution is composed of three delta functions (bars). The bars are scaled by being divided by 10.

$[-4.6254, -2.1254]$ *as in the last example. When we use the latter interval, the sampled value at* $-2.1254$ *has a large negative value. As a result, we simply dropped that point, since the remained interval is still large enough to support the true* $g(T)$*.*

*It is seen in the figure that the solution given by the sampling method has a peak at 20, but the latter two delta functions are represented by one wide peak of low magnitude. This is understandable since the resolution of the sampling method decreases logarithmically and the resolving capacity on* $[10, 40]$ *is the same with that on* $[30, 120]$*.*

### 4.1.3 Inverting the Laplace transform using arbitrary constituent functions

Now we apply the method of arbitrary constituent functions in Section 4.1.1 to invert the Laplace transform. All expansions are performed in terms of the eigenfunctions of the Laplace transform.

We use the discretization (4.24) and the frequency cutoff (3.50) so that $\Delta\omega = 0.34$ and $\omega_{max} = 4.5$. Then $N = 14$.

This method is very flexible not only because that the constituent functions are arbitrary, but also because that it is not affected by change of variables. If $N$ constituent functions of $v$ can invert the Laplace transform, then $N$ constituent functions of $T$ can solve the relaxation time distribution, and any variable can be equipartitioned.

$N = 14$ is for any $p(v)$ for $v \in [10^{-6}, 100]$. Even if for our problem $v \in [0.01, 0.1]$, theoretically we still need this many constituent functions. However, this number is an upper bound. It does not mean that a smaller $N$ will not give a good solution.

In MATLAB, the NNLS scheme does not have regularization options. We will use an approximation for regularizing the first derivative: extend the matrix $B$ in 3.16 to $\tilde{B}$ such that

$$\tilde{B} = \begin{pmatrix} B \\ kI \end{pmatrix}, \tag{4.52}$$

where $I$ is the $N$ by $N$ identity matrix and $k$ is a weighting constant, and then concatenate $N$ zeros to the $f$ vector. In this way the minimizer becomes

$$||f(t) - \sum_{n=1}^{N} c_n z_n(t)||_2 + k||\vec{c}||_2. \tag{4.53}$$

In fact the way to extend $B$ can be made to realize the ordinary definition of regularizing the first derivative, which is to replace the $c_n^2$ term by a $(c_n - c_{n+1})^2$ term

for every $n$ in the minimizer, by adding a "$-1$" at positions $(n, n+1)$ in the identity matrix in (4.52). But in our experiments in MATLAB, LSQNONNEG gives SVD error for this extension. So we will use the above approximation.

## MATLAB algorithm 3

```
function [co,C,res]=lsqconsti(funcs,T,t,f);
% solving the coefficients of constituent functions
% for relaxation time distribution
% funcs contains the constituent functions. The number of rows
% of funcs is the number of constituent functions. And the number
% of columns of funcs is the number of T points
% T is the relaxation time axis
% f is the signal f(t)
% co is the vector of the coefficients of the constituent functions
% C is the baseline offset
% res is the residual
[M N]=size(funcs);
k=length(f);
yy=zeros(M,k);
for i=1:M;
    for j=1:length(t);
        yy(i,:)=yy(i,:)+funcs(i,:)*exp(-x/T(i));
    end;
end;
[co,C,res]=lsqsum(yy,f);
% lsqsum is the function in Algorithm 1 in Section 3.1.6
```

**Example 7.** ***Constructing approximate solutions from arbitrary constituent functions without regularization***

*Consider the same data set as in Example 5. We now attempt to solve for $g(T)$ in Eq. (4.52) by the procedure in Eqs. (3.12)-(3.15). Three sets of constituent functions will be considered for illustration.*

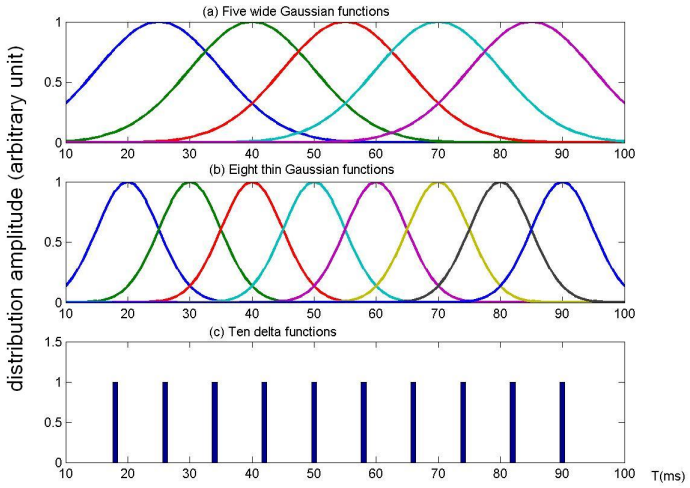


Figure 4.4: The three sets of constituent functions used in Example 7 as examples of using arbitrary constituent functions.

*(a) Five wide Gaussian functions:*

$$\phi_i(T) = e^{-(T-10-15i)^2/200}, T = 10, 11, ...100, i = 1..5.$$

*(b) Eight thinner Gaussian functions:*

$$\phi_i(T) = e^{-(T-10-10i)^2/50}, T = 10..100, i = 1..8.$$

*(c) Ten delta functions:*

$$\phi_i(T) = \delta(T + 10 + 8i), T = 10..100, i = 1..10.$$

*These constituent functions are plotted in Figure 4.4. The solutions are plotted in Figure 4.5 and the residuals are plotted in Figure 4.6. From the latter, we note that the data points are well fitted but the solutions cannot be constrained to be non-negative.*

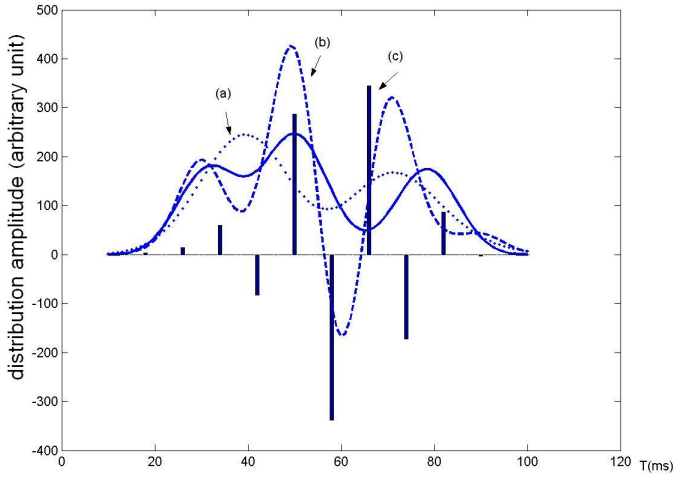


Figure 4.5: Results of Example 7. The solid line is the true $g(T)$ as defined in (4.50), the dotted line is the solution using the constituent functions set (a), the dashed line is the solution using (b), and the bars are solved using (c). The results of the bars were divided by 50 for the purpose of scaling.

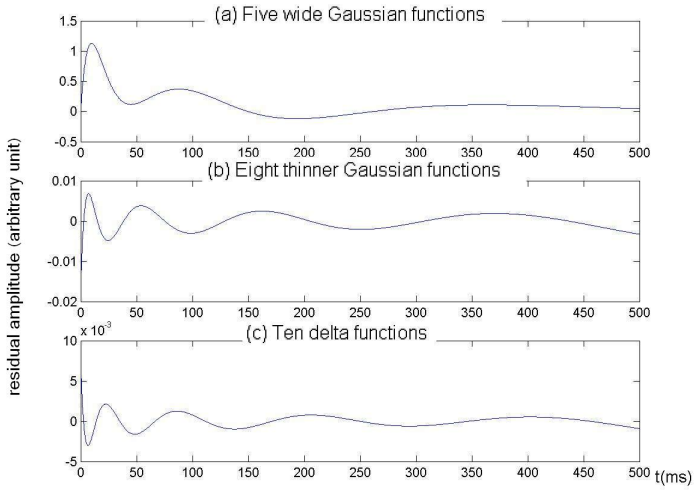


Figure 4.6: The residuals, that is, $f - S[g]$, for the three solved $g(T)$.

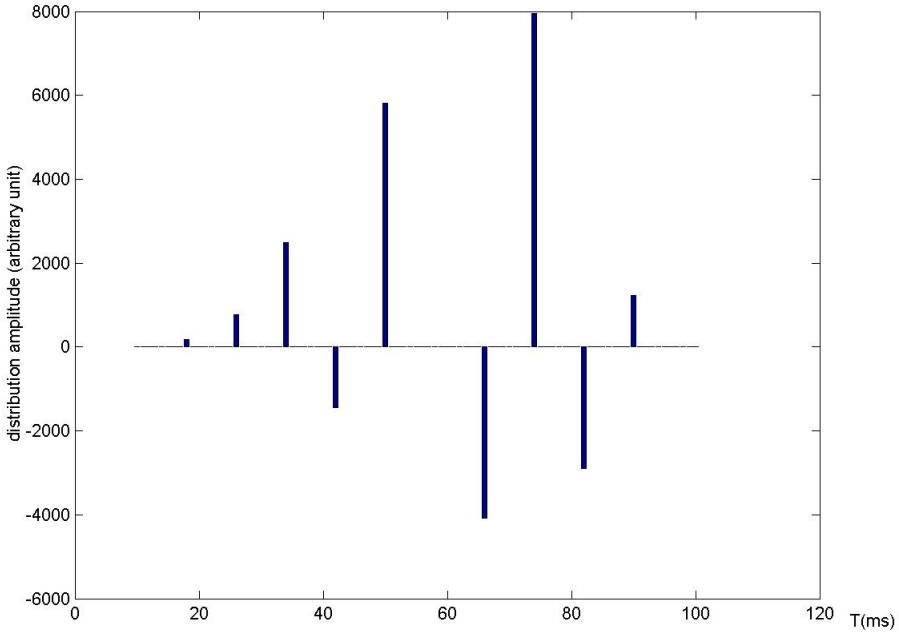


Figure 4.7: The solution solved by 10 delta functions.

Because the solutions cannot be constrained to be non-negative in this method, it is not ideally suited to the determination of physical density functions. But it can be used to detect baseline offsets and to denoise exponential decay data.

## 4.2 Modifying NNLS to solve the coefficients of the constituent functions

In the last two subsections, we showed that by the sampling method and the use of arbitrary constituent functions, the solutions cannot be constrained to be non-negative. For the physical problem, this is not acceptable. Non-negative least squares fitting (NNLS) gives non-negative vector solutions to the system (3.17). It can be modified to accomodate the sampling method and the use of arbitrary constituent functions, that is, to minimize

$$||f(t) - \sum_{n=1}^{N} c_n z_n(t)||_2, \tag{4.54}$$

where $z_n(t) = W_n(t)$ in the samping method, and $z_n(t) = S[\eta_n(T)]$ by use of arbitrary $\eta_n(T)$'s.

The algorithm of using NNLS in these methods is simply to add the matlab command used in Section 3.1.4, where $f$ in this command is the signal subtracting the baseline offset, after calling function "lsqsum" in MATLAB algorithms 1 and 2 in the previous sections which finds a baseline offset.

**Example 8.** ***Sampling together with NNLS***

*If the true distribution is non-negative, then its sampled points are also non-negative. So it is not reasonable to obtain negative numbers when solving for sampled values.*

*We use LSQNONNEG to solve for the sampled values in Example 5. Since NNLS*

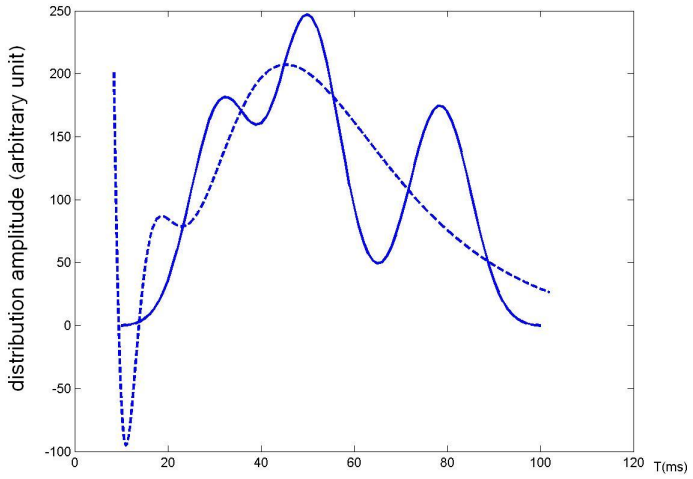


Figure 4.8: The true distribution (solid line) and the solved distribution (dashed line) by sampling together with NNLS, for the data set used in Example 5.

*alone does not solve the baseline well, we first solve C by (3.12)-(3.15), subtract this baseline from the data, and then invert the system. The previous sampled values and the new sampled values are listed in Table 4.1. The new reconstructed solution is plotted in Figure 4.8. Note that the new solution is still not non-negative. This is because that the interpolation functions, i.e., the* sinc *functions, are not non-negative.*

| $v_n$ | $P(x_n)$ without NNLS | $P(x_n)$ with NNLS |
|---|---|---|
| 0.0098 | 29073 | 27366 |
| 0.0162 | 57241 | 58382 |
| 0.0266 | 26292 | 25862 |
| 0.0439 | 42292 | 40827 |
| 0.0724 | -1828.5 | 0 |
| 0.1194 | 10931 | 14320 |

Table 4.1: Lists of sampling points and the sampled values without and with using NNLS.

**Example 9.** ***NNLS finding the coefficients of arbitrary constituent func-***

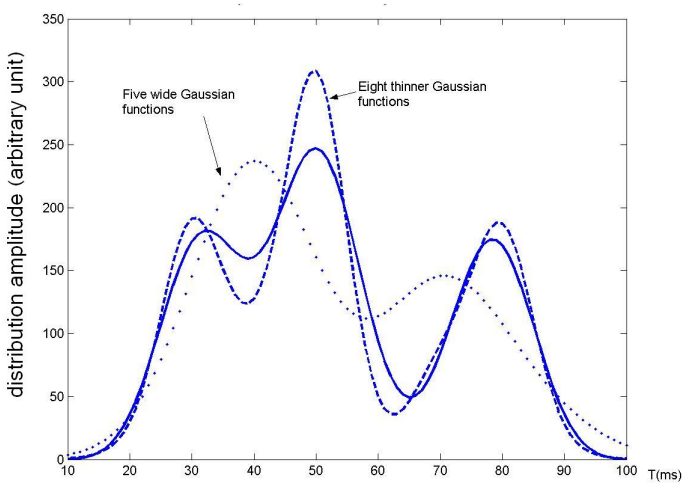


Figure 4.9: Use of arbitrary constituent functions together with NNLS. The solid line is the true $g(T)$. The dotted line is the solution by using the first set of constituent functions. The dashed line is from the second.

***tions***

*Using the same data set and the first two sets of constituent functions in Example 8, we use LSQNONNEG in MATLAB to find a positive* $\vec{c}$ *for each set. We found* $C$ *first, as done in Example 8 and subtract it from the data before inversion. The solutions are plotted in Figure 4.9. For all these plotted solutions, the magnitudes of the fitting residuals are less than* $0.001f(0)$.

*The number of iterations required in these two problems are 5 and 9, respectively. For the third set of constituent functions in Example 7, 39 steps are required to produce a final result. However this result is unreasonable since it is not non-negative which means that the algorithm fails (Figure 4.7). One might suspect that the failure is due to an insuffcient number of delta functions (The next example will show that this is not the real reason.) If we attempt to use more delta functions, the algorithm still does not give non-negative solutions for 22 and 91 delta functions, requiring 76 and 283 steps.*

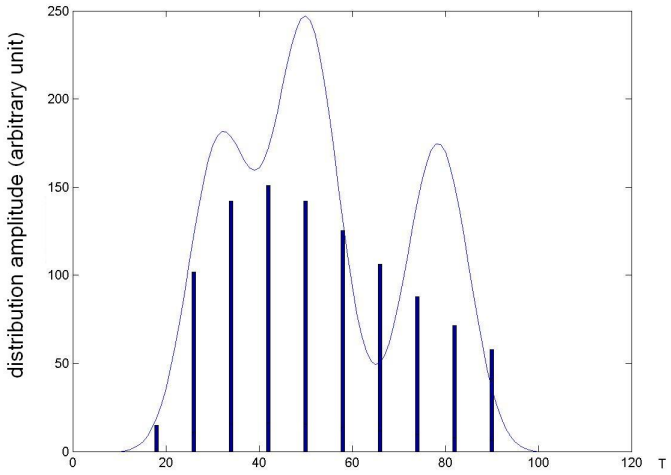


Figure 4.10: Use of a set of delta functions as constituent functions, together with NNLS and regularization. The solid line is the true $g(T)$. The bars is the solution for the third set of constituent functions in Example 5, divided by 10.

**Example 10.** ***Regularization for NNLS***

***1. Regularization increasing the chance of success of the algorithm***

*We use the same data set as in Example 7, and the third set of constituent functions in Example 7. The regularization is done by (4.52) with* $k = 0.1$*, so that* $\tilde{B}$ *is now a 2511 by 10 matrix.*

*The solution is plotted in Figure 4.10, and the residual is plotted in Figure 4.11. The result shows that this set of constituent functions is able to produce a reasonable solution. The number of iteration steps is 10. In the last example, this set of constituent functions did not yield a non-negative solution. The fact that now the algorithm is successful means that the previous failure was not due to the insufficiency of the number of delta functions, but rather to the way the iteration is carried out. When the algorithm fails, the solutions are like the one given in Figure 3.2. Regularization prevents such solutions from being given.*

***2. Effect of changing*** $k$

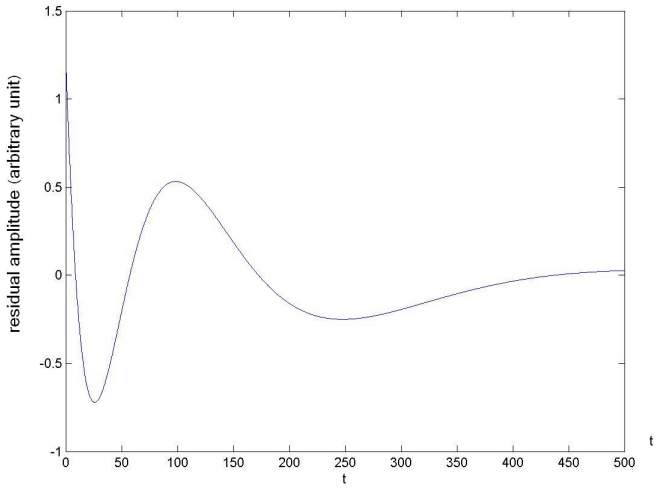


Figure 4.11: The residual for the solution using the delta functions defined in Example 7 as constituent functions by regularized NNLS.

*$k$ is the weight of regularization. For this example another set of constituent functions is used, which are seventeen very thin Gaussian functions, so that the effect of changing $k$ is more clear:*

$$\phi_i(T) = e^{-(T-10-5i)^2/10}, T = 10..100, i = 1..17.$$

*Figure 4.12 and 4.13 show the solutions and corresponding residuals for* $k = 0.1, 0.001$ *and* $0.0001$*. The numbers of iteration steps required are 18,19 and 14, respectively.*

Besides saving computing time and increasing the chance of success of the algorithm, another advantage of using constituent functions is that the spacing of $T$ points can be made arbitrarily small, since decreasing the spacing of $T$ points while leaving the number of constituent functions and $t$ points unchanged will not increase the time that iteration takes.

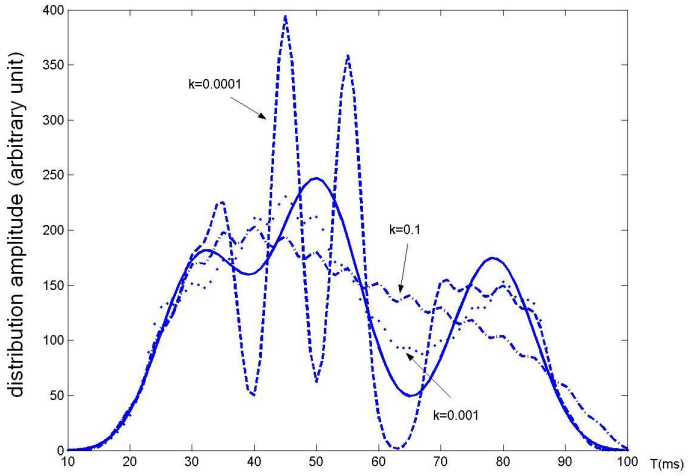


Figure 4.12: The solid line is the true $g(T)$. The dashdotted line is for $k = 0.1$. The dotted line is for $k = 0.001$. The dashed line is for $k = 0.0001$.

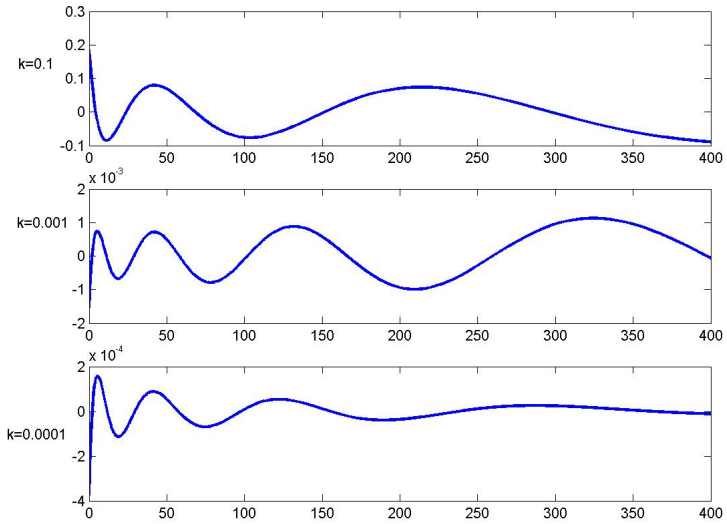


Figure 4.13: Residuals for $k = 0.1, 0.001, 0.0001$ sequentially.

## 4.3 Conclusions from the numerical instability and the reduction on number of unknowns

It has been shown in Examples 5-10 that solutions can be reasonable but very different from the true solution. In the physical problem, the solution is meaningful only if we can have the peak locations and the signal amplitudes belonging to each peak. If this information is incorrect, the solution is meaningless. This gives us the first conclusion:

**Conclusion 1.** ***Requirements on data***

*During data analysis we shall require that the center of the peaks for different species are far apart relative to the width of the peaks.*

If a discrete distribution model cannot make the residual look like a Gaussian white noise, one possibility is that there are wide peaks, the other possibility is that the assumption for the data analysis model is incorrect. For example there may be systematic errors. The fact that there is an upper bound of the number of constituent functions from which a solution can be constructed is sometimes an indicator of the second possiblity being true.

**Conclusion 2.** ***Detection of systematic errors***

*For a suitable $N$, if using $N$ constituent functions, the optimal solution will not make the residual look like a Gaussian white noise, then we would say that there are systematic errors.*

If the use of a few constituent functions may produce a good Gaussian white noise residual, then we should try to resolve the peaks by solving for the continuous distribution.

**Example 11.** ***Detection of systematic errors for a set of experimental data***

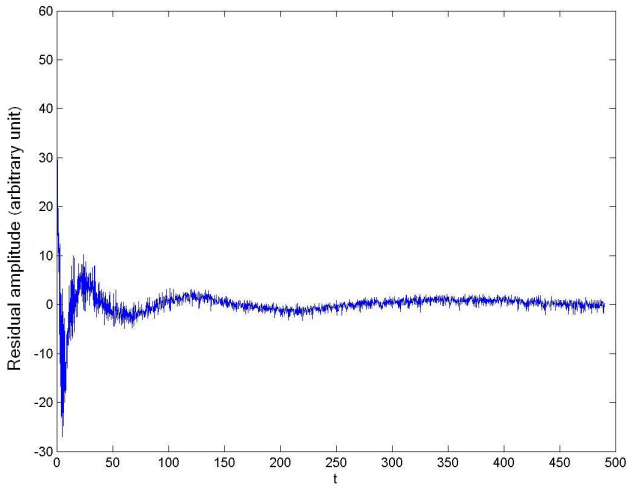


Figure 4.14: The residual using 20 constituent functions on [10,100].

*In one of our experiments using the 500 MHz machine on a water sample (Data Set 2 in Section 2.5), a single delta function model does not make the residual look like a Gaussian white noise. We know that this species should have a relaxation time within [10,100] ms. By assuming 20 linearly independent functions, which corresponds to* $\omega_{max} = 6.5$ *where*

$$\int_{\omega_{max}}^{+\infty} |\lambda_\omega| d\omega \approx 0.00004 \int_0^{+\infty} |\lambda_\omega| d\omega,$$

*we solve for the optimal solution by (3.12)-(3.15), which is not necessarily positive. The residual is plotted in Figure 4.14. The signal strength is about* $f(0) = 13000$ *and* $|C| < 5$. *The residual has too much time correlation. So we conclude that there are unknown systematic errors coming from the experimental environment.*

Note that if the best residual obtained through this method is a "good Gaussian white noise", there is still no guarantee that there is a non-negative $g(T)$ for whom the residual is a "good Gaussian white noise".

# Chapter 5

# Analyzing the Experimental Data

Now we apply the methods described in the previous section to real experimental data. For each set of data, we first employ the discrete data fitting algorithm LSQCURVEFIT function in MATLAB. If the residual is not "good Gaussian white noise", i.e., if it appears to exhibit some time correlations, then the method in Section 3.2.3 will be applied. If the best possible residual of this method is better than the residual in the discrete fitting, either the ordinary NNLS or the modified NNLS using constituent functions will be used to fit the data to a continuous distribution. In general, for our samples, the ordinary nonnegative least squares (NNLS) method described in Section 3.1.4 performs as well as the modified version by employing constituent functions. The continuous distributions consist mostly of narrow peaks and the ordinary NNLS algorithm does not consume too much time. As for the baselines that are passed into the NNLS algorithm, we use either the value determined by the iteration scheme assuming one or two components, or the value determined by finding the best possible residual from the constituent functions method.

We finally mention that the ORIGIN [52] software package and the CracSpin program [46] have been commonly employed by researchers in the NMR laboratory, Department of Physics,University of Waterloo, to extract relaxation times. Recall that ORIGIN also employs the iteration of parameters method but with a different

implementation than that used in MATLAB, as mentioned in Section 3.1.3. CracSpin uses a similar iteration scheme as that used in ORIGIN. In addition, a non-negative least-squares technique developed by Whittall [49] is used by a number of researchers in the medical physics area.

There are six data sets as were listed in Section 2.5. For these data sets, the best discrete fitting results by MATLAB had approximately the same values with those obtained by *Origin*.

1. **Data Set 1: Water (paramagnetic copper sulphate is added to shorten the $T_2$ relaxation time of the sample from that of pure water).**

   The solution is entirely liquid, and therefore is assumed to be homogeneous. Because of the equivalence of the two protons in the water molecule, we assume only one component in the sum of exponentials. We ran LSQCURVEFIT assuming one component with five randomly selected initial conditions. In all five runs the relaxation time converges to 32.87 ms, and the amplitudes all converge to 9293.8. The residual of the fit is plotted in Figure 5.1. Since there are some quite noticeable correlations near the start of the signal, we judge that this one component model does not fit the data set well. By the method in Section 4.1.3, the best possible residual is obtained by assuming 20 Gaussian functions as constituent functions on $[10, 100]$ ms. This residual, plotted in Figure 5.2, has the appearance of "good Gaussian white noise". Unfortunately, this solution, which did not involve NNLS, is not non-negative as seen in Figure 5.3. Therefore, we fitted the data again using the NNLS. However, for this data set, none of the continuous fitting method gives a better residual than the one-component iteration scheme does in terms of the $L_2$ norm and time correlation of the residual. After a few more experiments, we find that by the iteration scheme assuming up to four components, the residual cannot be made better unless negative amplitudes are allowed. Therefore, we judge the one-component result, for which the residual is pictured in Figure

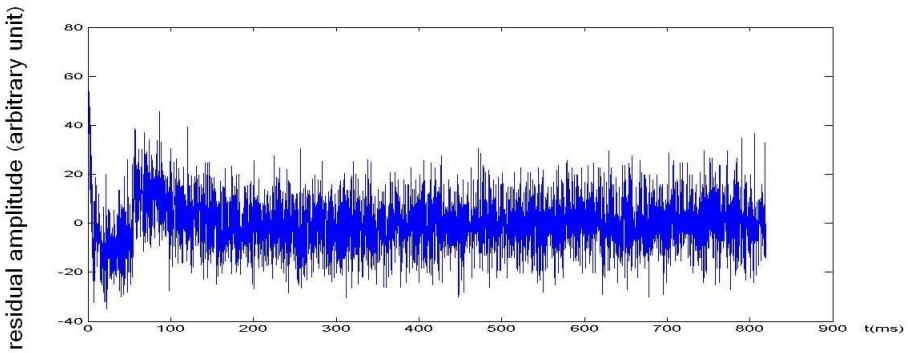


Figure 5.1: One-component fitting residual of Data Set 1.

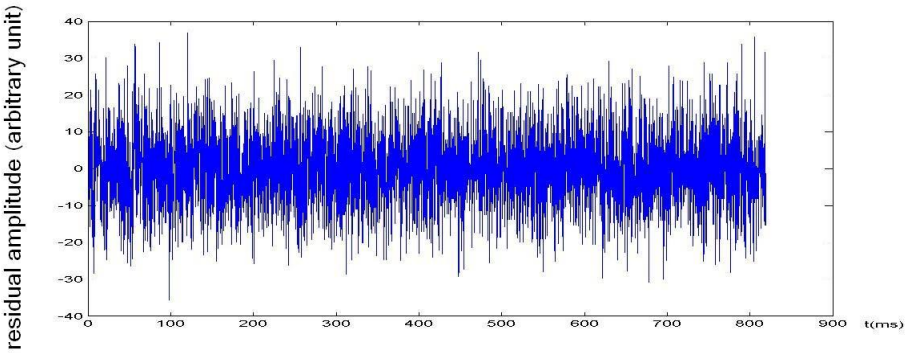


Figure 5.2: Best possible fitting residual of Data Set 1.

5.1, to be the best result. We also conclude that there are systematic errors in this data.

2. **Data Set 2: the same sample as in Data Set 1, but measured in a 500 MHz machine.**

   By using a different machine, we could test whether the relaxation time obtained by using the previous machine was affected by systematic errors. Once again, we ran the iteration scheme for five times with randomly selected initial values. In all five runs the relaxation time converged to 36.18 ms. Although this value is somewhat different from the 36.87 ms value obtained from the 30

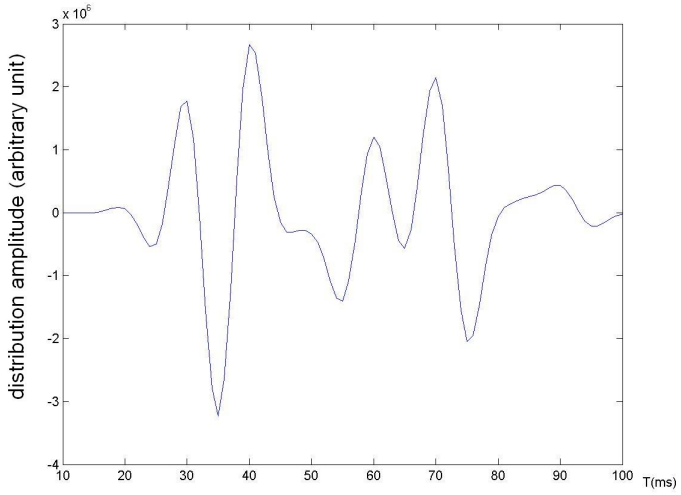


Figure 5.3: The solution for Data Set 1, solved by using 20 Gaussian constituent functions without using NNLS.

MHz machine data – about 2 % discrepancy – it is considered by NMR experimentalists to be reasonably close. Such differences are usually attributed to systematic errors and the presense of white noise. The residual is plotted in Firgure 5.4. This residual has about the same magnitude as that plotted in Figure 4.14 in Section 4.3, which is the best possible residual for this data, so fitting this data set to a continuous distribution will not improve the result much. As we can see, the two residuals for the Data Set 1 and 2 are very different, but the fitting results are about the same. We conclude that the systematic errors in these two data sets do not affect the fitting result.

3. **Data Set 3: A sample consisting of a single species of porous glass beads with pore diameter 273 Å, measured in the 30 MHz machine.**

   This sample was prepared to have only one species of porous material with controlled pore diameter. So theoretically there should be only one component in the sum of exponentials.

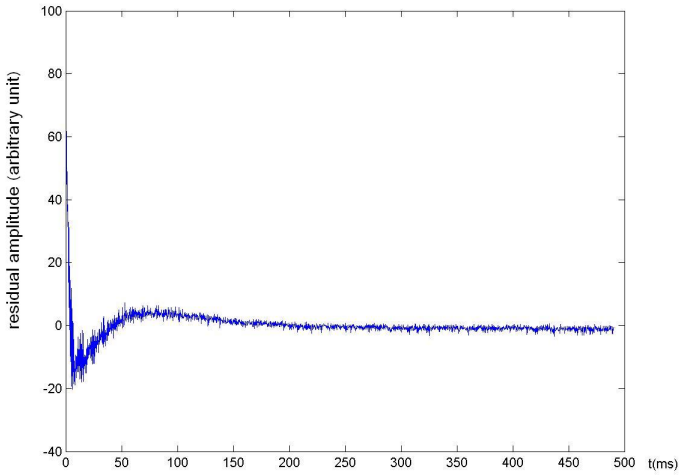


Figure 5.4: One-component fitting residual of Data Set 2.

In all five runs of LSQCURVEFIT assuming one component with randomly selected initial values, the relaxation time converged to 36.44 ms. Therefore we conclude that this porous medium has a relaxation time of around 36.44 ms when saturated. The relaxation times of the samples may vary slightly in each experiment because of slightly different levels of saturation.

The fitting residual for the best one-component fitting is plotted in Figure 5.5. And the best residual tested by the method in Section 4.2.3 is plotted in Figure 5.6. The latter residual is much better in terms of $L_2$ norm and time correlation of the residual. So we shall fit this data set to a continuous distribution.

The continuous distribution obtained by NNLS using 20 Gaussian functions on $[10, 100]$ as constituent functions is plotted in Figure 5.7, and its fitting residual is plotted in Figure 5.8.

In the solution shown in Figure 5.7, the mean value of the large peak is about 36.9, which is consistent with the one-component iteration result. There is a very small peak over $T \in [10, 20]$. The total amplitude belonging to this peak

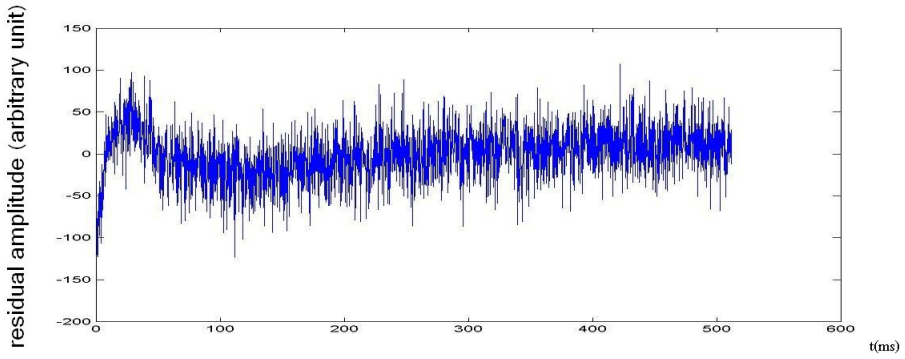


Figure 5.5: Residual from fitting Data Set 3 by one component.

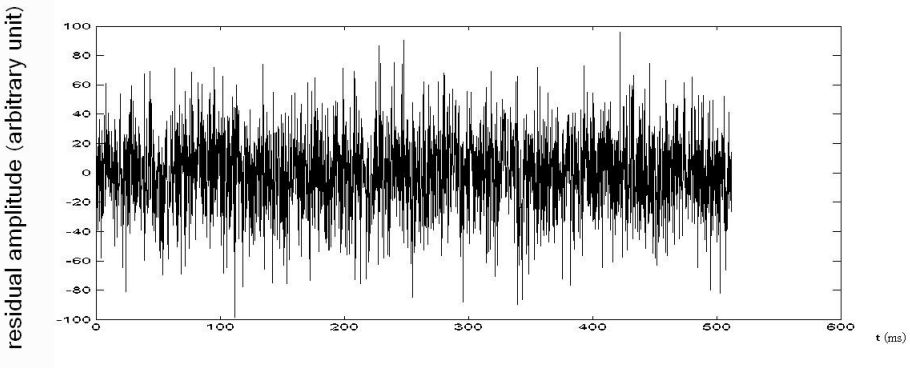


Figure 5.6: The best possible residual for Data Set 3.

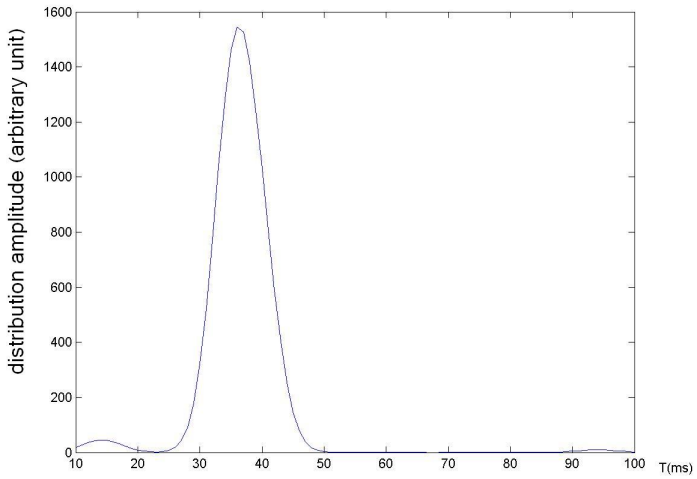


Figure 5.7: The continuous solution solved by NNLS using 20 constituent functions for Data Set 3.

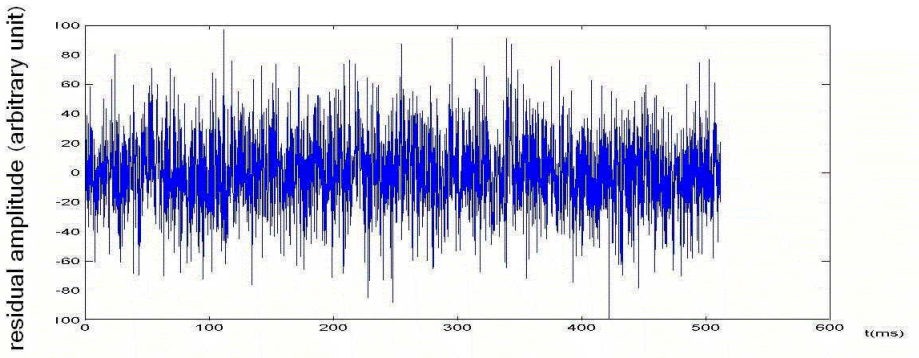


Figure 5.8: The fitting residual of the solution plotted in Figure 5.7.

(the integral of the solution over this peak) is about 250. Because of the large resolution of the problem when $T$ is small, this small peak can have a significant effect to the fitting residual, and is therefore not negligible numerically. This small peak can be due to the water molecules that really have relaxation times within $[10, 20]$, for example, the water molecules in undesired small tunnels in the glass bead. Or this peak can be due to systematic errors. From the analyses of Data Set 1 and this data set, we see that the systematic errors for the same machine may be quite different at different times. To verify which possibility is true, the experiment should be repeated. However, since here it does not affect the main fitting result, we did not proceed with such a verification.

Our fitting result differs from the result for a material with the same pore diameter in [19]. But in [19], the data sets are fitted to stretched exponentials as in (2.68). If our material were the same as what were used in [19], this sample is about half-saturated, and should have a stretching parameter $\beta = 0.9$. But after an attempt to fit our data to a stretched exponential, we found that introducing a $\beta < 1$ only made the residual worse. And so our sample is not the identical material as they used. In such a case, the parameters in the two-site model for these materials are different, and so they could have different relaxation times when saturated. But since we are only concerned with the numerical schemes that solve the relaxation times assuming a sum of exponentials, we will not explore any disagreements between our fitting results and those of others.

4. **Data Set 4: A single species of porous media with pore diameter** 491 **Å measured in the 30 MHz machine**

   In all five runs of LSQCURVEFIT assuming one component with randomly selected intial conditions, the relaxation time converges to 63.81 ms. The residual obtained from one-component fitting is plotted in Figure 5.9. And the best possible residual is plotted in Figure 5.10. Again, the $L_2$ norm and time correlation of the residual from one-component fitting is worse than those of

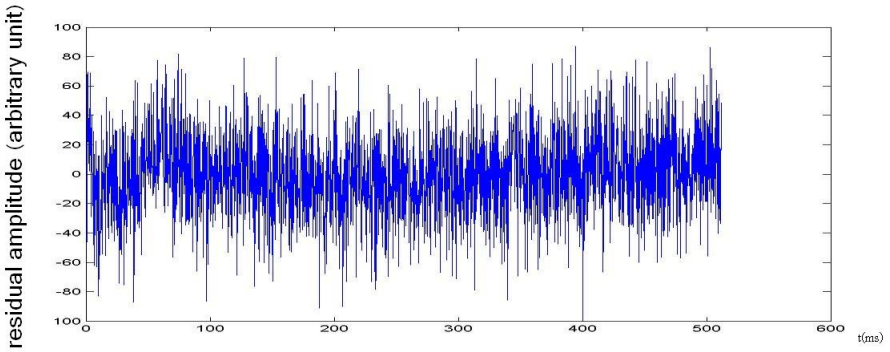


Figure 5.9: residual from fitting the data set for Data Set 4 by one component.

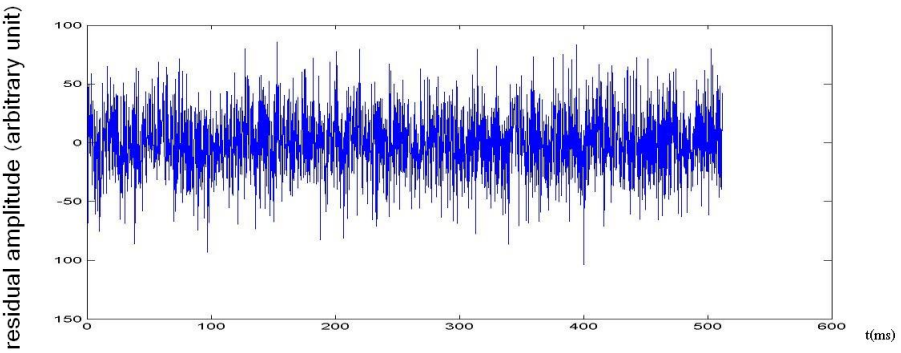


Figure 5.10: The best possible residual for Data Set 4.

the best possible residue, we shall fit this data set to a continuous distribution. The solution obtained by NNLS using 20 Gaussian functions as constituent functions is plotted in Figure 5.11, and the fitting residual for this solution is plotted in Figure 5.12. This residual is a little better than that of the one-component fitting, in terms of the $L_2$ norm.

In the solution plotted in Figure 5.11, the mean value of the large peak is 63. There is a small peak for $T \in [90, 100]$. Again we will ignore it but whether or not it is the result of systematic errors might be verified by repeating the experiment.

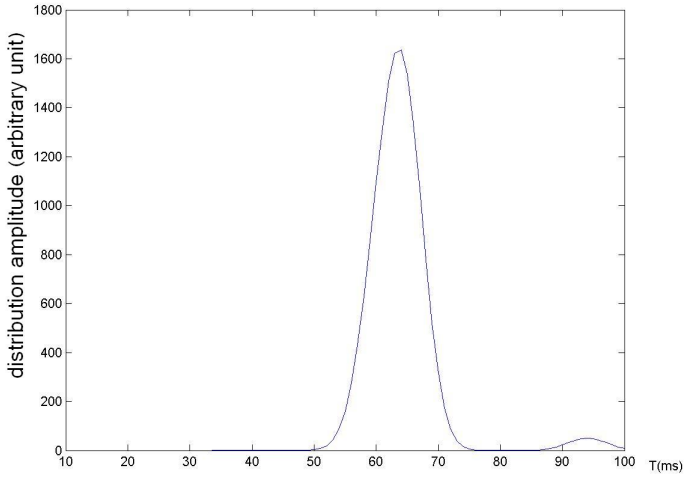


Figure 5.11: Solution obtained by NNLS using 20 constituent functions for Data Set 4.

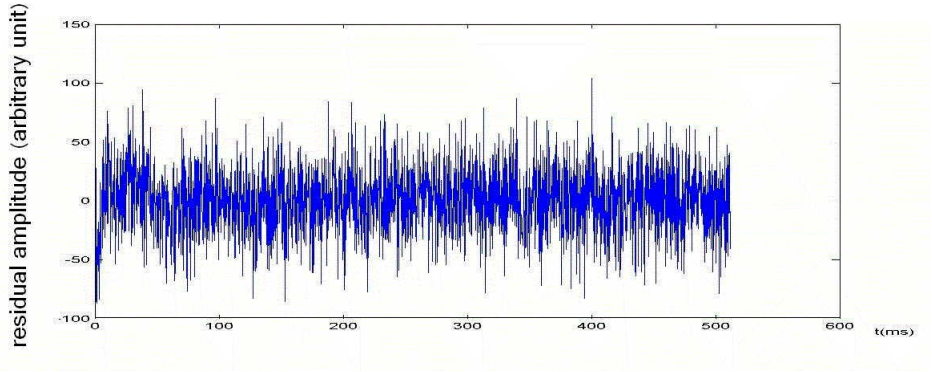


Figure 5.12: The fitting residual of the solution plotted in Figure 5.11.

| $A_1$ | $T_1$ | $A_2$ | $T_2$ | $C$ | norm of residual |
|---|---|---|---|---|---|
| 15740.95 | 43.91 | 4794.16 | 76.69 | -4540.49 | 1468.56 |
| 15031.67 | 43.34 | 5505.54 | 72.04 | -4538.39 | 1477.82 |
| 14765.55 | 43.14 | 5771.57 | 71.18 | -4537.71 | 1481.46 |
| 11215.29 | 40.29 | 9324.22 | 63.49 | -4530.27 | 1537.09 |
| 10134.09 | 39.30 | 10410.11 | 61.94 | -4528.82 | 1556.80 |

Table 5.1: Iteration results for Data Set 5.

5. **Data Set 5: A mixture of the two species of porous glass beads that were used for the last two data sets with proportion 6:5 in pore volume.**

   The numerical experiments performed on this data set are similar to those of the previous samples, except that for LSQCURVEFIT we assumed two components.

   Table 5.1 contains the fitting results in five runs of the algorithm with randomly selected initial conditions. The results are sorted in their $L_2$ norms of residuals.

   In Figure 5.13 the residual for the parameters in the first row of Table 5.1 is plotted. If we assume that the saturation level for the two kinds of pores are about the same, which is very likely to be true as the two samples were saturated together in the same beaker, then the proportion in the amplitudes of the signal given by the two species should be about 6:5. In the best result shown in the table, the proportion of the amplitudes is quite different from the way in which the sample was prepared, and the relaxation times are much larger than the results from the measurements of individual species. As a comparison, the fourth row of the table is closer to what we could have predicted by the previous measurements and the way this sample is prepared. However, its norm of residual is much higher than that of the first result.

   Figure 5.14 plots the best possible residual. Again we should fit this data set to a continuous distribution. Figure 5.15 plots the solution obtained by NNLS using 20 constituent functions. And its residual is plotted in Figure 5.16. This

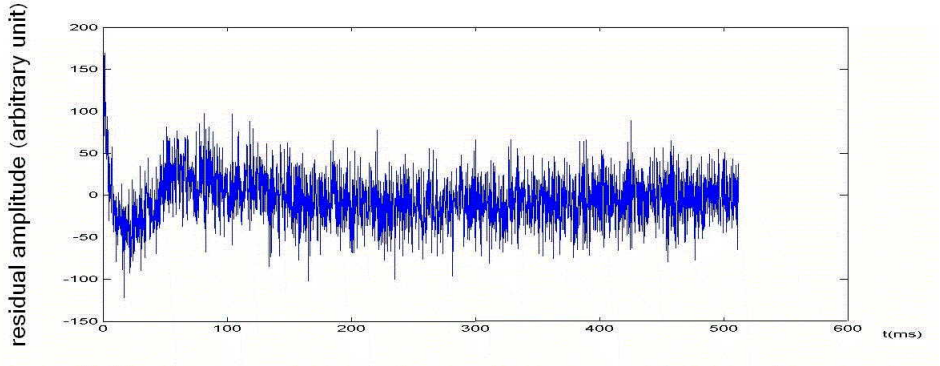


Figure 5.13: The residual from fitting Data Set 5 by assuming two components.

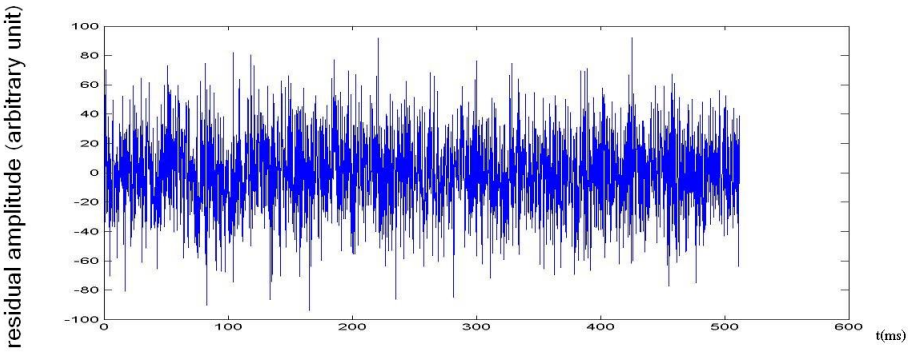


Figure 5.14: The best possible residual for Data Set 5.

solution is consistent with the iteration fitting result. The two peaks have mean values of about 47 and 82. Its residual is a little better than that for the two-component iteration fitting in terms of the $L_2$ norm.

6. Data Set 6: A mixture of the two species with proportion 1:3 in pore volume. The same numerical experiments as those for Data Set 5 were done. In Table 5.2 are listed the fitting results of five runs with randomly selected initial conditions, sorted in their $L_2$ norm of residual. In Figure 5.17 is plotted the residual for the result in the first row in the table. Figure 5.18 plots the best possible residual solved by constituent functions. The best possible residual seems like a "good Gaussian white noise". We will fit this data set to a con-

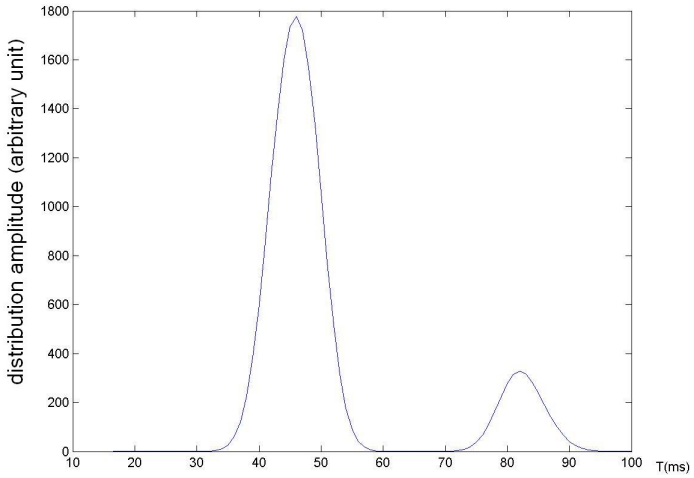


Figure 5.15: NNLS solution for Data Set 5 using 20 constituent functions.

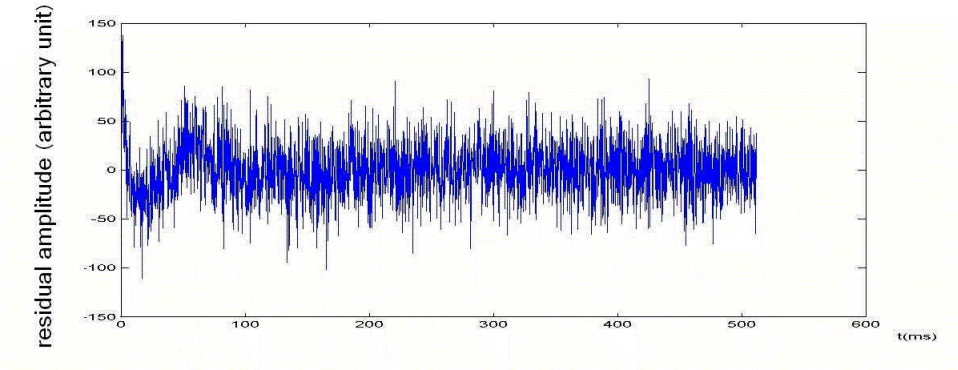


Figure 5.16: The residual for the solution plotted in Figure 5.15.

| $A_1$ | $T_1$ | $A_2$ | $T_2$ | $C$ | norm of residual |
|---|---|---|---|---|---|
| 3809.12 | 44.572 | 6466.71 | 76.61 | -3107.9 | 613.95 |
| 3473.32 | 43.33 | 6804.08 | 75.554 | -3106.8 | 614.61 |
| 3472.04 | 43.329 | 6805.30 | 75.55 | -3106.8 | 614.61 |
| 4787.98 | 47.64 | 5484.38 | 79.988 | -3110.9 | 617.54 |
| 2576.4 | 39.306 | 7705.1 | 72.876 | -3103.5 | 640.64 |

Table 5.2: Iteration results for Data Set 6.

tinuous distribution. The solution by NNLS using 20 constituent functions on $[10, 100]$ is plotted in Figure 5.19, and the corresponding residual is plotted in Figure 5.20. This solution is quite different from a two-component exponential decay. Consider the problem found in the two-component fitting for this data set, and the numerical instability of solving the continuous problem, we cannot obtain much information from this continuous fitting result.

The situation here is similar to the results for Data Set 5. The last row is cloest to what would have been predicted from the experimental preparation, yet yields the highest residual error. The "best" result, i.e., the one with the lowest residual norm, has an incorrect proportion in amplitudes and the relaxation times are larger than what they are for individual species. There are two possibilities for this phenomenon: (1) The fourth row represents approximately the true parameters. The fact that the first row yields the best fitting is due to systematic errors, or is because that the samples either the single species samples or the mixtures were prepared improperly. (2) The mixture of two species of porous media cannot simply be considered as a union of the two independent components. There may be other unknown physical processes at play. First of all, we believe that these samples are mixed well at the microscopic level. As such there are no significant one-species regions in the mixture. There can be unknown physical processes as a result of the species being mixed. For example, it has been suggested [35] that "fast exchange" of water molecules between small pores and large pores may make the relaxation times different from what they are for individual species. However, it was also suggested in [35] that although the fast-exchanges can explain the relaxation time distribution of the mixtures, these fast-exchanges are unlikely to occur, as we believe that the surfaces of beads are totally dry before the measurements. The effect of mixing can be tested by performing an experiment with the two species separated in the tube. Indeed, we performed such an experiment in which the two species were separated by a piece of parafilm in the tube. The

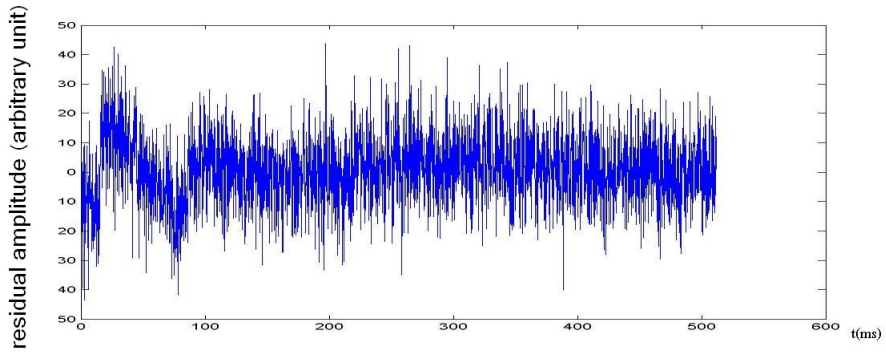


Figure 5.17: residual from fitting the data set for Data Set 6 by assuming two components.

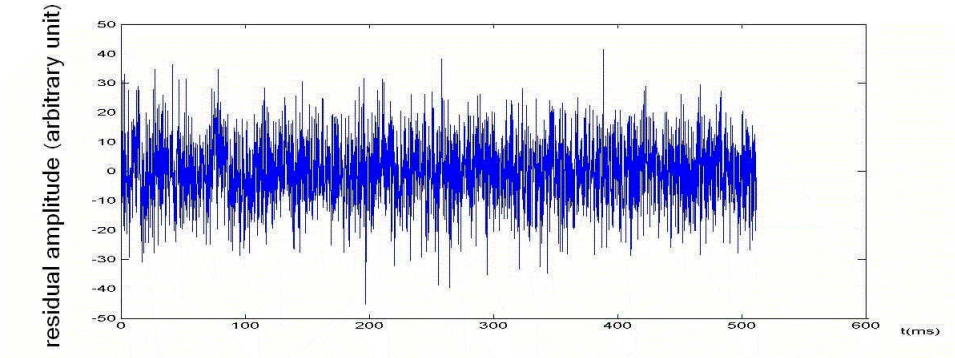


Figure 5.18: The best possible residual for Data Set 6.

proportion of the two amplitudes was very close to what it could be predicted from the sample preparation. Unfortunately, this experiment was not well controlled, in that the sample was not fully saturated and there is a much greater off-resonance occuring than what was analyzed in Section 2.6. As a result, we shall not present the data or the results of the experiment.

It is unlikely that the unreasonable fitting results are due to numerical instability only, since when we tried to fit the addition of Data Set 3 and Data Set 4, the fitted relaxation times by a two-component iteration are still around 36 ms and 63 ms.

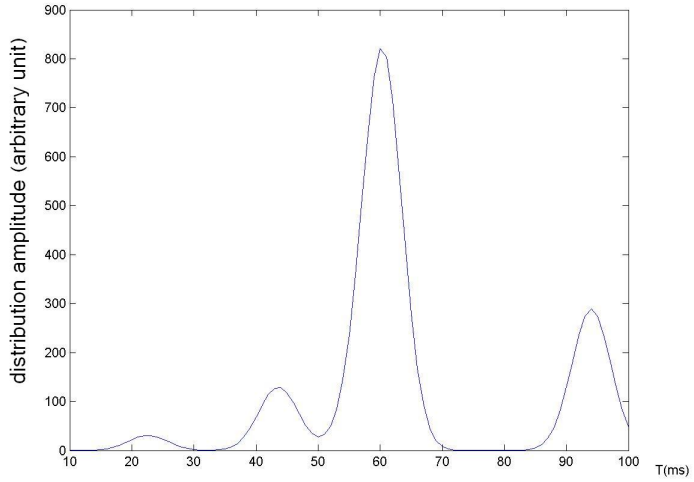


Figure 5.19: The solution solved by NNLS using 20 constituent functions for Data Set 6.

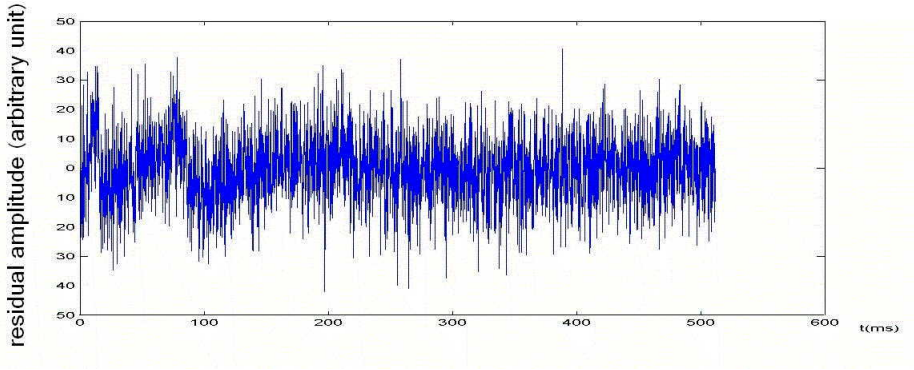


Figure 5.20: The residual for the solution plotted in Figure 5.19.

## Summary of results

In summary, our water solution sample has the spin-spin relaxation time $T_2$ of about 36 ms. This result agrees with previous measurements by Jianzhen Liang from the Department of Physics, University of Waterloo. Systematic errors do not seem to produce large deviations of the fitted relaxation times.

The glass gel with smaller pores has a $T_2$ value of about 36 ms, and the other species with larger pores has a $T_2$ value of about 63 ms. The pore inhomogeneity in terms of the variance of the pore diameter is comparable for these two kinds of glass gel. By fitting the single-species data sets to continuous distributions, the mean of the relaxation times we obtain are about the same as what we obtain from the one-component fitting.

When the two species are mixed, the fitting results are undesirable, which may be due to fast-exchange phenomenon and/or systematic errors. It may also be possible that some of the samples were not prepared properly, for examples, some were possibly not fully saturated, or not fully try outside the beads. The reliablility of the data sets can be tested by repeating the sample preparation procedure and the measurements. Based on what we have concluded from the experiments on the water solution sample, it is very likely that the systematic errors do not change the fitting result very much. Also by virtually mixing the two species, through the addition of Data Set 1 and Data Set 2 and fitting the curve assuming two components, we found that the undesirable results are not due to numerical instability or systematic errors that are no larger than those in our one-species experiments. Therefore we conclude that there is a large possibility that unknown physical processes occur during mixing. This, of course, should be tested by more experiments.

# Chapter 6

# Conclusions and Discussions

This thesis presents an exploration of CPMG data analysis in the study of NMR applied to porous media. Here we summarize the key points made in the previous chapters. For the numerical analysis of the inverse problem involving the CPMG data, we have made the following assumptions:

1. The relaxation time for a porous material obeys the two-site model.
2. There is no slow diffusion (as opposed to fast-exchanges) in a saturated porous material.
3. The stretched exponential model is not considered.
4. The noise component in the signal is additive Gaussian white noise. The $L_2$ norm is used for comparing the "goodness" of a Gaussian white noise with the same variance.
5. The off-resonance of the 30 MHz machine is less than 10 kHz, and the pulse length error is less than 4%.

With the above assumptions, we have the following results for CPMG data analysis:

1. Off-resonance and pulse length errors within above assumed values do not affect the fitting results to a noticable degree. The existence of off-resonance or off-resonance together with pulse length error can be detected by a Fourier transform of the fitting residual as this residual will have a beat pattern.

2. Iteration schemes are the best for solving the discrete problem. They work well with noise. The results found by this method are very accurate. With presence of systematic errors, by looking at non-optimal solutions we could find more possibilities for the parameters. If the number of components is not given, it can be found by checking when an increase of the number of components does not improve on the fitting residual.

3. Non-negative least squares (NNLS), which involves the solution of a large matrix system, is the best method for the continuous problem, because it yields non-negative solutions which are particularly suitable for our physical problem. In addition, NNLS can be accompanied with regularization methods in order to guarantee that the solution is meaningful to some extent. There are disadvantages, however. When a suitable level of regularization is used, NNLS can takes a long time (one minute for 100 relaxation time points and more than six minutes for 200 relaxation time points). NNLS is not suitable for the discrete problem, because that the number of the components cannot be constrained and the true components can be split or merged.

4. Regularization can constrain on the smoothness of an NNLS solution. And regularization sometimes increases the chance of success of the NNLS algorithm (Example 10).

5. The ill-posedness of the separation of exponentials is due to the fact that the data may not always be expressible in the form to which it is fitted, because of the presense of noise. The ill-conditioning of the problem can be illustrated very well by the eigensystem of the Laplace transform. The eigenfunctions of the Laplace transform are Fourier-like, and the eigenvalues are very small

when the frequency is large, if we say that the transform is taken from time domain to frequency domain. Both the ill-posedness and the ill-conditioning are sources of numerical instability of the problem.

6. Numerical instability of the separation of exponentials problem makes it difficult to guarantee the accuracy of the solution in the presence of noise. One example showed that in the presense of Gaussian white noise, the "best" solution, i.e., the one that minimizes the $L_2$ norm of the residual may differ significantly in some components from the true solution. In fact, we have not found a way to, or a class of situations under which, the accuracy of the solution can be guaranteed.

7. The resolution of the problem of separation of exponentials worsens logarithmically with increasing $T$.

8. For any Fredholm integral equation of the first kind, the numerical solution can be found by solving a (possibly very big) linear system resulted from using a numerical quadrature rule for the integral (such as NNLS does). If the solution can be expressed as a sum of several constituent functions, then the coefficients for these constituent functions become the unknowns in the problem. In this way the number of unknowns is much smaller than that in the ordinary NNLS algorithm.

9. For the separation of exponentials problem, an expansion in terms of the eigenfunctions of the Laplace transform gives a small cut-off in the frequency. When the frequency is discretized and the integral in the integral equation is infinite, we need to assume a large interval for the variable in the time domain so that the differences between transforming the eigenfunctions on this interval and transforming the eigenfunctions on the whole positive half axis are negligible.

10. Inverting the Laplace transform by assuming a sum of the eigenfunctions for our physical problem is not practical, because the domain of the solution cannot

be assumed small (see the last result), which is not consistent with our physical problem. Since the eigenfunctions are Fourier-like, the solution can be obtained by means of the Sampling Theorem, for which the constituent functions are sinc functions, and the solution can be sampled on a small interval. It is not possible to contrain the sampling method for the purpose of yielding non-negative solutions, since the sinc functions are not non-negative.

11. By an expansion of the solution in the eigenfunctions of the Laplace transform, it was also shown that the constituent functions can be arbitrary. By assuming positive arbitrary constituent functions, NNLS can be used to find non-negative coefficients thereby yielding a non-negative solution. With the reduced number of unknowns, the NNLS algorithm is faster and is not likely to fail. NNLS using constituent functions can also be accompanied by regularization.

12. By using constituent functions, the spacing of $T$ in the solution can be made arbitrarily small. Without NNLS, the solution by using constituent functions can be found by programming which requires an inversion of a small matrix (of size up to 20 in our examples) and no other special routines. This can be used to find the baseline offset and perform denoising on the data when solving an Fredholm integral equation of the first kind. When sufficiently many constituent functions are used, if the residual cannot be made a Gaussian white noise, then we conclude that systematic errors are present.

Besides the numerical results, we have analyzed six real experimental data sets. We found in our experiments that there usually are systematic errors, and that these errors are not the same all the time. However, we have also found that these systematic errors may not affect the fitting results very much. An interesting phenomenon was observed in the case of the mixture data sets. The two fitted relaxation times for these data sets are greater than those fitted from single-species data sets, and the amplitudes of the relaxation time distributions are biased to the small relaxation time component.

## 6.1 Future possibilities

Although we have performed a good deal of data analysis, there are still many topics in this context that can be explored further. Physically, if the pores in the material are not clean, i.e., there are so called paramagnetic impurities, then the data may need to be fitted to a stretched exponential (2.68). It would be worth seeing what happens if we fit a stretched exponential curve to a non-stretched exponential decay, so that the paramagnetic impurities can be detected without fitting the data to stretched exponentials. And if there are many species, or there is a distribution of the relaxation values, then suitable algorithms may be developed for stretched exponentials. In fact by the change of variable $T = 1/\lambda$, the integral equation corresponding to the stretched exponentials still has a symmetric kernel, and the algorithms can be similar to those described in this thesis.

More physical experiments for mixtures should be performed in order to test whether or not there are fast-exchanges of water molecules between pores or whether there are other microscopic physical phenomena that could give a dominating component in between the two relaxation times for the two species. If by separating the two species in the tube, for example by a piece of parafilm, for the mixture samples, the fitting results are still inconsistent with how the samples were prepared and what are the fitting results for the single-species samples, then the unknown physical processes are not the cause of our fitting results, and the inconsistency between the single-species data sets and the mixture data sets should be due to noises, systematic errors, or problems during sample prepatation.

We have assumed that off-resonance and pulse length errors smaller than the certain values. However, our experiment involving the two separate and unmixed porous media, which was designed to check for the existence of fast-exchanges, yield greater off-resonance and/or pulse length error than assumed. As a result, we concluded that the data set was too difficult to analyze. Some more numerical experiments could have been done to see what are the effects to the fitted values if these errors

are larger.

And numerically, the method of detecting systematic errors we have developed is limited. Although we have a method to see what could be the best residual for a data curve, comparably good residuals may not be achievable by a non-negative distribution. Therefore with continuous fitting, if the residual resulting from a non-negative distribution is worse than the best possible residual obtained by using arbitrary constituent functions without NNLS, we still do not know whether there can be a better non-negative solution. We can only say that systematic errors exist if the best possible residual is not a "good" Gaussian white noise.

Finally, we have simply employed the $L_2$ norm to compare the residuals. By further testing time correlations and the probability distributions of the residuals, we may have a more robust criterion on the "goodness" of the residuals. Also the noise component in real experiments could be coloured noise. It is possible to assume other noise models for data anlyses.

# Appendix A

# Representative Values for Variables

| | | |
|---|---|---|
| $\gamma$ | gyromagnetic ratio of a water molecule | $2.68 \times 10^8$rad/s/T(esla) |
| $B_{rf}$ | pulse field strength | 4 mT |
| $B_0$ | static field strength | 1 T |
| $\omega_0$ | Larmor frequency $\gamma B_0$ | $2\pi$30 MHz |
| $b$ | $\gamma B_z$,off-resonance | 1 kHz |
| $M_0$ | equilibrium longitudinal magnetization, for water | $1.7 \times 10^{-9}$ T/cm$^3$ |
| $T_1$ | longitudinal relaxation time, for bulk water | 3.6 s |
| | in fully saturated pores with diameter 237 Å[19] | 2 s |
| | in fully saturated pores with diameter 491 Å | 2 s |
| $T_2$ | transverse relaxation time, for bulk water | 3.6 s |
| | in fully saturated pores with diameter 237 Å | 80 ms |
| | in pores with diameter 491 Å | 130 ms |
| $t_\pi$ | $\pi$ pulse length | $3 \times 10^{-6}$ s |
| $t_{\pi/2}$ | $\pi/2$ pulse length | $1.5 \times 10^{-6}$ s |
| $t_E$ | dephasing length | 0.1 ms |
| $D$ | diffusion constant of bulk water | $2.1 \times 10^{-5}$ cm$^2$/s |

# Bibliography


[1] Abragam, A., *The principles of nuclear magnetism,* Clarendon Press, Oxford (1983).

[2] Airapetyan, R.G. and Alexander, G.R., *Numerical inversion of the Laplace transform from the real axis,* J Math. Anal. Appl., 248, 572-587 (2000).

[3] Aubard, J., *Direct analysis of chemical relaxation signals by a method based on the combination of Laplace transform and Padé approximations,* Comput. Chem., 11, 3, 163-178 (1987).

[4] Blinc, R., Lahajnar, G., Zumer, S. and Pintar, M.M., *NMR study of the time evolution of the fractal geometry of cement gels,* Phys. Rev. B, 38,4, 2873-2875 (1988).

[5] Deurer, M., Vogeler, I., Khrapitchev, A., and Scotter, D., *Imaging of water flow in porous media by magnetic resonance,* J. Environ. Qual., 21, 487-493 (2002).

[6] Blinc, R., Dolinsek, J., Lahajnar, G., Sepe, A., Zupancic, I., Zumer, S., Milia, F., and Pintar, M.M., *Spin-lattice relaxation of water in cement gels,* Z.Naturforsch., 43a, 1026-1038 (1988).

[7] Bloch, F.A., *Nuclear induction,* Phys. Rev., 70, 460-474 (1946).

[8] Brownstein, K.R. and Tarr, C.E., *Spin-lattice relaxation in a system governed by diffusion,* J. Magn. Res., 26, 17-24 (1977).

[9] Carr, H. Y. and Purcell, E. M., *Effects of diffusion on free precession in nuclear magnetic resonance experiments,* Phys. Rev., 94, 3, 630-638 (1954).

[10] D'Orazio, F., Tarczon, J., Halperin, W.P., Eguchi, K, and Mizusaki, T., *Application of nuclear magnetic resonance pore structure analysis to porous silica glass,* J. Appl. Phys., 65(2), 15, 742-751 (1999).

[11] Dullien, F. A. L. *Porous media: fluid transport and pore structure,* Academic Press, London, United Kingdom (1979).

[12] Gaspard Riche de Prony, *Essai expérimental et analytique, Sur les lois de la dilatabilité des fluides élastiques et sur celles de la force expansive de la vapeur de leau et de la vapeur de lalkool, à différentes températures* Journal de l'Ecole Polytechnique, 1, 2, 24-76 (1795).

[13] Glasel, J.A., *NMR relaxation in heterogeneous systems,* Nature, 227, 704-705 (1970).

[14] Gutierrez-Osuna, R., Nagle, H.T. and Schiffman, S.S., *Transient response analysis of an electronic nose using multi-exponential models,* Sensors and Actuators B, 61, 170-182 (1999).

[15] Haacke, E.M., *Magnetic resonance imaging: physical principles and sequence design,* John Wiley, N.Y. (1999).

[16] Jacques Hadamard, *Sur les problèmes aux dérivées partielles et leur signification physique,* Princeton University Bulletin, 49-52 (1902).

[17] Hahn, E.L., *Spin echoes,* Phys. Rev., 80, 4, 580-594 (1950).

[18] Hinshaw, W.S. and Lent, A.H., *An introduction to NMR imaging: From the Bloch equation to the imaging equation,* Proc. IEEE, 71, 3, 338-350 (1983).

[19] Holly, R., *Water proton spin relaxation in porous silica glass,* Master thesis, Department of Physics, University of Waterloo, Ontario, Canada (1996).

[20] Kaiser, R., Bartholdi, E. and Ernst, R.R., *Diffusion and field-gradient effects in NMR Fourier spectroscopy,* J. Chem. Phys., 60, 8, 2966-2979 (1973).

[21] Kallianpur, G. and Karandikar, R.L., *White noise theory of prediction, filtering and smoothing,* Gordon and Breach Science Publishers, UK (1988).

[22] Kroeker, R.M. and Henkelman, R.M., *Analysis of biological NMR relaxation data with continuous distributions of relaxation times,* J. Magn. Res., 69, 218-235 (1986).

[23] Kumaresan R. and Tufts, D. W., *Estimating the parameters of exponentially damped sinusoids and pole-zero modeling in noise,* IEEE Trans. Acoust., Speech, Signal Processing. ASSP-30, 6, 833-840 (1982).

[24] Kuperman, V., *Magnetic resonance imaging: physical principles and applications,* Academic Press, London, United Kingdom (2000).

[25] Lanczos, C., *Applied analysis,* Prentice Hall, Englewood Cliffs, N.J. (1957).

[26] Lauterbur, P.C., *Image formation by induced local interactions: examples employing nuclear magnetic resonance,* Nature, 242, 190-191 (1973).

[27] Lawson, C.L. and Hanson, R.J., *Solving least squares problems,* Prentice-Hall, Englewood Cliffs, N.J. (1974).

[28] Longman, I.M., Int. J. Comput. Math.(B), 3, 53-64 (1971).

[29] MacTavish, C., Miljkovic, L., Pintar, M.M., Blinc, R. and Lahajnar, G., *Hydration of white cement by spin grouping NMR,* Cement and concrete research 15, 367-377 (1985).

[30] Mansfield, P., *NMR 'diffraction' in solids?* J. Phys. C: Solid State Physics, 6, L422-L426 (1973).

[31] Markel, J.D. and Gray, A.H., Jr., *Linear prediction in speech,* Springer-Vertag Berlin Heidelberg, Germany (1976).

[32] Marks, R.J., *Introduction to shannon sampling and interpolation theory,* Springer-Verlag, New York (1991).

[33] McWhirter, J.G. and Pike, E.R., *On the numerical inversion of the Laplace transform and similar Fredholm integral equations of the first kind,* J. Phys. A: Math. Gen., 11, 1729-1745 (1978).

[34] Ostrowsky, N., Sornette, D., Parker, R. and Pike, E.R., *Exponential Sampling Method for Light Scattering Polydispersity Analysis,* Journal of Modern Optics, 28, 8, 1059-1070(1981).

[35] Peemoeller, H., private communication.

[36] Purcell, E.M., Torrey, H.C. and Pound, R.V., *Resonance absorption by nuclear magnetic moments in a solid,* Phys. Rev., 69, 37-38 (1946).

[37] Ramm, A.G., *Inversion of Laplace transform,* Inverse Problems, 2, L55-L59 (1986).

[38] Schlesinger, J. , Nucl. Instr. and Meth., 106, 503 (1973).

[39] Sobol, W.T., Cameron, I.G., Pintar, M.M., and Blinc, R., *Stretched exponential nuclear magnetization recovery in the proton pseudo-spin-glass* $Rb_{1-x}(NH_4)_xH_2AsO_4$, Phys. Rev. B, 35, 13, 7299-7302 (1987).

[40] Stewart, W.A., MacKay, A.L., Whittal, K.P., Wayne Moore, G.R. and Paty, D.W., *Spin-spin relaxation in experimental allergic encephalomyelitis. Analysis of CPMG data using a non-linear least squares method and linear inverse theory,* Magn. Res. Med., 29, 6, 767-775 (1993).

[41] Topping, J., *Errors of observation and their treatmetn,* Chapman and Hall Ltd., UK (1955).

[42] Torrey, H.C., *Bloch equations with diffusion terms,* Phys. Rev., 104, 3, 563-565 (1956).

[43] Troyer, W.E., Holly R., Peemoeller, H., Pintar, M.M., *Proton spin-spin relaxation study of hydration of a model nanopore,* Solid State Nuclear Magnetic Resonance, 28, 238-243 (2005).

[44] Vold, R.L. Vold, R.R., and Simon, H.E., *Errors in measurements of transverse relaxation rates,* J. Magn. Res., 11,283-298 (1973).

[45] Wallace, William E., JR., *Theory and optimization of the pulsed NMR driven equilibrium technique,* J. Chem. Phys., 54, 1425-1427 (1971).

[46] Weglarz, W. P.; Haranczyk, H., Two-dimensional analysis of the nuclear relaxation function in the time domain: the program CracSpin, J. Phys. D: Appl. Phys., 33, 1909-1920 (2000).

[47] Williams, M.A.K., Keenan, R.D. and Halstead, T.K., *A nonlinear regression method for the analysis of* $^1H$ $T_2$ *dispersion curves including comments on the role of polydispersity,* Magn. Res. Chem., 36, 163-173 (1998).

[48] Whittal, K.P. and MacKay, A.L., *Quantitative interpretation of NMR relaxation data,* J. Magn. Res., 84, 134-152 (1989).

[49] Whittall, K.P., Recovering Compartment Sizes from NMR Relaxation Data, J. Mag. Res., 94, 486-492 (1991).

[50] Yeramian, E. and Claverie, P., *Analysis of multiexponential functions without a hypothesis as to the number of components,* Nature, 326, 12, 169-174 (1987).

[51] Zimmerman, K.R. and Brittin, W.E., *Nuclear magnetic resonance studies in multiple phase systems: lifetime of a water molecule in an adsorbing phase on silica gel,* J. Phys. Chem., 61, 1328-1333 (1957).

[52] http://www.originlab.com/.